Bulge–to–disk decomposition of large galaxies in the Sloan Digital Sky Survey

Dissertation
der Fakultät für Physik
der
Ludwig-Maximilians-Universität München

angefertigt von
Lidia A.M. Tasca
aus Sanremo

München, den 10th September 2004

To all those who make it possible for a dream...
to become reality.

Abstract

Understanding the way in which galaxies form and evolve remains an outstanding issue in modern astrophysics. A strong effort is being made in order to identify the physical processes involved, their relative role and the associated time–scales.

In this thesis we study the structural properties of galaxies in the local universe. Our study will serve as an ideal local zero point against which to discern evolutionary trends out to high redshift and can be also used to test competing scenarios of galaxy formation and evolution.

This analysis is performed using a magnitude limited sample of galaxies taken from the Sloan Digital Sky Survey in 5 different photometric bands, from the near–UV to the near–IR.

On all the galaxies in our sample an "eye ball" classification has been performed and for many of these galaxies we have spectroscopic information. We measure the structural parameters which characterize the two photometric components of galaxies, the bulge and the disk. We model the surface–brightness profile of galaxies using a two–dimensional photometric decomposition algorithm, which is able to automatically decompose all the objects in an input image as the sum of a de Vaucouleurs or Sérsic profile for the bulge and an exponential profile for the disk.

We use the results of the bulge–to–disk decomposition to

- quantify the amount of light in the local universe which is coming from the bulges and disks of galaxies;

- define a multi–parameter space in which galaxies of all morphological types are located according to well defined physical properties;

- identify possible relations between bulge and disk structural parameters.

The thesis is organised as follows: in chapter 1 we outline the basics of modern cosmology, with a particular emphasis on galaxy classification schemes. We describe the characteristic features of different morphological types, and review the main surveys of recent years. In chapter 2 we give an overview of the main technical aspects of the Sloan Digital Sky Survey and a

brief summary of the main results achieved. Then, in chapter 3 we describe the algorithm used to perform a detailed bulge–to–disk decomposition and we present our results on the amount of light which resides in the galactic bulge and disk components in the local universe. In chapter 4 we investigate the relations between quantitative morphological classifiers with the aim to select those ones which are suitable for quantitative, automatic and objective galaxy classification. In chapter 5 we briefly describe the correlations of the fundamental structural parameters of galaxies. We present our preliminary results on possible correlations between disk and bulge structural parameters and we discuss them in the context of different galaxy formation scenarios. Finally we draw our conclusions and discuss future developments.

Contents

List of Figures

List of Tables

"Io non so... a me la vita sembrava giá cosí difficile...
sembrava giá un'impresa viverla e basta.
Ma tu... tu sembra che devi vincerla, la vita,
come se fosse una sfida...
sembra che devi stravincerla... una cosa del genere.
Una roba strana.
È un pó come fare tante bocce di cristallo...
prima o poi te ne scoppia qualcuna...
e a te chissá quante te ne sono giá scoppiate,
e quante te ne scoppieranno... Peró...
Peró quando la gente ti dirá che hai sbagliato...
e avrai errori da pertutto dietro la schiena, fottitene.
Ricordatene. Devi fottertene.
Tutte le bocce di cristallo che avrai rotto erano solo vita...
non sono quelli gli errori... quella è vita...
e la vita vera magari è proprio quella che si spacca,
quella vita su cento che alla fine si spacca...
io questo l'ho capito, che il mondo è pieno di gente
che gira con in tasca le sue piccole biglie di vetro...
le sue piccole tristi biglie infrangibili...
e allora tu non smetterla mai di soffiare
nelle tue sfere di cristallo...
sono belle, ci si vede dentro tanta di quella roba...
è una cosa che ti mette l'allegria addosso...
non smetterla mai...
e se un giorno scoppieranno anche quella sará vita,
a modo suo... meravigliosa vita"

Castelli di rabbia Alessandro Baricco

Chapter 1

A "picture" of our Universe

In this chapter we introduce the main theoretical and observational framework in light of which the results presented in this thesis have to be interpreted. After a brief review of the properties of our Universe and of the most reliable models of structure formation, we concentrate on the galaxy classification schemes, describing the characteristic features of different galaxy morphological types, and on the main surveys of recent years.

1.1 The large-scale structure of the Universe

How is the Universe organized on large scales? How did these structures evolve from the unknown initial conditions to the present time? The answers to these questions will shed light on the cosmology we live in, the amount, composition and distribution of the matter in the universe, the initial spectrum of density fluctuations, and the formation and evolution of galaxies, cluster of galaxies, and larger scale structures.

1.1.1 The Big Bang theory

There was a time when scientists thought the universe had always existed. New evidence has convinced almost all cosmologists that the Universe somehow had a beginning.

Our present understanding of the evolution of the universe is based on the Standard Hot Big Bang Model (see Figure 1.1). It postulates that 12 to 14 billion years ago the portion of the universe we can see today was only a few millimeters across. It has since then expanded from this hot dense state into the vast and much cooler cosmos we currently inhabit. The expansion of the universe, the synthesis of light elements and the Cosmic Microwave Background radiation (CMB) are the pillars of this model.

In 1929 Edwin Hubble announced the discovery that galaxies are moving away from us with a recessional velocity proportional to their distance. The
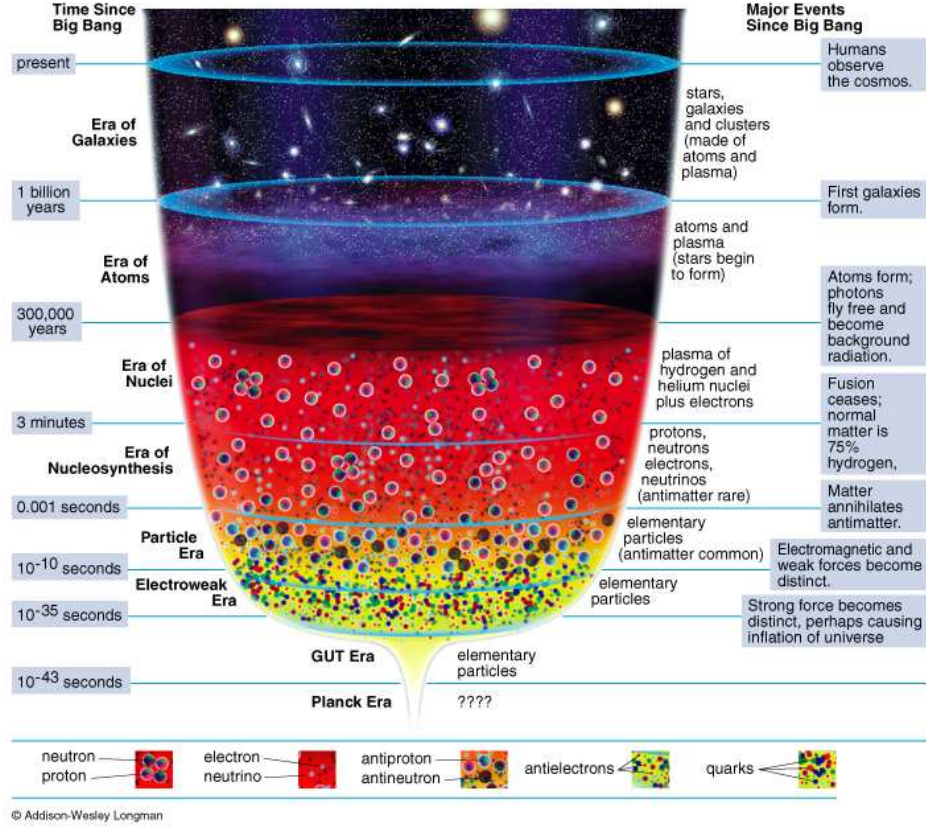
Figure 1.1: The diagram outlines the major Eras of the Universe according to the Big Bang Theory.

Hubble–law

$$v = H\,d \tag{1.1}$$

has since then been verified to hold to great distances. The uncertainty on the constant of proportionality H, often expressed in units of $100\,h$ km s^{-1} Mpc^{-1}, is condensed in the factor h. The HST Key Project (Freedman et al. 2001) has measured it with high accuracy, finding $H_0 = 72 \pm 3$ (stat.) $\pm$ 7 (syst.) km s^{-1} Mpc^{-1}. This result is confirmed by Spergel et al. (2003), who found $H_0 = 72 \pm 5$. In a ΛCDM cosmology the Hubble constant H is a function of redshift (Lahav et al. 1991):

$$\left(\frac{H(z)}{H_0}\right)^2 = \Omega_0\,(1+z)^3 - (\Omega_0 - \Omega_\Lambda - 1)\,(1+z)^2 + \Omega_\Lambda \tag{1.2}$$

where $\Omega_0 = \rho/\rho_c = 1 - \Omega_M - \Omega_\Lambda$ is the adimensional total density parameter. Ω_M and Ω_Λ are respectively the matter and the energy density and

$\rho_c = 3H^2/8\pi G$ is the critical density, needed to close the universe. Hubble's finding immediately suggested that space itself is expanding and that the universe was a lot smaller and denser in the past. Based on this observation, George Gamow realized (Gamow 1948a,b) that the universe was dense and hot enough in its early phase to allow fast thermonuclear reactions and the synthesis of light elements. When the temperature, from its initial $\gtrsim 10^{12}$ K value, had cooled down to $\simeq 10^9$ K (at a time of $\simeq 300$ sec after the Big Bang), the elements up to ^{7}Li started to be synthesized. Their abundances can be used to obtain important constraints on cosmological parameters. The universe continues to expand and cool and protons, electrons and neutrons condense into atoms. Matter and photons, initially in thermal equilibrium, decoupled at a redshift $z \simeq 1000$, when the age of the universe was only $\simeq 300,000$ yrs. A relic of this primordial black–body radiation should be seen as a now very cold $\simeq 3$ K cosmic microwave background radiation which still pervades the universe and is visible to microwave detectors as a uniform glow across the entire sky. Its first, accidental, detection dates back to 1965 by Penzias & Wilson, who received the Nobel Price for this discovery. This was the definite observational confirmation of the Gamow prediction and of the Big Bang cosmologies.

Since Hubble's discovery our knowledge of the universe has made a lot of progress and a lot of interesting features have been added to the Hot Big Bang Theory. However, the basic picture of its origin and evolution still relies on the same simple independent pieces of evidence: the expansion of the distribution of galaxies discovered by Hubble; the black–body spectrum and the isotropy of the CMB; the primordial abundance of elements.

1.1.2 Cosmological parameter estimation from CMB experiments

To take into account the enormous diversity of structures we observe in the universe it is necessary to develop a more realistic model which include tiny density perturbations. These perturbations originated as a quantum zero–point fluctuations during the period of inflationary expansion of the universe and they grew under the influence of gravity. Density fluctuations can be observed as small temperature anisotropies in the cosmic microwave background radiation (see Figure 1.2). The study of the cosmic microwave background temperature anisotropies is one of the most powerful tools to answer the basic questions about the nature of the universe: what is its geometry, its matter and energy content, what are the initial conditions which seeded the formation of structures. It is a firm theoretical conclusion that the angular power spectrum of the CMB anisotropies must encode a vast amount of information on the cosmological parameters. The majority of this information is thought to be concentrated at angular scales smaller than about 1 degree on the sky, corresponding to regions of the universe
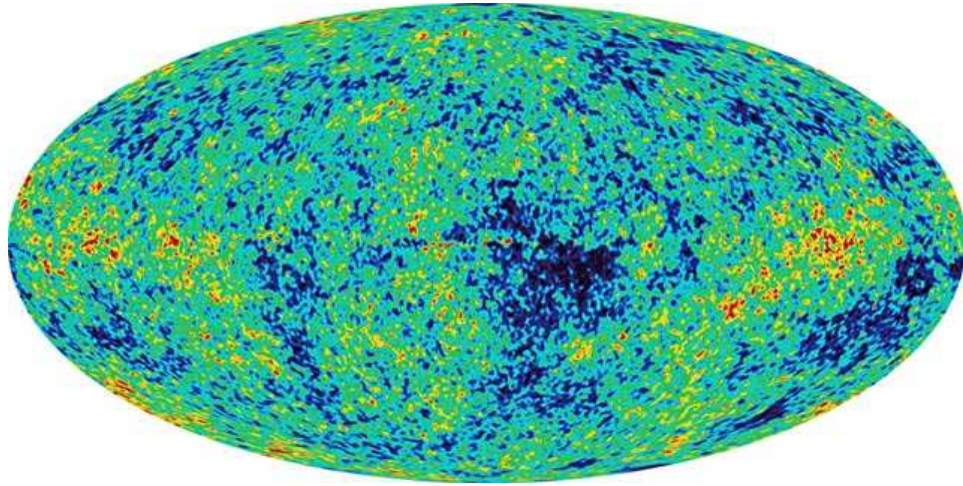
Figure 1.2: The Microwave Sky image from the WMAP Mission. Colors indicate "warmer" (red) and "cooler" (blue) spots.

that were in causal contact when the background photons decoupled from the matter, at redshift of about 1000. On these scales, physical processes in the early universe were able to leave an imprint on the CMB.

A dipole anisotropy (Conklin 1969), due to the Doppler shift caused by the solar system motion relative to the black–body field on an angular scale $\theta \simeq 180°$, was measured in the background temperature. In the 1990s the COBE (*COsmic Background Explorer*) satellite improved on the previous observations and measured an almost isotropic black–body radiation with temperature $T_{CMB} = 2.726 \pm 0.010$ K (Mather et al. 1994). It also discovered temperature anisotropies on smaller angular scales, $\theta \sim 90°$ (Smoot 1992). Following the success of COBE, new missions have been devoted to study the CMB, and the combined observations of BOOMERanG (*Balloon Observations Of Millimetric Extragalactic Radiation and Geomagnetics*) (de Bernardis et al. 2000), MAXIMA (*Millimeter Anisotropy eXperiment Imaging Array*) (Hanany et al. 2000) and WMAP (*Wilkinson Microwave Anisotropy Probe*) (Bennett et al. 2003a) have provided the power spectrum of temperature anisotropies. Anisotropies on small angular scales ($\theta < 90°$) are interpreted as the result of perturbations in the energy density at the decoupling epoch. Their detection is therefore a proof of the existence of primordial density fluctuations which grew through gravitational instabilities to form the cosmic structures we observe today. The power spectrum, $P(k, z)$, which characterise these density perturbations gives the variance of the fluctuation as a function of wavenumber k and redshift. It depends on three factors: the seed fluctuation created in the early universe, the galaxy formation process and the matter budget. An important assumption, based on simple models of inflation, is that the distribution of primordial fluctu-

ations is gaussian. WMAP demonstrated that the CMB anisotropy obeys Gaussian statistics within the 95% confidence level (Komatsu et al. (2003), Bennett et al. (2003b), Spergel et al. (2003)), confirming previous results from other CMB experiments.

1.2   Structure formation in a ΛCDM scenario

In this section we review our knowledge of galaxy formation and evolution from a theoretical and observational point of view. We focus our attention not only on what we learn from N–body simulations and semi–analytical models but we also concentrate on the scenario which is offered by deep high–redshift surveys and large–scale low–redshift ones.

1.2.1   Theory

Explaining the formation of luminous elliptical and spiral galaxies is one of the most challenging problems in modern cosmology. Galaxies form from the condensation of matter which in the past was much more uniformly distributed in the universe. From the theoretical point of view, extensive sets of numerical simulations of the early universe are performed and have improved our original simple picture of galaxy formation from large rotating and collapsing gas clouds, or "protogalaxies". Using numerical simulations we can follow the development of structures from primordial perturbations to the point where they can be compared with observations. Theoretical models of structure formation have provided interesting results for many decades but they require observational data at low and high redshift in order to put constraints on different ideas.

The favored model for the origin of the perturbations is an inflationary model, in which the universe expands exponentially for a brief period of time at early epochs ($t \simeq 10^{-35} - 10^{-33}$ s). One of the main predictions of the inflationary model is that Ω_0 is extremely close to unity. Since observational constraints on the baryon density give $\Omega_b h^2 = 0.0224 \pm 0.0009$ (Spergel et al. 2003), the presence of either a cosmological constant, Ω_Λ, or a "dark" component of matter must be invoked. Different scenarios for the evolution of the universe can be obtained (see Figure 1.3) changing the relative contribution to $\Omega_0 = 1.02 \pm 0.02$ (Spergel et al. 2003). In a widely used cosmological scenario the dark matter is composed of cold, weakly interacting massive particles; thus, they are usually referred to as Cold Dark Matter (CDM) cosmologies. Weakly interacting means that they must have a negligible interaction cross–section and cold means that they must have been slowly moving at the onset of the matter dominated epoch, in order to be able to immediately cluster gravitationally. Dark matter particles are finally required to be massive. This means that they are gravitationally self–attractive, like ordinary matter, and cluster with it to form structures like

EXPANSION OF THE UNIVERSE
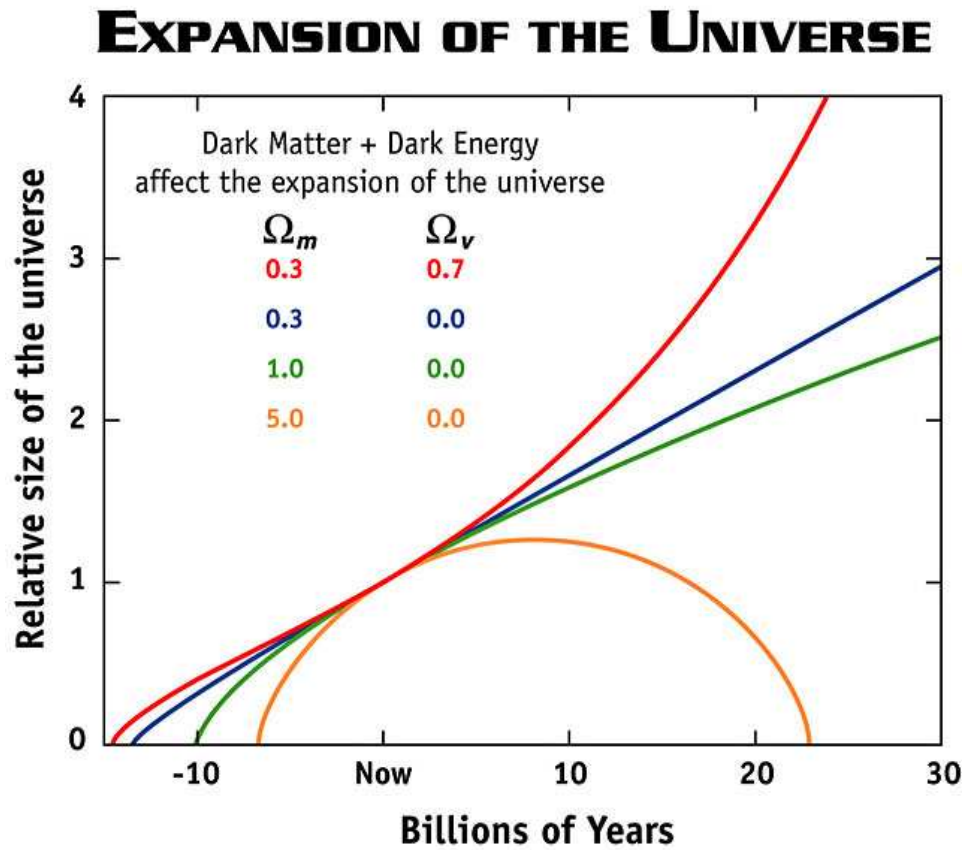
Figure 1.3: Scenarios for the relative size of the universe vs. time: the bottom (green) curve represents a flat, critical density universe in which the expansion rate is continually slowing down. The middle (blue) curve shows an open, low density universe whose expansion is also slowing down, but not as much as the critical density universe because the pull of gravity is not as strong. The top (red) curve shows a universe in which a large fraction of the matter is in a form dubbed "dark energy" which is causing the expansion of the universe to speed up (accelerate). There is growing evidence that our universe is following the red curve.
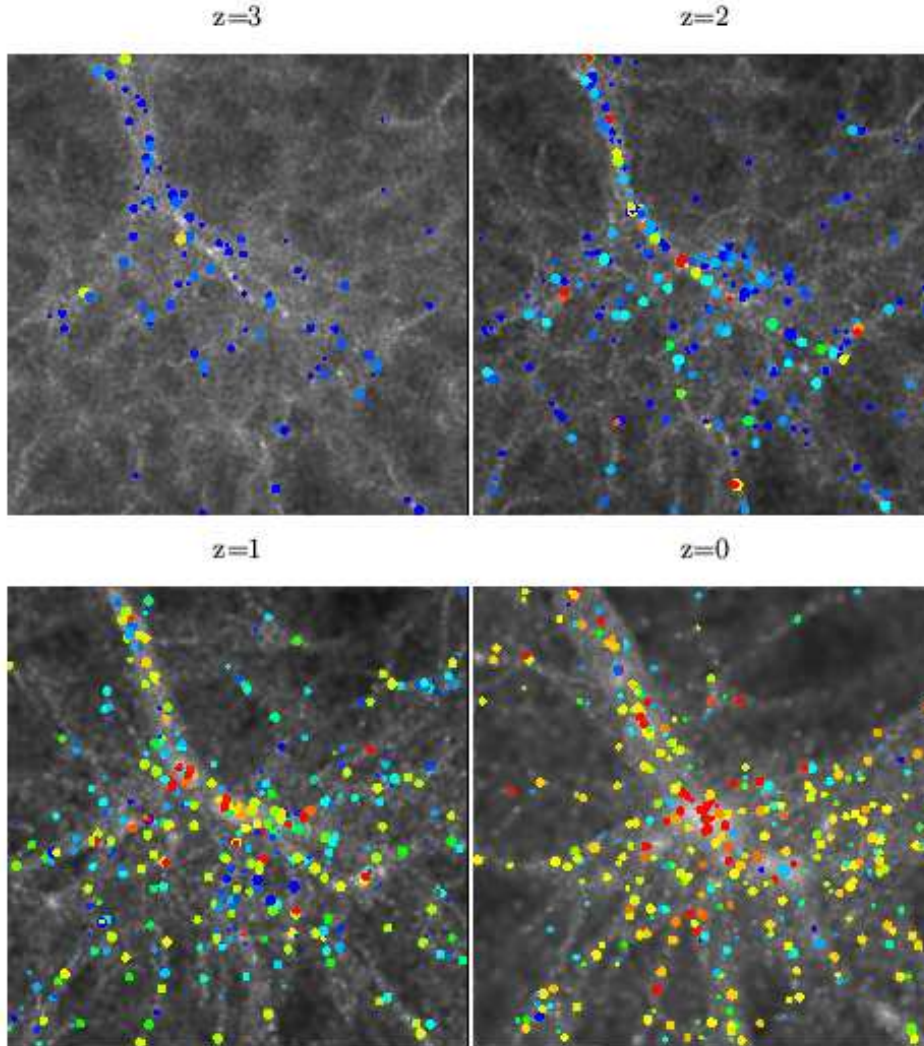
Figure 1.4: Population of galaxies superposed on dark-matter distribution (grey-colored) in a small region of 21x21x8 (Mpc/h)^3. Galaxies are shown as circles colour-coded according to their star formation rate: the sequence red, yellow, green and blue represents an increasing rate of star formation. At early times (top left panel) there exist only a few galaxies forming stars at a very high rate. As time goes on, from z=3 to z=0, more galaxies form and, at the same time, some galaxies run out of gas, form fewer stars and become green, yellow and red. At the present time (z=0), red galaxies populate the central region of the cluster, whereas blue galaxies can be found in the outskirts of the system. This is very similar to what is observed in the real Universe. Credit: Joerg Colberg and Antonaldo Diaferio

galaxies and clusters. When the universe becomes matter dominated, perturbations grow completely decoupled from the matter and radiation. Only after the epoch of recombination the baryons collapse into the potential wells of dark matter halos to form galaxies and structures. The Press and Schecter formalism (Press & Schechter 1974) well describes how the mass function of objects of various masses evolves with time.

Two competing scenarios for the formation of elliptical galaxies have been proposed so far: **monolithic collapse** (Eggen, Lynden-Bell, & Sandage (1962), Larson (1974), Tinsley & Gunn (1976)) and **hierarchical merging** (Kauffmann & White (1993), Cole et al. (1994)). In the first scenario all the galaxies and the stars therein are formed in a single burst and subsequently evolve passively with no further star formation. More precisely at z $\gtrsim 2$ gravitational collapse of gas clouds with considerable energy dissipation leads to the formation of stars within a very short period of ~ 100 Myrs with star formation rate of 10^2 - 10^3 $M_\odot yr^{-1}$, creating massive galaxies that thereafter passively evolve in luminosity. The commonly adopted theory for structure formation is the gravitational instability scenario, in which primordial density perturbations grow through Jeans instability to form all the structures we observe today. The Cold Dark Matter scenario predicts that the most massive galaxies we observe in the local universe formed through multiple major mergers of pre–existing smaller systems. These processes are found to occur in simulations of galaxy formation. An alternative scenario is proposed by Cole et al. (1994) and Kobayashi (2002) with the difference that in the latter the formation and evolution of stellar system is decoupled from the evolution of dark halos. In their scenario galaxies form through the successive merging of sub–galaxies of various masses: if galaxies form by the assembly of gas–rich small galaxies, it looks as a monolithic collapse; otherwise the evolved galaxies with small gas fraction merge and form elliptical galaxies.

Although it seems well understood that the dark matter halos are built in a hierarchical process controlled by the nature of the dark matter, the power spectrum of density fluctuation, and the parameters of the cosmological model, the physics which governs the assembly of the stellar masses in galaxies is yet not fully included in semi–analytical codes. There are different types of mass assembly that are related in an unknown way, including the collapse, infall, and accretion of dark and baryonic matter, which are likely to be related to how baryonic material is converted into stars. Assembly of galaxies and dark halos through mergers and accretion is the cornerstone of all cold dark matter models of galaxy formation (Cole et al. 2000). In numerical simulations, the dark matter is generally represented as a collisionless, dissipationless fluid, while the gas is often described by smoothed particle hydrodynamics (SPH). When simulating the large–scale structure of the universe, the dark matter alone traces all the relevant scales, while the treatment of baryonic processes becomes indispensable only when simulating

the detailed structure of galaxies and sub–galactic objects (see Figure 1.4). Although CDM models predict that dark matter halos merge, it is not clear whether galaxy formation or star formation occurs before, during or after dark–halo mergers. If baryons collapse to form stars in dark halos before a large amount of halo merging, then, based on dynamical friction arguments, we should witness mergers of galaxy stellar components. On the other hand, it also possible that gas cools and forms into stars after dark halos merge, producing the large galaxies we observe today (Noguchi 2000).

The CDM model with the "concordance" set of cosmological parameters (ΛCDM) provides a remarkably successful framework to explain a broad range of observations of structures on scales larger than $\simeq 1$ Mpc, although some problems still need resolving. The non–linear growth of structures is investigated through numerical simulation of gravitational clustering. N–body techniques have achieved the dynamic range necessary to resolve substructures within virialised structures and a new generation of very high–resolution simulations has demonstrated that the presence of substructures is unavoidable in every cosmological scenario invoking the cold dark matter paradigm. Nevertheless in dissipationless simulations substructures disrupt very quickly in dense environments (*"overmerging problem"*, Katz & White (1993)). Observationally, the predicted abundances of substructures in clusters is one of the major successes of the CDM model (Springel, et al. 2001), but on galactic scales, it appears that simulations over–predict the number of substructures by almost two orders of magnitude (Kauffmann, White & Guiderdoni 1993). Solutions have been proposed which involve either changes in the cosmological paradigm or in the physics of the baryons. In the first case the nature of dark matter may be different to that assumed in the standard ΛCDM models, for example, by being warm or self–interacting, both of them could eliminate small–scale structure. The second solution states that the presence of a strong photoionising background radiation, after reionisation, suppresses the accretion and cooling of gas in low mass halos (Efstathiou (1992), Navarro & Steinmetz (1997)). If the gas is unable to cool, stars do not form and small halos cannot be detected because of a lack of stellar light. The other problem is that cold dark matter models predict halos that have a inner density profile which is too steep compared to the observed ones (*"cuspy halo problem"*, Moore et al. (1998))

1.2.2 Observations

To understand the assembly of large–scale structure in the universe and to trace the history and evolution of galaxies are the main goals of observational cosmology.

The fundamental question is how the universe developed from the initial, nearly homogeneous state to the complex form we observe today. While

on large scales ($\gg$ 100 Mpc) the universe is indeed very smooth, inhomogeneities are in evidence on small scales, from planets and stars to galaxies, which are themselves clustered in associations ranging from small groups ($M \geqslant 10^{13}$ M$_\odot$) to rich clusters ($M \geqslant 10^{15}$ M$_\odot$). These structures are not uniformly distributed, but rather have some spatial correlation, and regions of space almost totally void of galaxies are juxtaposed to high density regions. Rich clusters of galaxies, the largest gravitationally bound systems in the universe, are grouped together to form super–clusters, filaments, walls and other structures on larger scales which still have not had the time to relax to a state of dynamical equilibrium.

The main processes in galaxy formation are the assembly of mass, both baryonic and dark, through accretion and mergers, and the conversion of baryons into stars. Various methods are applied to statistically map the latter out to nearly the beginning of the universe (Lilly et al. (1996), Madau, Pozzetti, & Dickinson (1998)) while a lot of steps are still needed before we can understand how and when masses were assembled. A redshift domain where galaxies are expected to be strongly affected by merging or assembly processes is at z $\gtrsim$ 1, so that here are focused the main studies of the evolution of physical properties of galaxies.

Obtaining statistically significant samples of galaxies, from the local universe to the highest redshifts, is mandatory to constrain models of galaxy formation and evolution. Large spectroscopic samples of galaxies at all redshifts have become available during the last ten years, thanks to massive surveys in different rest–frame wavelength domains (Lilly et al. (1995); Steidel et al. (1996), Steidel et al. (1999), Steidel et al. (2004), Colless et al. (2001), Schneider et al. (2003)).

The observational study of galaxy formation and evolution can be performed using different methods: tracing how stellar masses are assembled in galaxies, measuring the galaxy clustering at different redshift and following the merging history over cosmic time are only few of them. They are related to each other since the building up of stellar masses in galaxies is the consequence of their past star formation and merging history.

Galaxy number counts

Since the availability of deep optical galaxy number counts, the excess at faint magnitudes has provided the major evidence for galaxy evolution at increasing redshifts (Tyson (1988), Lilly et al. (1991), Metcalfe et al. (1995)). Using models of spectro–photometric evolution of galaxies (Bruzual A. & Charlot 1993), either passive luminosity evolution or more complex effects have been suggested to explain the faint number–count excess. Initially the excess objects were envisioned as early–type galaxies at high–z but the lack of a corresponding high–z tail in the redshift distribution (Lilly 1993), consolidated the interpretation in terms of evolution of later type galaxies such

as spiral, irregular or peculiar galaxies. It is obvious that a reliable description of galaxy evolution requires proper identification of the evolving galaxy population and detailed knowledge of their luminosity functions. de Lapparent et al. (2004) obtain evidence for evolution of late spirals and maybe dwarf irregulars at $0.1 < z < 0.5$.

In all analyses of redshift and magnitude distributions, the major difficulty is to distinguish between luminosity and density evolution, as these produce the same net effect on the distributions. Interpretation of density and luminosity evolution of a galaxy population is also complicated by possible variations in the star formation rate with cosmic time: Lilly et al. (1998) evaluate an increase in the star formation rate of galaxies with large disks by a factor of ~ 3 at $z \sim 0.7$, which shows an increase of the luminosity density at bluer wavelengths.

Major galaxy mergers

Galaxy merging is of fundamental importance for understanding the formation and evolution of galaxies. The outcome of a merger between two galaxies depends on the mass ratio between the two objects, their intrinsic and orbital angular momenta and their gas content. Mergers between objects with a mass ratio lower than 1:4 will not fundamentally change the structure of the more massive galaxy. A method of determining whether and how galaxies form by merging is to measure directly the fraction of galaxies undergoing mergers and mass assembly occurring by mergers at various look–back times, and estimate from these merger and mass assembly rates. The mass assembly history for nearby galaxies is mostly lost through equilibrium and relaxation processes. The most popular method for measuring the evolution of galaxy mergers at high–z is through pair counts or kinematic pairs (Carlberg et al. 2000). After correcting for selection effects and biases (Patton et al. 2000), pair–count methods can be used to study major galaxy mergers out to $z \sim 1$. Conselice (2003) propose to use the stellar light distribution, and in particular the observed structure of galaxies, in order to identify high–z galaxies which are undergoing mergers. Using the concentration, asymmetry, clumpiness (CAS) physical morphological system, Conselice et al. (2003) find, in agreement with Le Fèvre et al. (2000) that out to $z \sim 1$ the fraction of galaxies involved in major merger increases and in addition they claim that the merger fraction continues to increase with redshift for the brightest and most massive systems. Density evolution indicates that mergers could play a significant role in the evolution of late–type spirals and irregulars. Le Fèvre et al. (2000) find, using both visually identified mergers and pair counts, that the observed merger rates evolves with redshift as $(1 + z)^m$ with m ranging from 3.2 to 3.4, from $z \sim 0$ to $z \sim 1$. Interestingly de Lapparent et al. (2004) find that a significant fraction of the merger galaxies have a spiral or irregular structure. The fraction

of galaxy stellar mass density involved in mergers also increases as a function of redshift, but much more rapidly and with a higher maximum fraction for the brightest and most massive systems. More in detail, for galaxies with $M_B < -21$ or $M^* > 10^{10}$ M$_\odot$ the fraction of mass involved in mergers is ~ 0.5 at $z \sim 2.5$, demonstrating that at least half of mass in the most massive galaxies in the nearby universe was involved in major mergers ~ 9 Gyrs ago.

Galaxy clustering

Measurements of clustering at large redshifts can be used to shed light on the assembly of large–scale structure in the universe and to trace the evolution of galaxies. Redshift surveys have been able to study galaxy clustering up to $z \sim 1$ finding a general decrease in clustering strength with redshift (Le Fèvre et al. 1996). In the local universe it is well established that galaxies of different types cluster very differently (Guzzo et al. 1997). At $z \sim 1$ some evidence of a significantly different clustering of early and late–type galaxies is also found. A population of strongly clustered $z \sim 3$ galaxies have been discovered by Daddi et al. (2003). The study of the number density and clustering of this population brings the conclusion that a direct evolutionary trend exists between these $J - K$ red $z \sim 3$ galaxies on one side and Extremely Red Objects (EROs) at $z \sim 1.5$ and local massive early–galaxies on the other side.

Formation of massive galaxies

Massive galaxies in the local universe include elliptical and spiral galaxies with large central bulges. There are well defined predictions for how massive galaxies should form. They are relatively easy to study as they are usually very bright at any epoch since they contain most of the stars. Nevertheless, the essential questions on when and how massive galaxies formed are still without an answer and have started to be investigated only recently. A solution may come from the study of the properties of massive galaxies at high redshift when they were formed. The first ultraviolet selected sample of these galaxies at $z \sim 3$ shows similar number densities and clustering properties to nearby massive galaxies (Steidel et al. (1996), Giavalisco (1998)), but lower stellar mass density (Dickinson et al. 2003). In agreement with the Cold Dark Matter model, these observations are proof that some massive galaxies do not form all their mass early. In addition, the discovery (Steidel et al. 1996) of a population of star forming galaxies at $3 \leqslant z \leqslant 3.5$ using a color technique whose efficiency is very high, allows to study their space density, star formation rates, morphologies and physical sizes. These results demonstrate that massive galaxy formation was well underway by $z \sim 3.5$. Summarising, the available data show that cluster ellipticals must
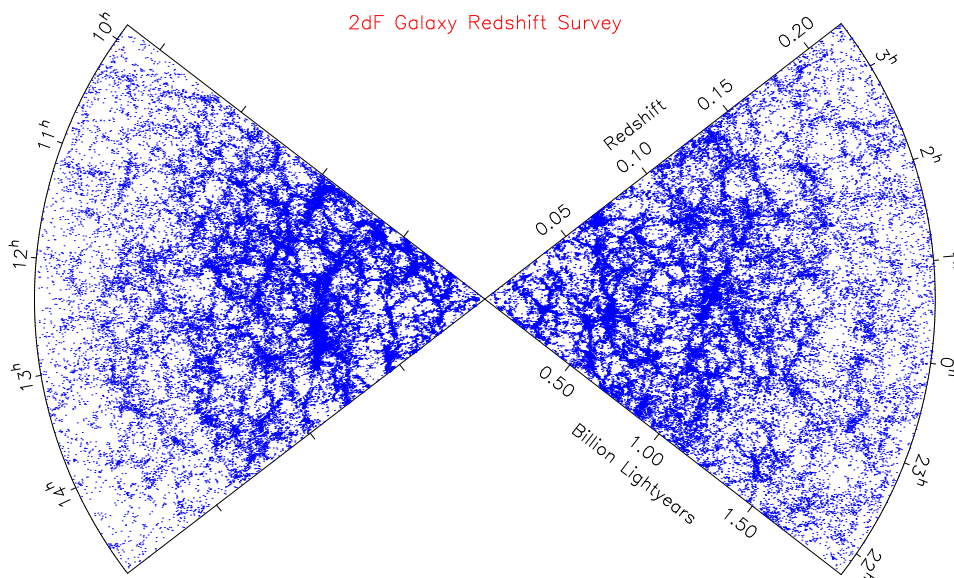
Figure 1.5: Distribution of galaxies in the 2dFGRS.

have rapidly formed at $z > 2$, and that up to 50% of all massive galaxies at $z \simeq 2.5$ are involved in major mergers. In support of the bottom–up scheme of galaxy formation is the discovery (Pascarelle et al. 1996) of a large number of faint, compact objects at $z \approx 2.4$, which appear to be star–forming spheroids smaller than the bulge of spiral galaxies. It is suggested that these sub–galactic sized objects exist throughout the entire redshift range $1 < z < 3.5$, and could have grown into the luminous giant galaxies that we see today through the process of repeated hierarchical merging.

1.3   Galaxy redshift surveys

Limits on when galaxies have begun to form and when the formation process ended are provided by recent results from deep redshift surveys and from the various missions aiming to measure the temperature fluctuation in the cosmic microwave background. Galaxy redshift surveys have achieved significant progress over the last couple of decades and help us to understand what our universe looks like: the galaxy distribution traces the bright side of the universe while detailed quantitative analyses of the data have revealed the dark side of the universe, dominated by non–baryonic dark–matter and more mysterious dark energy.

In the 1980s and 1990s the first redshift surveys (CfA, (Huchra et al. 1983); *Automated Plate Machine* (APM, Maddox et al. (1990)); *Las Campanas*, (Lin et al. 1996); *Canada-France Redshift Survey* (CFRS , Lilly et al. (1995))) measured tens of thousands galaxy redshifts. Nowadays, multi–fibre

technology allows us to measure the redshift of millions of galaxies. In between them it is worth mentioning the impressive results of the *2dF Galaxy Redshift Survey* (2dFGRS, Colless et al. (2001)) and of the *Sloan Digital Sky Survey* (SDSS, York et al. (2000)) at low redshift and the VIRMOS deep imaging survey (Le Fèvre et al. 2004) and DEEP2 survey (Davis et al. 2003) at high–z. In this section we do not intend to summarise the past, recent and future surveys but rather underline how surveys at various redshift and in different wavelengths contribute to increase our knowledge on the longstanding and still unresolved problem of galaxy formation and evolution. In particular we focus our attention on the kind of observations which need to be performed in order to give an insight on the formation of the Hubble sequence (see section 1.4.2).

The 2dFGRS and SDSS are massive surveys at high galactic latitude and provide definitive measures of large–scale structure and galaxy properties in the nearby universe. The completed 2dFGRS yields a striking view of the galaxy distribution over a large cosmological volume. Figure 1.5 illustrates the projection of a subset of the galaxies in the northern and southern stripes onto (α, z) slices. In addition to these shallower surveys ($z < 0.2$), the VLT/VIRMOS and the Keck/DEIMOS redshift surveys provide samples of galaxies at $z \sim 1$, advancing our knowledge of the evolution of the properties of galaxies and of large–scale structure.

For a long time high redshift galaxies were too faint for spectroscopic observations. The Lyman–break technique (Steidel et al. 1996) finally made it feasible to detect galaxies at very high redshift. The method is based on the fact that we receive virtually no radiation from galaxies below the Lyman break so that one can search for the so called drop–out objects, which are detectable in the longer wavelength filters but have no flux in the shorter ones. As normal consequence, this technique cannot be applied on galaxies with little or no ongoing star formation for which infrared or sub–mm surveys are required. Recent advances in near–infrared (NIR) capabilities on large telescopes have made it possible to select high redshift galaxies in the rest–frame optical rather than in the rest–frame UV. The rest–frame optical is much less sensitive to dust extinction and is expected to be a better tracer of stellar mass. In this respect the FIRES project (Franx et al. 2003) is the deepest ground–based NIR survey to date. High–z galaxies are selected with a simple color criteria ($J_s - K_s > 2.3$) which efficiently isolated galaxies with prominent Balmer or 4000 Å–break at $z > 2$. This rest–frame optical break selection is complementary to the rest–frame UV Lyman break selection. The population of red objects at $z > 2$ seems to be highly clustered, and the available evidence suggests they could be the most massive galaxies at high–z and progenitors of today early–type galaxies. The Spitzer Space Telescope (formerly SIRTF, *Space Infrared Telescope Facility*) observations out to 8μm will sample rest–frame 2μm light from galaxies out to $z = 3$ and 1μm light out to $z = 7$. This should provide much better constraints on stellar

masses than NICMOS and ground–based data, which only reach optical rest–frame light at high–z. K–band surveys have long been recognized as ideal tools to study the process of mass assembly at high–z (Broadhurst et al. (1992), Gavazzi et al. (1996), Madau, Pozzetti, & Dickinson (1998)). The K–band luminosity of a galaxy samples up to high–z the rest–frame optical and near–IR spectral range and therefore it is very nearly independent of star formation and dust extinction, but reflects the mass of the old stars within the galaxy. The results show that galaxies selected in the K band are characterised by a modest luminosity evolution up to $z \simeq 1$, that seems well described by simple pure luminosity evolution models. Moving towards longer wavelengths, we find that radio–loud AGNs, invariably associated with early–type host galaxies, can inhabit regions with a very rich interstellar medium (ISM) whose presence is likely to be related to the origin and evolution of the host galaxy and of the active nucleus. Recent observations show that a large fraction of radio galaxies contain significant young stellar population. This supports the idea that mergers are responsible for both the star burst phase and the triggering of the nuclear activity. The origin and activity in galaxies is often explained as being triggered by merger or interaction processes.

Multi–wavelength observations are an essential requirement in order to bring new insight on the physical parameters involved in the evolution of galaxies. When we observe a galaxy we have to account for the fact that we are measuring morphological parameters at different rest–frame wavelengths at different redshifts. The high–z redshift population is dominated by peculiars, while at low–z ellipticals and spirals are common. These high–z peculiars, often referred to as Lyman–break galaxies (LBG), could be the progenitors of massive nearby systems. It is therefore important to determine the future evolution of the high–z galaxy population in order to piece together the history of galaxy formation. In doing that one has to observe galaxies at different redshifts but in the same rest–frame wavelength. Hubble Space Telescope (HST) observations support the hypothesis that LBG, evolving through merging, could be the progenitors of massive ellipticals. Disk galaxies likely cannot form through these mergers since the spiral structure would not survive them. It is therefore supposed that they are forming at about the same time they appear morphologically, at $z \sim 1.5$. These galaxies have now possibly been identified at $z > 1.5$ by their low light concentration in HST Advanced Camera for Survey (ACS) images (Conselice et al. 2004). These luminous diffuse objects show comoving volumes similar to nearby massive disks and are common at $1 < z < 2$.

The evolution of the physical properties of galaxies as a function of redshift is particularly important for galaxies as $z \gtrsim 1$, a redshift domain where galaxies are expected to be strongly affected by merging or assembly processes. de Lapparent et al. (2004) show the utility of using both magnitude and redshift distribution to study galaxy evolution. By obtaining the

redshift distributions per galaxy type to $z \gtrsim 1$ over large volumes which average out the large–scale structure, spectroscopic redshift surveys such as the VIRMOS and the DEEP2 projects should provide improved clues on the evolving galaxy population at $z \sim 1$ and better constrain the nature of this evolution. In this framework the HST–COSMOS project is perfectly designed to study the evolution of galaxies over cosmic time, revealing the detailed morphologies of extremely distant galaxies and their environment. For the first time an area of sky as large as 2 square degrees will be mapped with the ACS. Observations will be supplemented by extensive multi–object spectroscopy (MOS) with the VIMOS spectrograph and by multi–wavelength observations, including deep imaging optical and NIR data, deep VLA, SIRTF–Spitzer, XMM, Chandra and sub–mm data.

1.3.1 Future

While the observation of very high–redshift universe, $z \simeq 1000$, is possible through the CMB, there is a lack of observational data about the universe in the redshift interval $10 \leqslant z \leqslant 10^3$, a recent study finding a galaxy having $z = 10$ (Pelló et al. 2004). The state of the art of the telescopes observing in the NIR/optical/UV range is represented by the Advanced Camera for Surveys (ACS) and the Near Infrared Camera and Multi–object Spectrometer (NICMOS) on board the Hubble Space Telescope (HST), that allows to take unprecedented high–resolution images such as the Hubble Ultra Deep Field (see Figure 1.6). This is the Hubble's deepest view of the universe. It unveils galaxies that existed between 400 and 800 million years ($7 \lesssim z \lesssim 12$) after the Big Bang. They present a wide range of sizes, shapes and colours in a very chaotic universe. Order and structures were just beginning to emerge.

In order to observe radiation from objects at even higher redshift, telescopes with very high sensitivity in the IR band are needed. The James Webb Space Telescope (JWST) with its exceptional nJy sensitivity in the $1 - 10\mu m$ infrared regime is ideally suited for probing optical–UV emission from sources at $z \geqslant 10$. Thus, in the near future, we should be able to image the first sources of light that had formed in the universe. We will be finally able to answer questions about the first sources of light in the universe, how galaxies were assembled, how the Hubble sequence forms and many others.

1.4 The morphological classification of galaxies

It was not until the early part of the 20th century that astronomers even recognized that the nebulous objects they often saw in the sky were in fact vast collections of stars like our own galaxy. Improvements in telescope technology allowed observers to distinguish these systems of stars from other nebulous objects such as large clouds of gas and dust or globular clusters. In this section we discuss the morphological classification of galaxies, which
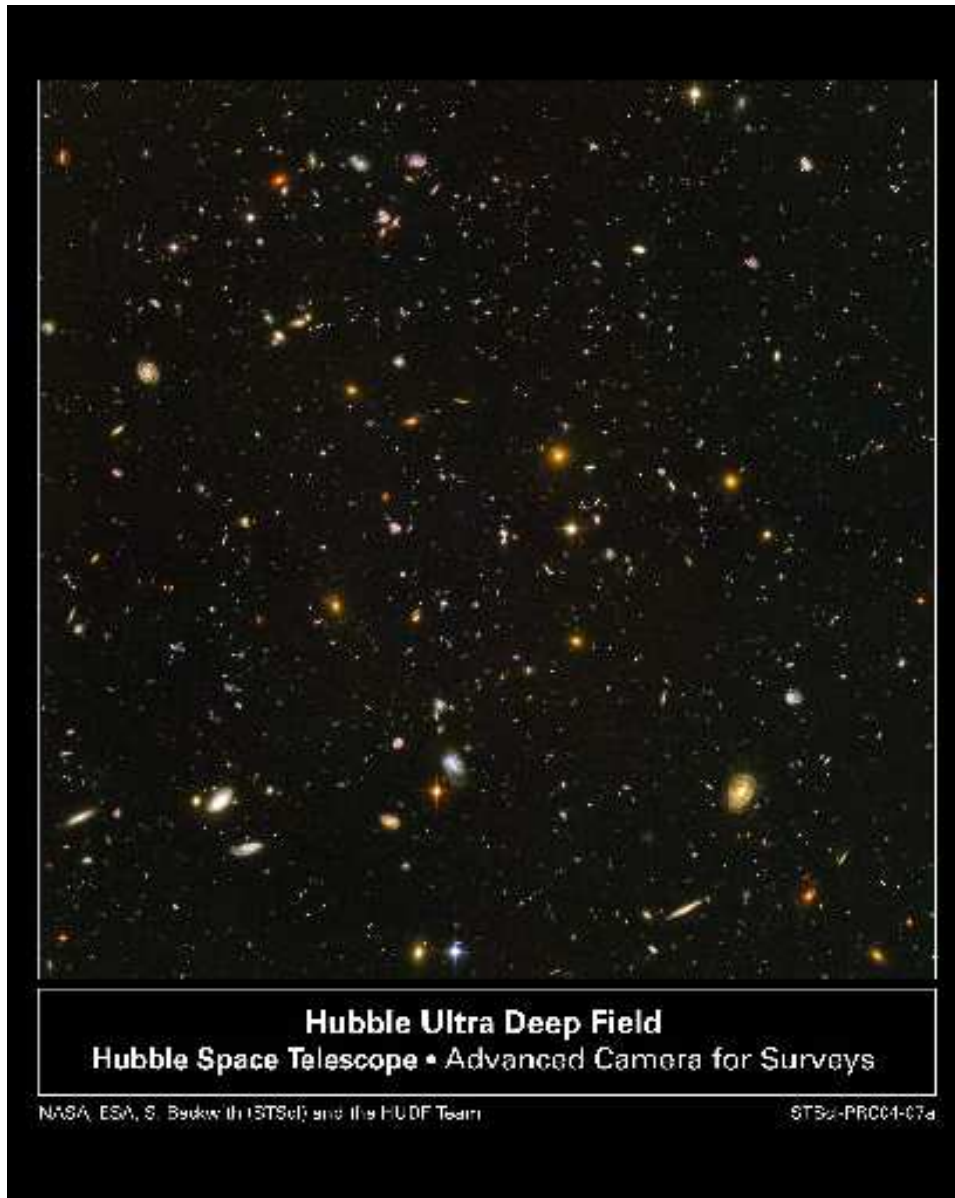
Figure 1.6: Hubble Ultra Deep Field.

is the classification of galaxies into types according to their shapes or their spectroscopic properties.

1.4.1 Basic components of galaxies

The various components of galaxies show photometric and spectroscopic differences which are a consequence of different kinematic and dynamical properties as well as different stellar populations and gas and dust content. More in detail we can distinguish:

- a **bulge** or spheroidal component, whose surface brightness profile $I(r)$ follows roughly a de Vaucouleurs law

$$I(r) = I(r_e) \, 10^{-3.33((r/r_e)^{0.25}-1)}. \tag{1.3}$$

  It generally contains an old stellar population with a range of metallicity spanning from very poor to super metal rich.

- a **disk** with a surface brightness profile following an exponential law

$$I(r) = I_0 \, \exp^{-r/h}. \tag{1.4}$$

  It has a strong rotation and it shows metal rich stars, with a wide range of ages, together with HI and H_2–gas, molecular clouds, dust and hot gas, heated by star formation and supernovae.

- a **baryonic halo** which contains metal poor stars, with little or no rotation and a wide variety of orbits, globular clusters, low density HI and HII gas and and X-ray gas, particularly prominent in ellipticals.

- a **dark halo** which dominates the mass outside of 10 kpc and whose total mass in dark matter is 5 to 10 times larger than the baryonic mass.

1.4.2 The Hubble classification scheme

When classifying galaxies according to their shapes we have to be aware of some observational constraints: images at different resolutions or in different photometric bands cannot be compared to each other. The same spiral galaxies will appear more clumpy in the UV band, which is more sensitive to the star formation, than in the NIR which well samples the old population and where dust effects less affect the shape of the galaxy. Although this may appear obvious at low redshift, it becomes essential if one wishes to compare the morphology of galaxies at high redshift with that of galaxies in the local universe: for this comparison it is necessary to have images in the same rest–frame wavelength. With this warning we can start to consider the various classification schemes, keeping in mind that we are strongly biased
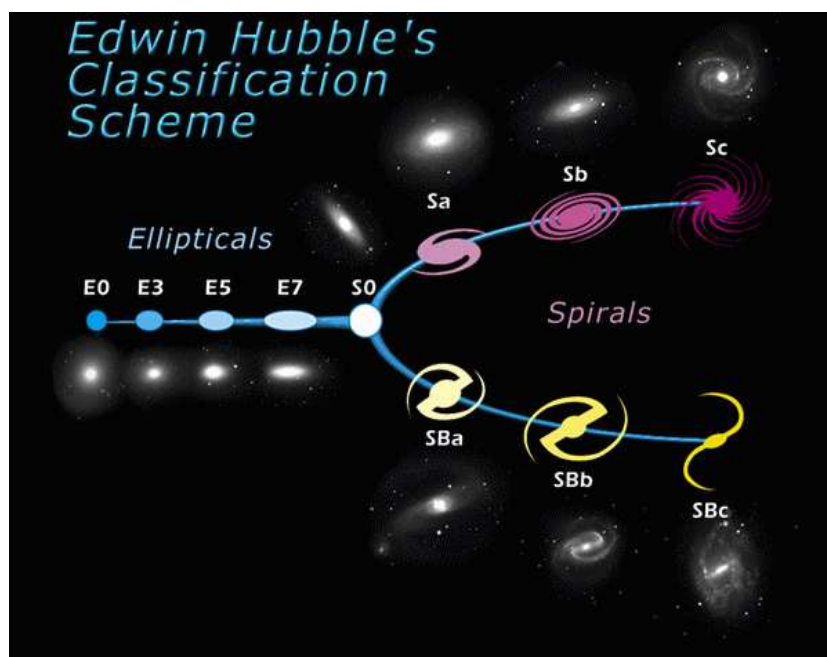
Figure 1.7: The Hubble tuning fork diagram depicting the basic galaxies shapes observed in the present Universe.

in the choice of the classification parameters by the appearance of galaxies at the visible wavelength at which our eyes are sensitive. The morphological classification of galaxies is the first step in order to create models which provide a physical explanation for the formation of the variety of objects we observe today. For this reason it has to be based on parameters which are linked to physical properties of the galaxy.

After he discovered what galaxies really were, Edwin Hubble in 1936 became the first person to classify galaxies (i.e. Figure 1.8). The **"Hubble Tuning Fork"** (see Figure 1.7) went through various modifications and found its definitive exposition in *The Hubble Atlas of Galaxies* (Sandage 1961).

Elliptical galaxies

On the left of Hubble's tuning–fork diagram are placed those galaxies which appear smooth and structureless. These **elliptical galaxies** vary in shape from round to fairly highly elongated and are designated En, with $n = 10[1 - (b/a)]$ determined by the galaxy's observed ellipticity. Elliptical galaxies, such as M87, have very little cold gas and dust. Since gas and dust are

Hubble's Classification of Galaxies
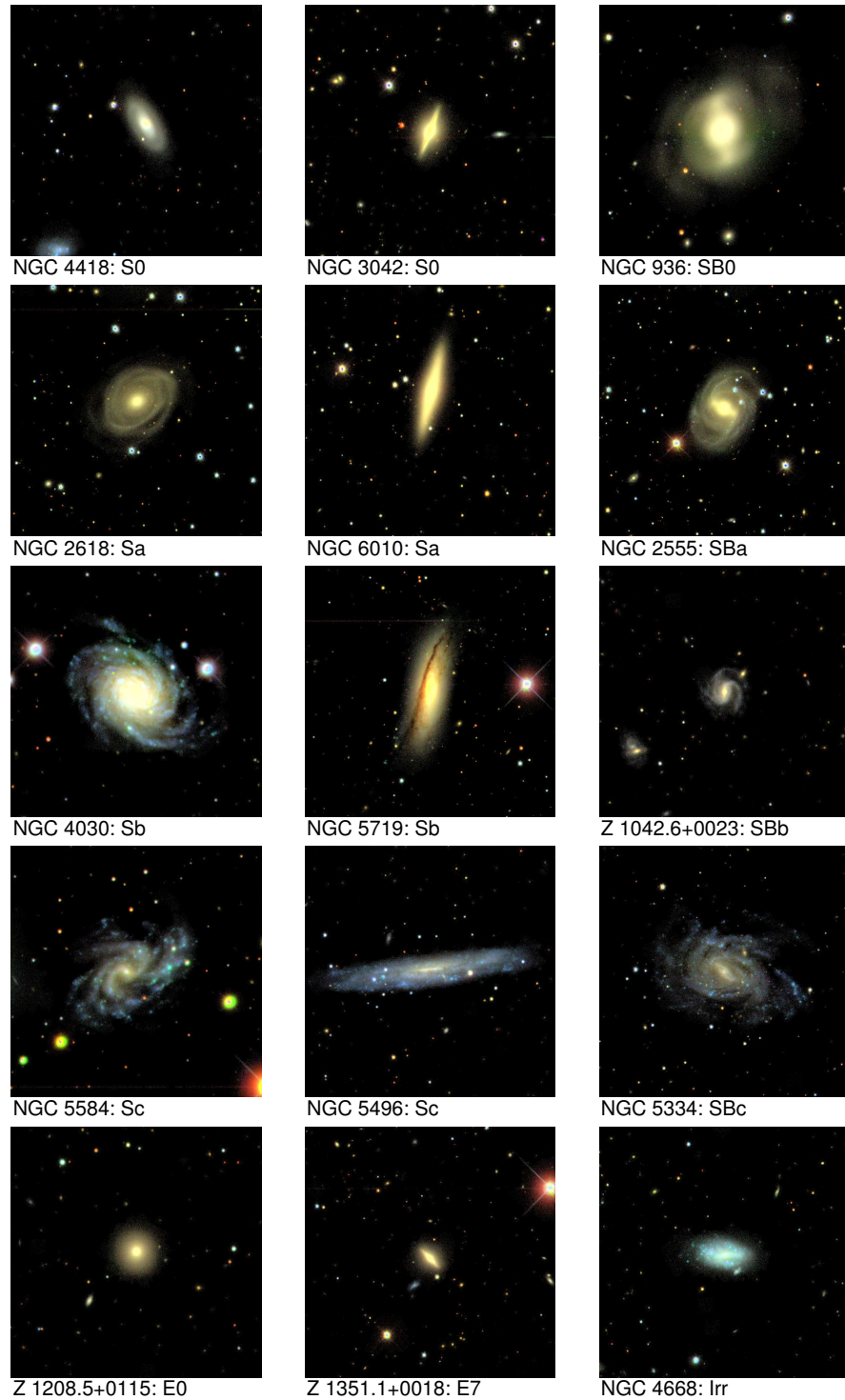
Figure 1.8: Galaxy Hubble types from SDSS. 5×5 arcmin true–color g–r–i images. Zelijko Ivezic and Robert Lupton for the SDSS Collaboration.

found in the clouds that are the birthplaces of stars, we should expect to see very few young stars in elliptical galaxies. In fact, they contain primarily old, population II, red stars. Elliptical galaxies vary widely in size so that the largest and the smallest known galaxies belong to this class.

These objects for long time were wrongly considered as simple systems. More accurate studies have actually revealed their real complexity:

- massive ellipticals are not flattened by rotation, but pressure supported;

- they have hot, $T > 10^6$ K, interstellar medium;

- kinematic peculiarities are exhibited by a significant fraction of them, as counter–rotating cores, which point to a violent formation process. The core is the most central region and extends until the surface brightness becomes half that at the centre.

- low–mass ellipticals seem to contain intermediate age stars;

- all ellipticals and bulges seem to contain super-massive black holes accounting for 0.2% of their mass.

Ellipticals are known to obey various relations. The color–magnitude relation states that more luminous elliptical galaxies have stronger absorption line and are redder. It is also demonstrated that more luminous ellipticals have larger central velocity dispersion. This correlation is called **Faber–Jackson relation** (Faber & Jackson 1976):

$$L \sim \sigma_0^4. \tag{1.5}$$

Kormendy (1977) shows that larger galaxies have fainter effective surface brightness. It was discovered by Djorgovski & Davis (1987) that ellipticals lie in the **Fundamental Plane** which is defined by the effective radius, the central velocity dispersion and the effective surface brightness.

Spiral galaxies

After ellipticals the Hubble's diagram bifurcates into two branches: **"normal"** and **"barred"** galaxies. The two types occur with similar frequencies and misclassification is quite common since the bar-like characteristics may be lost on small–scale plates, especially for nearly edge–on systems. A normal spiral galaxies comprises a central brightness condensation, which resembles an elliptical, located at the center of a thin disk containing more or less conspicuous spirals of enhanced luminosity, the spiral arms. A barred spiral has, interior to the spiral arms, a bar, often containing dark lanes believed to be produced by absorption of light by dust. The spiral arms generally

emanate from the ends of the bar. The two distinct regions of spiral galaxies correspond to different stellar populations. The disk is a region of star formation and has a great deal of gas and dust. It is dominated by young, blue, population I stars. Instead the central bulge is devoid of gas and dust and it is primarily composed of population II stars.

Spiral galaxies are further classified into S(B)a, S(B)b, S(B)c, S(B)d according to the following properties:

- the tightness with which spiral arms are wound, Sa galaxies have their arms tightly wound. More quantitatively the opening angle of spiral arms is $0° − 10°$ for Sa $5° − 20°$ for Sb and $10° − 30°$ for Sc;

- the relevance of the bulge in producing the overall light distribution of the galaxy. It decreases towards later types;

- the degree to which spiral arms are resolved into stars and HII regions;

- the increasing amount of gas, dust, young stars and HII regions.

They are actually related to each other (i.e. the total luminosity decreases as soon as the bulge becomes less predominant) and to physical properties of the galaxy. The importance of the bulge with respect to the disk is likely to be connected to the angular momentum distribution in the proto–galaxy and/or to the ratio between the collapse time and the time of the first star formation. In this scenario the disk would form from matter with higher angular momentum with respect to the one which form the bulge. In addition, when the star formation is rapid with respect to the collapse time (and so to the disk formation), the bulge would result to be more prominent than in the case of a rapid collapse.

The circular–speed curve of a galaxy is of fundamental importance because it allows to measure the dynamical mass of a galaxy within a certain radius. The circular speed can be approximately determined as a function of the radius by measuring the redshift of the emission lines of the gas in the disk: either the H_α emission line, due to the ionisation of gas by hot stars, or the 21–cm radio line, produced by hyperfine structure transition in the neutral hydrogen emission line. An observational fact is that rotation curves remain flat out of radii much larger than the extent of the optical disk: for the majority of spiral galaxies no decrease in the circular velocity is observed even beyond radii of $50 − 100$ kpc. The only explanation is to postulate the existence of "dark matter". The correlation between the galaxy's luminosity and the amplitude of its circular speed curve is quantified by the **Tully–Fisher relation** (Tully & Fisher 1977).

Lenticular galaxies

In the middle of the Hubble diagram, at the junction of the elliptical and the spiral galaxies, there are the so called **lenticular galaxies**. These galaxies

are designated as S0 or SB0 according to whether or not they are barred and they are further classified (by Sandage) in three sub–types: for the S0 the sequence is function of the increasing amount of dust in the disk; for the SB0 it depends on the predominance of the bar with respect to the bulge, from large but external to the bulge to thin but crossing it. They are a transition type between the elliptical and spiral galaxies since they have a central bulge and a disk but no spiral arms. The S0 galaxies show a smooth central brightness condensation surrounded by a large, generally rather structure-less, region of less steeply declining brightness. This component appears to be intrinsically flat. The only way to distinguish lenticulars from ellipticals is to look at their brightness profile which results steeper for the ellipticals and showing an exponential trend for the lenticular galaxies. Incidentally, if the resolution is not high enough and the galaxies is face–on it is impossible to detect the disk.

Irregular galaxies

On the extreme right–hand side of the tuning fork Hubble placed the **irregular galaxies**, meaning those objects which are neither spirals nor ellipticals, and can have any number of shapes. They show a lack of symmetry or of well defined spiral arms. An intense star formation is present, as shown by the numerous bright knots that contain O and B stars. The very irregular shapes exhibited by this class of objects can be associated with different causes:

- the interaction with other galaxies: in fact they are frequently the product of two galaxies colliding with each other, or at least affecting each other through gravity;

- the young age: the equilibrium is reached in few rotations (10^9 yr);

- the irregular distribution of the gas and the dust;

- the low density of the stellar background from which the associations of young O and B stars stand out.

The surface brightness profile is well fit by an exponential law like the one of later–type spirals but less smooth with respect to it, due to regions of high star formation, and with a lower surface brightness and smaller disk scalelengths. They are very blue; show a color gradient, being more blue in the center; have low metallicity, a sign that they are weakly evolved systems; they present X–ray emission stronger than in spirals as consequence of the higher number of young stars.

Dwarf galaxies

This class of galaxies does not occupy a particular position in the Hubble diagram and is populated by small galaxies with low luminosity and surface brightness. They are usually divided into **dwarf ellipticals**, dE and **dwarf spheroidal**, dSph. In these systems the star density is everywhere so low that they appear as mere clusterings of faint, but intrinsically moderately luminous, stars. Kormendy & Djorgovski (1989) additionally divided dwarf ellipticals into two classes, compact and diffuse ones. The former are well fitted by a de Vaucouleurs profile and follow at one end of the sequence of profiles for giant ellipticals while the latter are best fitted by an exponential law. It is worth stressing that in contrast to giant ellipticals the diffuse dwarves do not lie on the fundamental plane (Kormendy 1987) and have dynamically insignificant rotational kinetic energy in contrast with normal ellipticals of comparable low luminosity, which appear to be flattened by their rotational kinetic energy. Dwarf galaxies are very common, being the dominant species in nearby galaxy clusters (Wirth & Gallagher (1984), Binggeli, Sandage, & Tammann (1985)) where they can actually be seen, and it is believed that dE could be the commonest type of galaxy in every environment. In addition their distribution on large scales, and eventually their presence in voids, has important consequences for cosmological studies.

In this group are included also the **Blue Compact Dwarves**, an extreme type of dwarf irregulars with star formation bursts concentrated in a very bright region. The star formation activity in this object leads to bubbles of HII gas that expands and can cause significant gas loss.

Hubble suggested an evolutionary interpretation of his diagram that we now know to be wrong: galaxies do not move down the forks of the diagram as they evolve. An easy and convincing explanation is that while spiral galaxies rotate quickly, this is not true for elliptical galaxies and there is no way that an elliptical galaxy could spontaneously begin rotating, so there is no way an elliptical galaxy could turn into a spiral galaxy. Although the failure of Hubble's theory of galaxy evolution, his diagram provides a useful way to classify galaxies and the terminology he introduced is widely used: elliptical galaxies are still referred to as "early–type" and spirals as "late–type". Hubble's original system, with the revision by Sandage, is considered satisfactory as regard to the ellipticals but is regarded as incomplete for the treatment of spirals and inadequate for irregulars. For these reasons more sofisticated and detailed classification schemes were provided. In particular, de Vaucouleurs (de Vaucouleurs 1959) introduced additional classes Sd, Sm and Im; Kormendy (Kormendy 1979) has emphasized the importance for morphological study of the rings and lenses that often occur in disk galaxies, especially barred ones; and more recently, Kormendy & Bender

(1996) revised the Hubble–Sandage tuning fork for ellipticals with the sub–classification into boxy and disky, the Hubble sequence becomes a continuous disk–to–bulge sequence from ellipticals to Sc galaxies.

Besides the rather qualitative classification criteria at the base of the Hubble–Sandage system, we can identify a more quantitative interpretation related to how physical parameters vary along the sequence (see Roberts & Haynes (1994) for an extensive review):

- stellar masses decrease going from ellipticals (10^{12} M$_\odot$) to irregulars (10^8 M$_\odot$);

- the specific angular momentum J/M of baryons increases from ellipticals to spirals;

- mean stellar density of spheroids increases with decreasing spheroid luminosity;

- mean surface brightness of disks increases with luminosity;

- mean age increases from irregulars through spirals to ellipticals: the M/L_B ratio increases from about 2 to 10 and B-V goes from 0.3 to 1;

- cold gas content increases from a fraction of baryonic mass close to 0 in ellipticals up to 0.9 in irregulars passing through values between 0.1 - 0.3 in Sa to Sc;

- hot gas content of the order of few percent of the baryonic mass is only significant in massive ellipticals.

The redshift range $1 < z < 5$ is thought to be a critical age in the emergence of massive galaxies. We still have to learn about the origin of the Hubble sequence of typical massive galaxies we observe in the local universe, since the evolution back to $z = 1$, already studied from the ground and with the HST, is too small. The sub–kpc resolution of the ACS at optical wavelengths is sufficient to classify galaxies at high redshifts (Abraham et al. (1996), van den Bergh (1996), Snail et al. (1997), Brinchmann et al. (1998)) in a scheme which is relatable to the classification of galaxies at the present epoch.

1.5   Bulge–to–disk decomposition

Starting from the introduction of the Hubble's tuning fork diagram the visual classification of galaxies has a venerable tradition in optical astronomy, although it presents several weaknesses. First and foremost it is a subjective process; second, it is not clear how it can be useful with respect to high–z galaxies. Due to limited spatial resolution, larger and larger galaxy
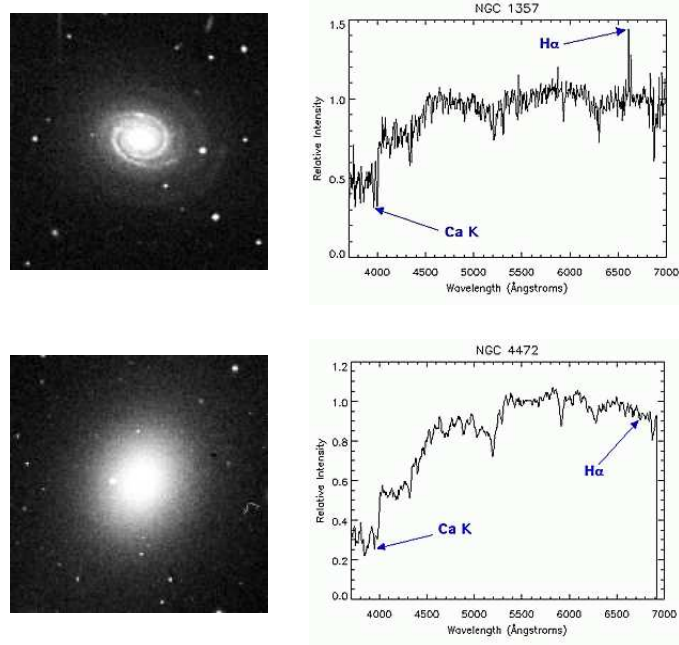
Figure 1.9: Image and relative spectra of a spiral (upper–panel) and an ellipical (lower–panel) galaxies from the Sloan Digital Sky Survey.

internal structures such as spiral arms and tidal tails get smoothed out with increasing redshift, introducing significant classification biases. These are the main reasons for the introduction of a quantitative approach to morphological galaxy classifications. To probe the structure of galaxies a number of parametric (model–based) and non parametric quantitative classifiers have been developed. Non parametric classifiers include the $C - A$ system (Watanabe, Kodaira, & Okamura (1985), Abraham et al. (1994), Conselice et al. (2000)), artificial neural nets trained from visual classification sets (Odewahn 1995) and self–organizing maps (Naim 1997). Parametric classifiers include radial multi–gaussian deconvolution (Bendinelli (1991), Fasano et al. (1998)), Shapelet decomposition (Kelly & McKay 2004), and bulge–to–disk decomposition (Schade et al. (1995), Schade et al. (1996), Ratnatunga, Griffiths, & (1999)). Basic to most systems of classification of galaxy types is the recognition of two fundamental components of galaxy structure: a more or less flat disk of stars, and often of gas and dust; and a generally spheroidal component. Most galaxies possess both structures, but there are a lot of objects without a disk: ellipticals; and without a noticeable spheroidal component: some late–type spirals and irregulars. If we assume that these two components reflect different formation mechanisms, their relative importance must

be fundamental. Among disk galaxies themselves there exists a dichotomy between those rich in gas and dust and resulting star formation, spiral and irregulars, and those in which this activity is virtually absent, S0 galaxies.

It is known that there is a segregation between the population of the low–density field, largely spirals, and the densest regions of clusters of galaxies, largely composed of S0 and ellipticals. Many interpretations have been proposed so far: common origin of all galaxies coupled with the subsequent evolution of one type to another; major differences are native in the formation process or reflect evolution at a relatively early epoch.

What is secure is that galaxies span a wide range of morphology and luminosity, and a useful way to quantify them is to fit their light distribution with parametric functions. The de Vaucouleurs law and the exponential profile became standard functions to use after de Vaucouleurs (1948) found many ellipticals to have a $r^{1/4}$ light distribution, while Freeman (1970) found later–type galaxies to be well described by a de Vaucouleurs bulge plus an exponential disk. Since then, the empirical techniques of galaxies fitting and decomposition have led to a number of notable advances in understanding galaxy formation and evolution. These include investigation into the Tully–Fisher relation (Tully & Fisher 1977), the fundamental plane of spheroids (Faber et al. (1987), Dressler et al. (1987), Djorgovski & Davis (1987), Bender, Burstein & Faber (1992)), the morphological transformation of galaxies in cluster environments (e.g. Dressler (1980), van Dokkum & Franx (2001)), the bimodality of galaxy nuclear cusps (Lauer et al. (1995), Faber et al. (1987)) and its implication for the formation of massive black holes (Ravindranath et al. 1995), and the cosmic evolution of the galaxy morphology (Lilly et al. (1998), Marleau & Simard (1998)).

There are two general types of galaxy fitting: one–dimensional (1D) fitting of surface brightness profiles (e.g. Kormendy (1977), Burstein (1979), Boroson (1981), Kent (1985), Baggett, Baggett & Anderson (1998)), and two–dimensional (2D) fitting of galaxy images (e.g. Shaw & Gilmore (1989), Byun & Freeman (1995), de Jong (1996b), Wadadekar, Robbason, & Kembhavi (1999), Khosroshahi, Wadadekar, & Kembhavi (2000), Peng et al. (2002), Simard et al. (2002)), with each its own tradeoffs and benefits. The main problem in 1D fitting is how to obtain a radial surface brightness profile from a 2D image. A common practice is to use isophote fitting, which is a powerful technique when performed on well–resolved images, because it averages over elliptical annuli to increase the signal to noise (S/N) at a given radius. However, since many galaxies show isophote twists and changing ellipticity as a function of radius, the galaxy profile is extracted along a radial arc which is ill–defined. Commonly a direct 1D slice across the image is used: Burstein (1979) argues that only cuts along the major axis should be used in bulge–to–disk (B/D) decompositions; Ferrarese et al. (1994) point out that galaxies with power law central profiles may have different profiles along the major and the minor axis. Non–uniqueness in the 1D decompo-

sition is caused by the fact that the galaxy bulge and disk may appear to merge smoothly and the parameters that are obtained depend to some extent on how the fitting is done. In 2D fitting, isophote twists and ellipticity changes provide additional constraints to break those degeneracy. Therefore, the only reliable way to choose between possible bulge–to–disk decompositions is to fit the models directly to the 2D surface photometry, rather than to surface brightness profiles. 2D structural decomposition of galaxy images show that it is possible to obtain a reliable fit even for those objects which reveal large isophotal twists and changes in shapes. These morphological complexities are often signatures of distinct galaxy components: evidence of galaxy substructures, too subtle to be seen in the original image, can be discovered after the major components are removed. The substructures include features such as nuclear point sources, low–level dust patterns, stellar disks, stellar bars, and other distinctive large–scale components. Even giant elliptical galaxies, often regarded as featureless objects, may reveal unusual shapes and slight misalignment of the sub–components. The physical interpretation of these features is not yet clear, although it is believed that the amount of distortion in a galaxy may give clues to its evolutionary history.

Spectroscopic classification

It is worth noticing that not only photometric but also different spectroscopic features of galaxies can be used to classify them (see Figure 1.9). In particular, spectroscopic classification is based on the relative strengths of some absorption and emission lines. When we observe the spectrum of a galaxy, we are really looking at the combination of spectra from the millions of stars in the galaxy. Studying the features of a galaxy spectrum tells about the types of stars the galaxy contains and the relative abundances of each type of star. Since galaxies do change as they age, older galaxies have few young blue stars while younger ones have many HII regions, where stars are forming, which are clearly visible in the red part of their spectra. Some modern studies have attempted to use spectroscopic features to classify galaxies into morphological types (Bromley et al. (1998), Folkes et al. (1999)) An advantage is that it makes it possible to analyse large samples. Although a general correlation is known between spectroscopic and Hubble morphologies, the samples derived from photometric and spectroscopic methods are considerably different. In particular, classification using spectroscopic features or colours is sensitive to small–scale star formation activity, now or in the recent past, in early–type galaxies.

Chapter 2

The Sloan Digital Sky Survey

The Sloan Digital Sky survey (SDSS, York et al. (2000)) is one of the most ambitious observational astronomical projects ever undertaken. It aims to map about one–quarter of the sky, determining the position and absolute magnitude of more than 10 billion objects and the redshifts of more than a million galaxies and quasars. We briefly describe in this section the main technical aspects of the survey and we point our attention to some parameters of particular interest for the analysis we performed.

2.1   The survey

The SDSS project is a digital photometric and spectroscopic survey that will cover one–quarter of the celestial sphere toward the northern Galactic cap and produce a smaller area ($\sim 225\,\mathrm{deg}^2$) but much deeper survey toward the southern Galactic cap. It consists of an imaging survey of π steradians of the northern sky in 5 photometric bands (u, g, r, i and z) centered at (3540, 4770, 6230, 7630 and 9130 Å) down to (22.0, 22.2, 22.2, 21.3 and 20.5 mag). The filter system, described by Fukugita et al. (1996), spans the entire optical range from the atmospheric ultraviolet cutoff in the blue to the sensitivity limit of silicon in the red. The sensitivity of the CCD chips in the SDSS's five filters is shown in Figure 2.1 as a function of wavelength. The filters are less sensitive when looking through the Earth's atmosphere. A small overlap between the filters is also present. The survey is carried out in a drift–scan mode using a dedicated 2.5 m telescopes, an imaging mosaic camera with 30 CCDs (Gunn et al. 1998), two fiber–fed spectrographs and a 0.5 m telescope for the photometric calibration (Hogg et al. (2001), Smith et al. (2002)). Individual fiber plug plates are drilled for each field to accommodate 640 optical fibers of $3''$ entrance diameter, which feed the spectrographs. The survey sky coverage of about π steradians ($10,000\,\mathrm{deg}^2$) will result in photometric measurements of $\sim 5 \times 10^7$ galaxies, as well as $\sim 10^6$ moderate–resolution ($\lambda/\delta\lambda = 1800$) spectra of galaxies brighter
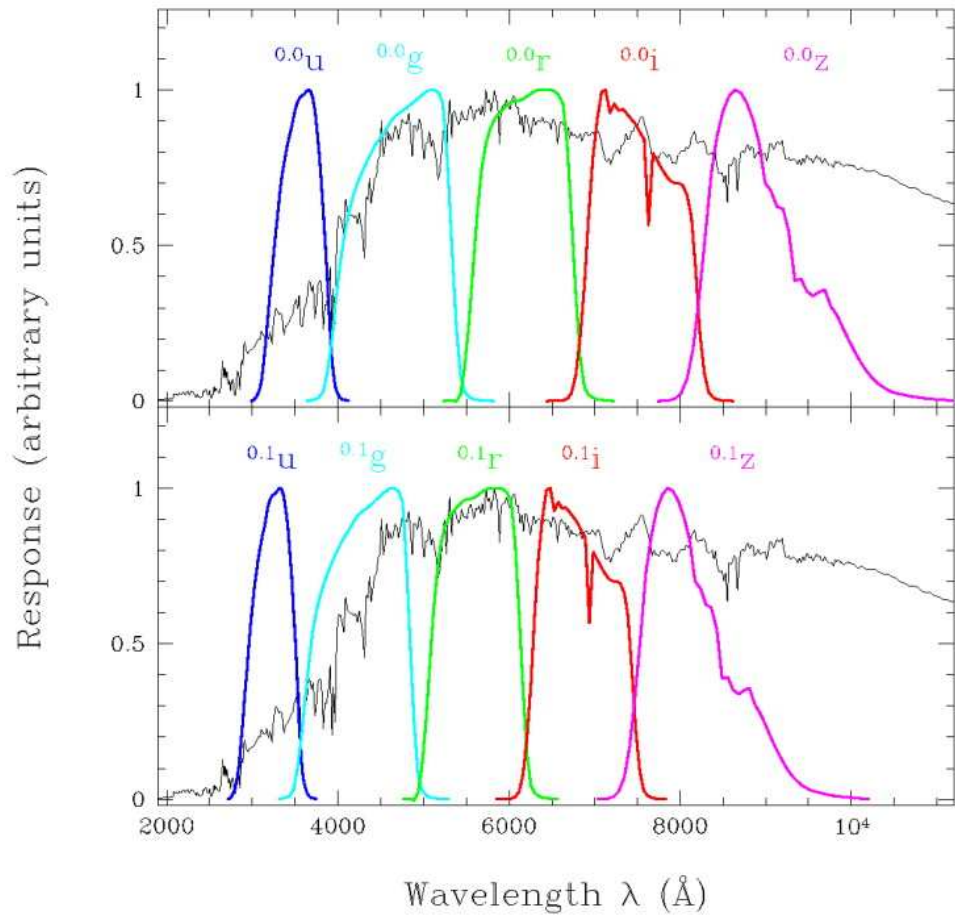
Figure 2.1: (from Blanton et al. 2003b). SDSS filter system (top panel) and SDSS filter system shifted by 0.1 (bottom panel).

than $r \approx 17.8$, covering the wavelength range 3800–9200 Å. The imaging data are processed with an automatic software pipeline called **PHOTO** (Lupton et al. (2001), Lupton et al. (2002)) while the basic spectroscopic parameters are obtained by the spectroscopic pipeline **IDLSPEC2D** (written by D.Schlegel and S. Burles) and **SPECTRO1D** (written by M. SubbaRao, M.Bernardi and J. Frieman). The morphological information from the images currently allows robust star–galaxy separation to ~ 21.5 mag (Lupton et al. 2001; Yasuda et al. 2001) The software identifies individual features in the spectra such as emission and absorption lines. Comparing the observed lines to a list of laboratory measurements, it is possible to infer the relative velocity of the galaxy or star with respect to Earth. From this we derive the distance and eventually create a three–dimensional map of the universe.

2.2 Derived galactic quantities

Galaxies do not have sharp edges or a unique surface brightness profile. Therefore, their emitted flux can be measured in various ways. The Sloan photometric pipeline calculates three different types of magnitudes for each object: model magnitude, Petrosian magnitude and PSF magnitude. Model magnitudes are obtained by fitting a de Vaucouleurs plus exponential model, convolved with the local PSF, to the two dimensional image of the galaxy in the r band. Total magnitudes are determined from the better fit of the two parametric functions. Galaxy colours are obtained by applying the best fit model of an object in the r band to the other bands and measuring the flux in the same effective aperture. Due to a bug in the code, model magnitude are systematically under–estimated by about 0.2 magnitudes for galaxies brighter than 20 magnitude, and accordingly the measured radii are too large. The Petrosian magnitudes have the advantage to measure a constant fraction of the total light of a galaxy, independent of the surface brightness limit. The Petrosian radius r_P is defined to be the radius where the local surface brightness averaged in an annulus equals 20 per cent of the mean surface brightness interior to this annulus

$$0.2 = \frac{2\pi \int_{0.8r_P}^{1.25r_P} \frac{I(r)r\,dr}{\pi r^2 (1.25^2 - 0.8^2)}}{2\pi \int_0^{r_P} \frac{I(r)r\,dr}{\pi r^2}}, \tag{2.1}$$

where $I(r)$ is the azimuthally averaged surface brightness profile. The Petrosian flux is then defined as the total flux within a radius of $2r_P$,

$$F_P = 2\pi \int_0^{2r_P} I(r)\,dr. \tag{2.2}$$

With this definition the Petrosian magnitude is about 98 per cent of the total flux for an exponential profile and about 80 per cent for a de Vaucouleurs profile. The Petrosian magnitudes are the best measure of the total light for bright galaxies but fail to be a good measure for faint objects. The reason for this is that for faint objects the effect of the seeing on Petrosian magnitude is not negligible. As the galaxy size becomes comparable to the seeing disk, the Petrosian flux is close to the fraction measured within a typical point spread function (PSF), which is about 95 per cent. This means that the flux is reduced for a galaxy with an exponential profile and increased for a galaxy with a de Vaucouleurs profile.

2.3   Interesting results of the SDSS

The primary science goal behind the SDSS is the characterization of the large–scale structure of the universe. Nevertheless the survey has already had a significant impact on several branches of astrophysics, from the investigation of asteroids in our Solar System to the discovery of the most distant known objects in the universe.

In the field related to this thesis, the SDSS galaxy data have already been used in a number of studies. Blanton et al. (2003b) calculate the galaxy luminosity function and its dependence on galaxy surface brightness, morphology and intrinsic colours. The galaxy number counts are derived by Yasuda et al. (2001) while the effect of galaxy–galaxy weak lensing is measured by Fischer et al. (2000). The clustering of galaxies in the SDSS and their three–dimensional power spectrum are analysed in a series of papers (Kayo et al. 2004; Tegmark et al. 2004; Connolly et al. 2002; Dodelson et al. 2002; Zehavi et al. 2002). A sample of $9,000$ galaxies is used by Bernardi et al. (2003a,b,c,d) to study different scaling relations of early–type galaxies. Strateva et al. (2001) and Shimasaku et al. (2001) investigate in detail the colour, effective size, and concentration parameter of SDSS galaxies, using a sample of 456 bright objects visually classified into seven morphological types. Kauffmann et al. (2003) develop a method to estimate the star formation history, dust attenuation and stellar mass of a galaxy based on its spectral features, and obtain these information for a sample of $122,808$ SDSS galaxies. In an interesting paper Shen et al. (2003) study the size distribution of galaxies and its dependence on their luminosity, stellar mass and morphological type. The relation between stellar mass and gas–phase metallicity is investigated by Tremonti et al. (2004).

Chapter 3

Luminosity in Bulges and Disks

In this chapter we describe the algorithm we use in order to perform a detailed bulge–to–disk (B/D) decomposition on a complete magnitude limited sample of roughly 1800 morphologically classified galaxies in the Sloan Digital Sky Survey (SDSS). The total luminosity in the galactic disk and bulge components is computed and a constraint is given. The structural parameters obtained for galaxies of the same morphological type using different parametric functions for the decomposition are consistent in the different modellings and bands. The luminosity function of Blanton et al. (2003) and the results of our decomposition in the Sloan i and r bands are used to measure the luminosity density in bulges and disks at z=0.1 for a cosmological model with $\Omega_M = 0.3$, $\Omega_\Lambda = 0.7$ and $h = 0.7$. We conclude that $(55 \pm 2)\%$ of the total light in the local universe resides in the disk component.

3.1 Introduction

In June 2001 the Sloan Digital Sky Survey (SDSS; York et al. (2000)) released its Early Data Release (EDR;Stoughton et al. (2002)), roughly 462 square degrees of imaging data collected in drift scan mode in five different band-passes (u, g, r, i and z). The EDR contains around a million galaxies distributed within a narrow strip of 2.5 degrees across the equator. As the strip crosses the galactic plane, the data are divided into two separate sets in the North and South galactic caps. The SDSS has the ambitious project to image a quarter of the Celestial Sphere at high Galactic latitude as well as to obtain spectra. We therefore have the advantage, in comparison to previous works, of using a larger database, which allows to increase the statistics, and good photometric and spectroscopic data.

Models of galaxy formation make an attempt to explain the fundamental observation that galaxies typically have two components, a bulge and a disk,

with different photometric and dynamical properties.

To determine the chronology of bulge and disk formation and the relative contribution of these two components at different cosmological epochs is a fundamental issue in observational cosmology since it provides us with important constraints which eventually will give us the possibility to discriminate between competing scenarios of galaxy formation and evolution. In models where bulges form first and disks form later there is no obvious reason to connect their formation. In this hypothesis the ratio of spheroids luminosity to total luminosity measures the efficiency of the first burst of star formation. If instead disks form from bulges by secular evolution a strong correlation is expected. A correlation might also be expected in the hierarchical infall and small merger models.

In this chapter we apply an algorithm for morphological decomposition of galaxy images to a sample of SDSS galaxies. We use the results of this decomposition to study the relations of bulge and disk properties in galaxies in the local universe. This is the starting point for a further study of these relations at higher redshifts in order to trace their evolution.

The luminosity function of galaxies (see Binggeli, Sandage, & Tammann (1988) for a comprehensive review), is defined as the number of galaxies per unit volume, per absolute magnitude (or luminosity) interval and eventually for each morphological type. It is an important observational "ingredient" for cosmology as well as for galaxy formation and evolution. It contains fundamental information about the power spectrum of primordial density fluctuations, the physical processes which convert mass into light (e.g. gravitational collapse, cooling, star formation), the mechanisms that destroy/generate galaxies or change their morphology such as tidal interaction, merging and ram pressure stripping.

The determination of the luminosity function, and therefore of the analytic form which best approximates the galaxies' absolute luminosity distribution, is complicated by the following factors: the irregular distribution of galaxies in space, so that it is necessary to average over very extended regions; the detection limits, so that we miss fainter objects; the morphological segregation of galactic types according to the environment density (Dressler 1980). The universality of the luminosity function is much debated. It is known that it changes for different morphological types (Binggeli, Sandage, & Tammann (1988); Nakamura et al. (2003)) and in different environments (e.g. field, cluster, various regions in the cluster) (Efstathiou & Rees (1988); Zucca et al. (1997)). Nevertheless it can be used to compare the morphological content and the deviation from a standard luminosity distribution. The most popular parameterization to fit the data was proposed by Schechter (1976):

$$\Phi(L)dL = \Phi^* \cdot \left(\frac{L}{L^*} \right)^\alpha \cdot \exp^{-\left(\frac{L}{L^*} \right)} \cdot \frac{dL}{L^*} \qquad (3.1)$$

Sample	Subsamples								Total
	$0 \leqslant T < 1$ E	$1 \leqslant T < 2$ S0	$2 \leqslant T < 3$ Sa	$3 \leqslant T < 4$ Sb	$4 \leqslant T < 5$ Sc	$5 \leqslant T < 6$ Sd	$T = 6$ Irr	$T = -1$ unclassified	
Photometric	487	417	313	312	232	48	25	28	1862
Spectroscopic	413	363	272	262	197	42	16	23	1588

Table 3.1: Visual classification of our photometric and spectroscopic samples into morphological subsamples.

where α gives the slope of the luminosity function at faint magnitudes; $L^*(h^{-2}L_\odot)$ is the characteristic luminosity above which the number of galaxies decreases exponentially; and $\Phi^*(h^3 Mpc^{-3})$ characterizes the galaxy density.

This powerful tool is used to investigate the contribution of disks and bulges to the total light in the local universe.

This chapter is organized as follows. In section 3.2 we present the sample used and the galaxy selection. In section 3.3 we briefly describe the fitting algorithm and the parametric functions used to fit the galaxy light distribution and we show how the image reduction was performed. In section 3.4 the resulting parameters are presented for those galaxies which could be successfully fitted. The luminosity in bulges and disks and its implications for the galaxy formation scenario are investigated. Space is given in section 3.5 for the comparison of these results in different bands and for different parametric functions in the fitting procedure. The accuracy of the fits is also estimated.

Throughout this chapter, unless otherwise stated, we assume a Hubble constant of $H_0 = 70 \ km \ s^{-1} \ Mpc^{-1}$ and an $\Omega_M = 0.3$, $\Omega_\Lambda = 0.7$ cosmology in calculating distances and luminosities.

3.2   Observational data

3.2.1   Galaxy sample

In the following analysis we are using the sample of galaxies defined by the Japanese Participation Group (JPG, Yasuda et al. (2001)). It is a homogeneous sample obtained from the Sloan Digital Sky Survey for northern equatorial stripes. The region of the sky included in the sample covers an area of 229.7 square degree for $145.15° \leqslant \alpha \leqslant 235.97°$ and $-1.27° \leqslant \delta \leqslant 1.27°$.

The sample is limited to bright galaxies with $r \leqslant 15.9$ after galactic reddening correction, since eye classification cannot be made confidently beyond this magnitude.

All the 1862 galaxies in the sample are classified by eye into 7 morphological classes according to the *Hubble Atlas of Galaxies* (Sandage 1961), by the JPG using the g band image of each galaxy. The mean is given as the final type, but also the rms of 4 individual classifications is quoted. The
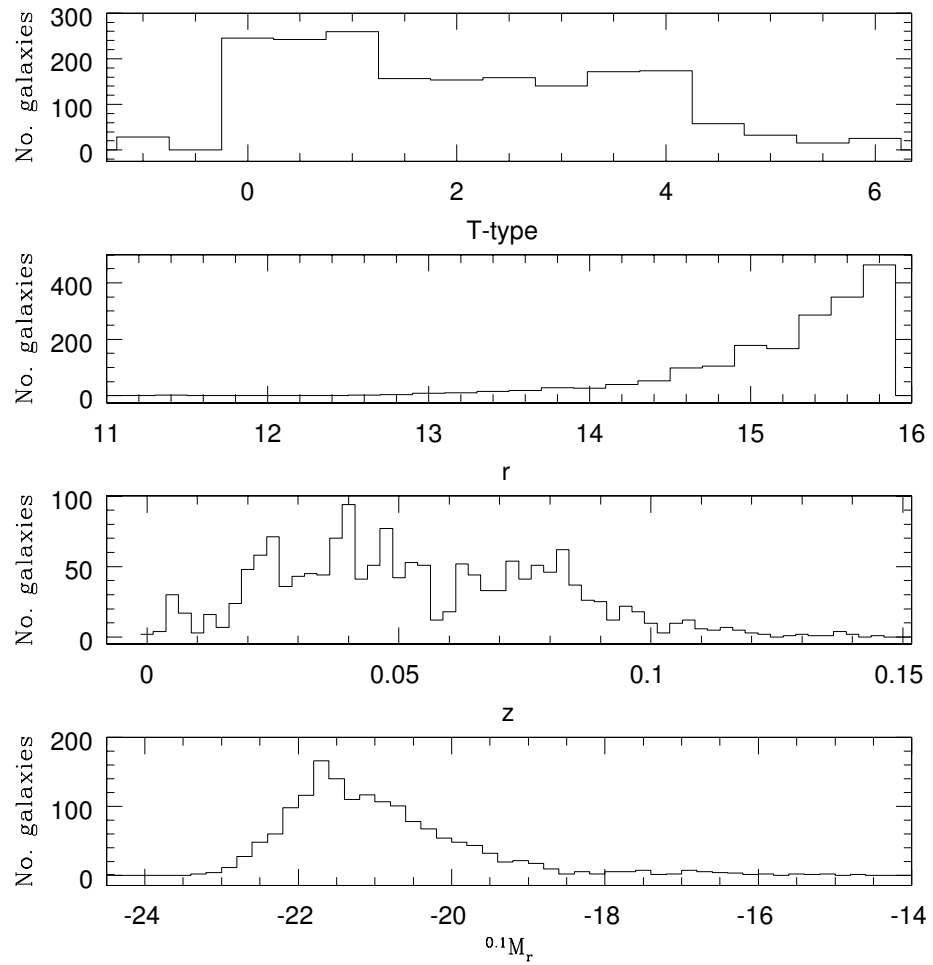
Figure 3.1: The distribution of galaxies versus morphological type (upper panel) and against Petrosian magnitude in the r band after extinction correction (second panel) are shown for the 1862 galaxies in the sample. The redshift (third panel) and absolute magnitude (lower panel) distributions are given for the 1550 galaxies in the sample for which we have spectroscopic information.

classifications agree within $\Delta T \leqslant 1.5$. The morphological types given by the *Third Reference Catalogue of Bright Galaxies* (de Vaucouleurs et al. 1991) are also reported. The seven resulting subsamples include galaxies with the same morphological type going from early types, ellipticals (E) and lenticulars (S0), to early–type spirals (Sa, Sb), late–type spirals (Sc, Sd) and irregulars (Irr). For 1588 galaxies in our sample out of 1862 we have spectroscopic information. A schematic view of our sample and subsamples is given in Table 3.1. We refer to (Nakamura et al. 2003) for further details on this sample.

3.2.2   Photometric and spectroscopic data

Two important quantities used in this analysis are taken from the Sloan data base: the redshift and the Petrosian magnitude. The first is obtained by the spectroscopic pipelines **idllspec2d** (written by D.Schlegel & S.Burles) and **spectro1d** (written by M. SubbaRao, M. Bernardi and J. Frieman), and the distribution of galaxies with respect to z is shown in the third panel of Figure 3.1. The second is obtained by the automatic **Photo** pipeline (see Lupton et al. (2001, 2002)) and it is a modified form of the Petrosian system for galaxy photometry designed to measure a constant fraction of the total light. Three related quantities also used in this work are R_{50} and R_{90}, defined as the radii which include respectively 50 and 90 percent of the Petrosian flux, and the concentration index $c \equiv R_{90}/R_{50}$. The second panel of Figure 3.1 shows the distribution of galaxies with respect to their Petrosian magnitude after correction for foreground Galactic extinction using the reddening map of Schlegel, Finkbeiner, & Davis (1998). The extinction–corrected Petrosian magnitudes are used throughout this paper.

3.3   Analysis

3.3.1   The fitting algorithm

The structural properties of galaxies are examined using **Gim2D** (Simard et al. 2002), a two–dimensional photometric decomposition fitting algorithm able to automatically decompose all the objects in an input image as the sum of a Sérsic and an exponential profile.

Being aware that the usual separation of a galaxy into a bulge and a disk component only tells us about the light distribution and it does not claim to give any information concerning their internal kinematics, we perform a multi–component model fit to the two dimensional (2-D) surface brightness profile of each galaxy in our sample.

It is well known that the bulge component of a galaxy can be modeled by a Sérsic profile of the form:
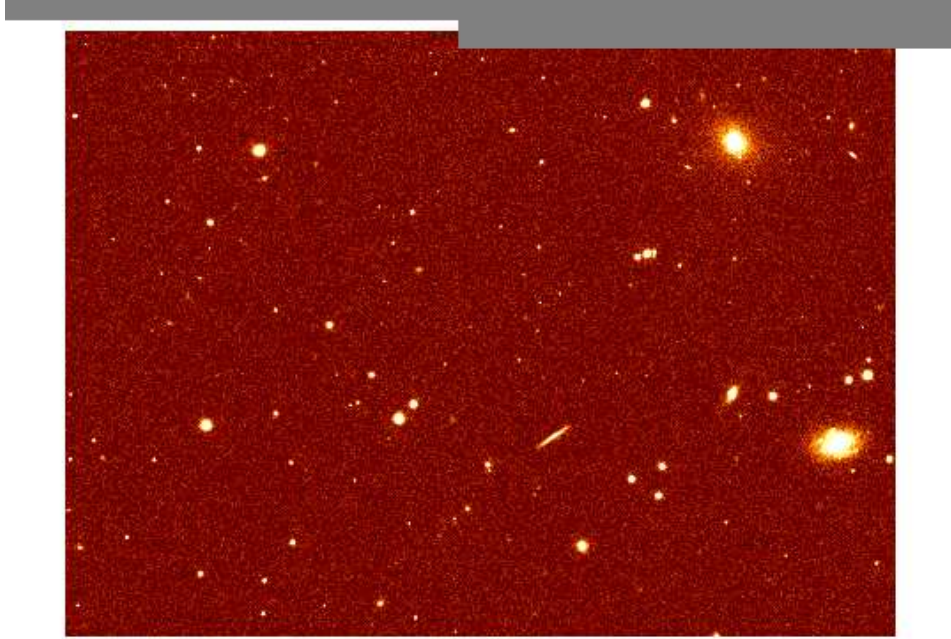
Figure 3.2: Example of a Sloan corrected frame.

$$\Sigma(r) = \Sigma_e \cdot \exp\left\{-b\left[(r/r_e)^{1/n} - 1\right]\right\} \qquad (3.2)$$

where $\Sigma(r)$ is the surface brightness at radius r along the semi-major axis in linear flux units per unit area, and Σ_e is the effective surface brightness. The parameter b is related to the Sérsic index n and set equal to $1.9992n - 0.3271$ so that r_e stays the projected radius enclosing half of the light in this component (Sersic 1968; Ciotti 1991). The bulge is often fitted by a more specific function, the de Vaucouleurs $r^{1/4}$ law, obtained by setting the Sérsic index equal to 4. In the following analysis we use a Sérsic index ranging from 0.2 to 4.

This choice is driven by the knowledge that when the generalized de Vaucouleurs law is fitted to data for a low–luminosity elliptical galaxy, the best fitting value of n is likely to be smaller than 4 while for very bright ellipticals, mostly cD systems, values of n in excess of 4 are usually found and we do not expect these objects in our sample.

The disk component is generally well described by an exponential profile:

$$\Sigma(r) = \Sigma_0 \cdot \exp(-r/h) \qquad (3.3)$$

where Σ_0 is the central surface brightness and h the disk scalelength.
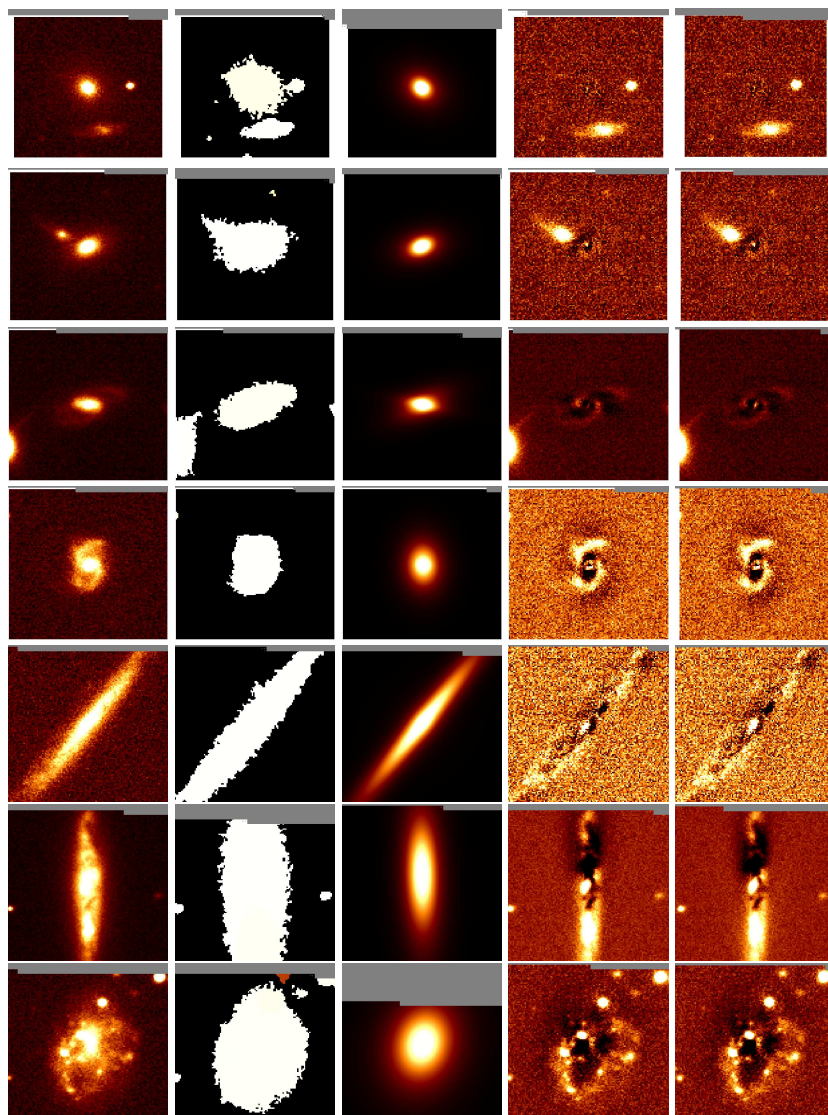
Figure 3.3: The science image, the mask, the model and the residual images for the de Vaucouleurs plus exponential and Sérsic plus exponential modelling in the g band (from the left–hand side to the right–hand side) for the seven morphological classes (E, S0, Sa, Sb, Sc, Sd, Irr, respectively from the top to the bottom) considered in this study.

These laws are purely empirical fitting functions and others might provide equally good fits to a galaxy profile using different parameters for the bulge–to–disk decomposition. In our model we have 12 morphological parameters and others could be introduced to model other features (e.g bars, spiral arms, etc.). Since the computational time would dramatically increase and such decompositions become somewhat arbitrary, we found our choice to be a good compromise between available computing resources, stable results, and detailed decomposition.

The theoretical profile of each galaxy is deconvolved with a point spread function (PSF) which has been measured from stars on each galaxy frame. The PSF is highly variable across a field (Stoughton et al. 2002) and for this reason it is important to use a PSF which is centered at the center of the galaxy, at

$$(nxpsf - 1)/2 + 1 \qquad \text{and} \qquad (nypsf - 1)/2 + 1 \qquad (3.4)$$

where $nxpsf$ and $nypsf$ are the dimensions of the PSF image. And integrating the sum of Equations 3.2 and 3.3 with the best fitting parameters we obtain the PSF–deconvolved half–light radius r_{hl}, being the radius which includes half of the light of the object.

3.3.2 Image reduction

We perform our analysis starting from a Sloan corrected frame, an example of which is shown in Figure 3.2. These are the imaging frames with flat–field, bias, cosmic-ray, and pixel–defect corrections applied. To proceed with the fitting of galaxy images we need a catalogue of the sources to be analyzed in each field and their x-y centroid position, given by the Sloan data base, to detect them in the field. The **SExtractor** galaxy photometry package version 2.2.2 (Bertin & Arnouts 1996) is used to perform an initial estimate of the local sky background level and to measure the isophotal area of the object in pixels above the detection threshold. As SExtractor performs galaxy photometry, it constructs a segmentation, or mask, image in which pixels belonging to the same object all have the same value and sky background pixels are flagged by zeros. The 2–D profile fit is done on the image pixels belonging to the same pixel value segmentation image. Each decomposition is then subtracted from the input image, and the results are a "galaxy free" image and a catalogue of quantitative structural parameters. The detection threshold is set to 1.5 σ_{bkg} and the required minimum object area above that threshold to 10 pixels, large enough to ensure a good discrimination between sky background and galaxy flux in the bulge–to–disk decomposition.

When the fitting algorithm starts to sample the 12-dimensional parameter space, it is taking into consideration not only the pixels in the mask which belong to the galaxy but also an extra 5 pixels around it in order to

account for faint structures belonging to the galaxy which extend outside the flagged region. Once convergence is achieved, the galaxy light model that we obtain for the PSF–convolved galaxy image is the sum of an exponential disk and a Sérsic, or de Vaucouleurs, bulge.

There is a maximum of twelve parameters which can go into the galaxy light model and that we can retrieve as output of our decomposition: the total flux of the object in digital units (DU); the bulge to total light ratio B/T, defined as the flux in the bulge component compared to the total one. The value of $B/T = 1$ corresponds to a pure bulge system while $B/T = 0$ to a pure disky object for which no bulge component is modeled. The bulge effective radius r_e, being the radius which contains half of the light of this component, and the disk scalelength h are given in pixels. The disk inclination angle i is defined so that $i = 0$ for face–on disks and $i = 90$ for edge–on ones. The axial ratio of this component is then given by $(b/a)_{disk} = cos(i)$. The bulge ellipticity e is given by $e = 1 - (b/a)$ where b and a are semi-minor and semi-major axis length. Bulge and disk position angles (hereafter PA) are the angles between the major axis of the ellipses and the north–south axis in the sky, measured clockwise. The Sérsic index n can also be left as a free parameter in the fit. The last three parameters are the x and y centroid pixel shifts dx and dy in pixel and the background level db in DU.

As mentioned above the Sloan point spread function varies considerably across the field. In order to perform an accurate bulge–to–disk (B/D) decomposition we choose to provide a PSF defined at the center of the image for each individual galaxy in the sample.

Finally a photometric calibration and the redshift are required to retrieve physical quantities from the output of the B/D decomposition code.

3.4 Results

3.4.1 Galaxy structural parameters

As described above the surface brightness profile of galaxies can be quantified by the use of empirical luminosity laws such as the $r^{1/4}$ law associated with the bulge population and an exponential profile describing the disk of galaxies.

The bulge–to–disk decomposition is performed on thumbnail images, two for each galaxy, extracted around the object detected by SExtractor. The area of these postage stamp images is chosen to be 10 times larger than the 1.5 σ_{bkg} isophotal area. The first thumbnail is extracted from the corrected frame and the local background measured by SExtractor is subtracted from it, while the second is taken from the mask image. The N–parameter space is sampled by the algorithm and once convergence is achieved the parameters

for the best model are given. The derived parameters for the bulge and disk components are shown in Figure 3.16–3.19.

Error estimates and goodness of fit

As a result of the photometric decomposition, for each galaxy, we obtain a PSF–convolved model image, a residual image, the best parameter values and the reduced chi–square χ^2 for the fit. When the algorithm converges the region of parameter space where the likelihood is maximized is sampled and these iterations are used to compute median values as well as confidence limits for each model parameter. For each free parameter in our model we end up with the best parameter value and the 99% confidence upper and lower bound.

The computed χ^2 turns outs to be not too sensitive to whether problems occur in the decomposition (i.e. a wrong point spread function) or the decomposition reliably describes the light distribution in the galaxy. Nevertheless the χ^2 can be taken into consideration for having a first, rough idea on the success of the modelling: a $\chi^2 > 0.35$ is used in this work to eliminate galaxies for which the parametrisation cannot be entirely trusted.

With the aim to better understand the goodness of the fit we introduce two estimators, G_1 and G_2. They are defined respectively as the ratio between the light in the residual image over the model luminosity and the absolute value of the residual light over the luminosity of the model image. More in detail for each postage stamp image we consider only the region which is flagged as belonging to the galaxy in the segmentation image generated by SExtractor. We then look at the same area in the model and residual images obtained from the modelling procedure. Working on the single pixels (ij), by definition the total counts in the science image $(\sum O_{ij})$ and in the model image $(\sum M_{ij})$ are due to the light of the galaxy plus a uniform sky $(\sum S_{ij})$, which is the same in the two images. The total counts in the residual image simply result in the difference between the luminosity of the observed and modelled galaxy $(\sum D_{ij} = \sum O_{ij} - \sum M_{ij})$. Our definition can consequently be formulated as:

$$G_1 = \frac{\sum D_{ij}}{L_{model}} \qquad \text{and} \qquad G_2 = \frac{\sum |D_{ij}|}{L_{model}} \tag{3.5}$$

Figure 3.4–3.7 show the distribution of galaxies with respect to these quantities and their correlation with the galaxy absolute magnitude. The results of this analysis are presented for the two relevant parametrisations chosen for galaxies in the i band, the r band not presenting significant differences. The G_1 parameter is narrowly distributed around zero, a bit shifted towards positive values. We infer that there is no particular trend of the modelling procedure to subtract too much or too little. The distribution of the absolute
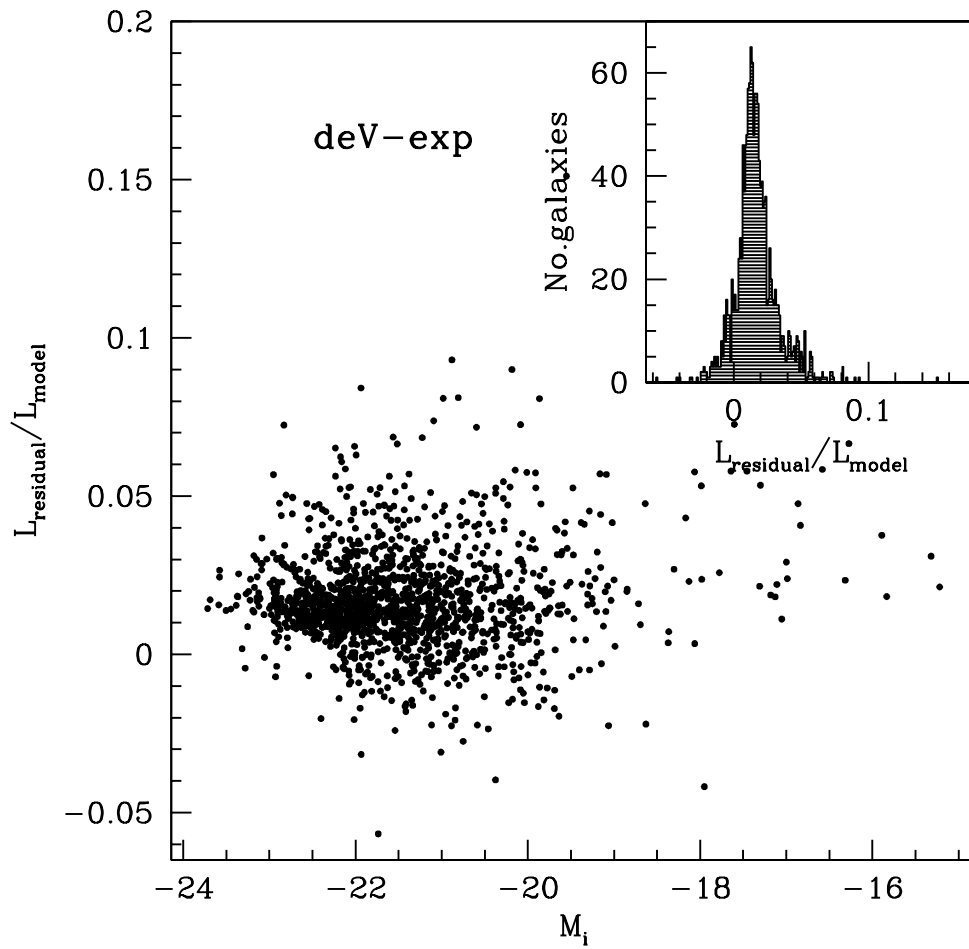
Figure 3.4: The fraction of light in the residual image with respect to the total flux in the model image is plotted against the total absolute magnitude of the galaxy in the i band. The histogram in the top–right–hand corner shows the distribution of galaxies versus the parameter G_1, which we are using as an estimator of the quality of the fit. The points are the 1469 galaxies which were modelled in the i band using a de Vaucouleurs profile for the bulge and an exponential for the disk.
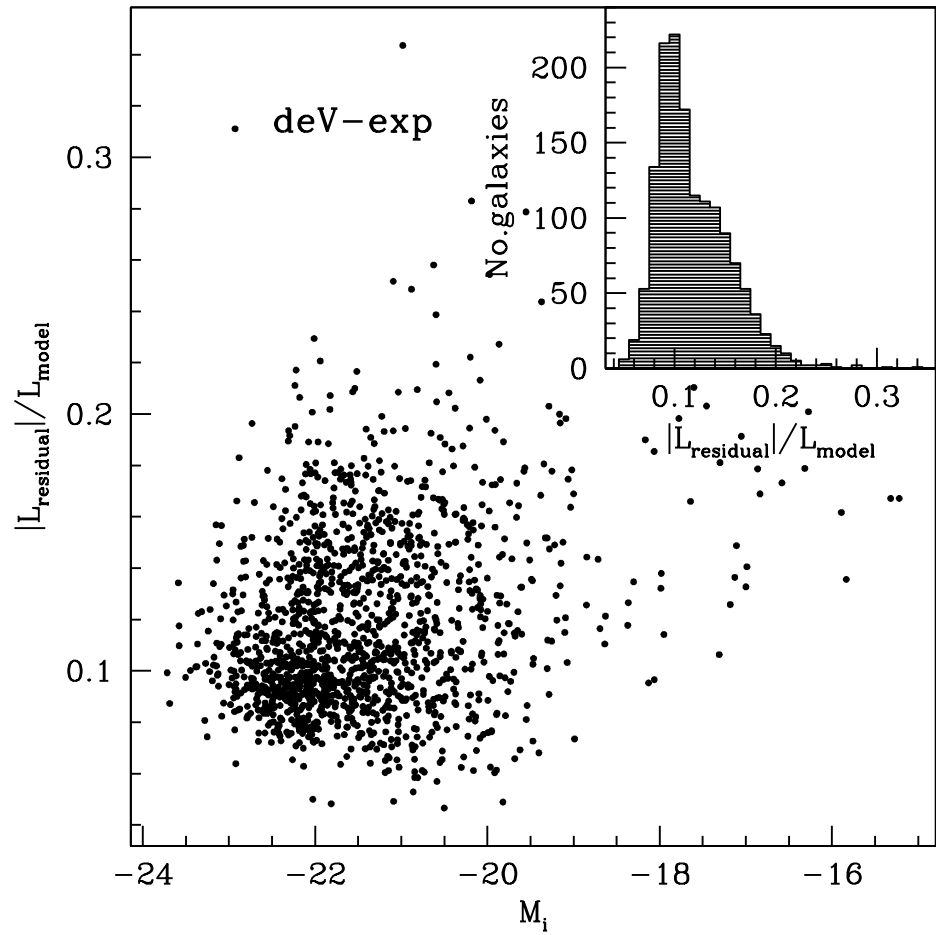
Figure 3.5: The absolute value of the fraction of light in the residual image with respect to the total flux in the model image is plotted against the total absolute magnitude of the galaxy in the i band. The histogram in the top–right–hand corner shows the distribution of galaxies versus the parameter G_2, which is one of our estimator of the quality of the fit. The points are the 1469 galaxies which were modelled in the i band using a de Vaucouleurs profile for the bulge and an exponential for the disk.

Figure 3.6: As Figure 3.4 but for the choice of a more general Sérsic profile for the bulge and an exponential for the disk.

Figure 3.7: As Figure 3.5 but for the choice of a more general Sérsic profile for the bulge and an exponential for the disk.

Galaxies modelled		
Type of fit	r band	i band
de Vaucouleurs + exponential	1450	1469
Sérsic + exponential	1528	1532

Table 3.2: Galaxies in the spectroscopic sample that we use to calculate the fraction of light in the two photometric components of galaxies. Of the 1588 galaxies in our sample for which the redshift is known, 1565 are successfully modelled by the code. In the table we report the number of galaxies in the i and r bands for which we have the spectroscopy, the decomposition parameters, a good photometry and the reduced χ^2 of the fitting is greater than 0.35.

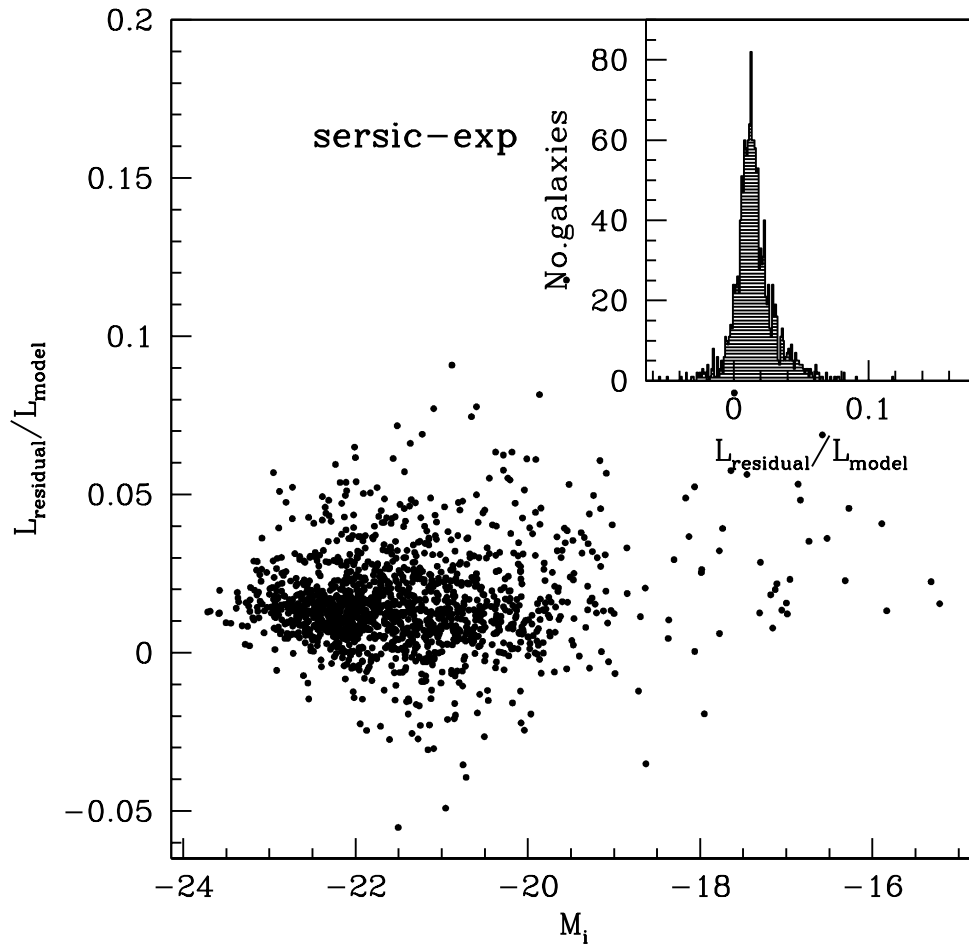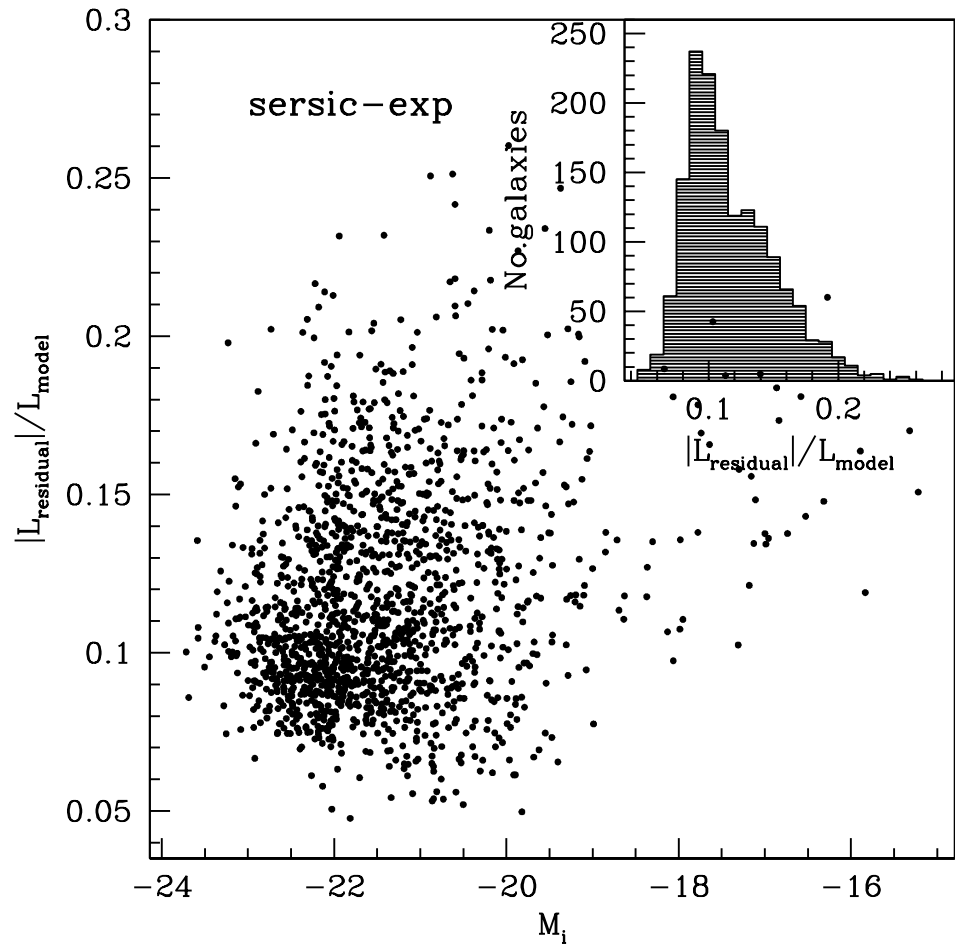| Type of fit	r band	i band
de Vaucouleurs + exponential	$(55.01 \pm 2.11)\%$	$(54.92 \pm 2.02)\%$
Sérsic + exponential	$(51.38 \pm 1.73)\%$	$(55.41 \pm 1.98)\%$

Table 3.3: Total fraction of light in the disk component in the local universe in the r and i band for the two set of parametric functions considered.

value of the residuals peaks at 0.1 with a slightly asymmetric, longer tail towards higher values. The light in the residual images is a tiny fraction of the total one and the points occupy in a uniform way the residual luminosity–absolute magnitude plane with the exception of galaxies fainter then -20 for which G_2 is greater than 0.1. We therefore believe that the galaxy luminosity distribution is reliably modelled and the fit can be regarded as robust.

3.4.2   Disk and Bulge luminosity

In this section we derive the luminosity in bulges and disks in the local universe in the Sloan i and r bands from our complete sample of r selected galaxies with $r < 15.9$ after the extinction correction.

From the total sample of 1862 galaxies we only consider 1588 objects for which spectroscopic data are available and it is therefore possible to measure the absolute magnitudes we need for the luminosity density measurements. The absolute magnitudes used in this paper are k–corrected using the k–correction code by Blanton et al. (2003), $v2\_16$. Since in the SDSS the median redshift is near $z = 0.1$, it is reasonable to express SDSS results in the SDSS filter system shifted by 0.1. Following Blanton et al. (2003b) we perform the k–correction to $z = 0.1$ and we denote the absolute magnitudes we obtain $^{0.1}M_r$ and $^{0.1}M_i$ to distinguish them from the ones in the unshifted system.

The 23 objects for which we do not have morphological classification are not taken into account. So we have 1565 objects with redshift for which the

Figure 3.8: Distribution of the 1469 galaxies with redshift in the *i* band modelled by a de Vaucouleurs plus an exponential with respect to the axial ratio of the disk. Galaxies of all morphological types are divided in bins of absolute magnitude with an equal number of objects.

Figure 3.9: Distribution of the 1469 galaxies with redshift in the *i* band modelled by a de Vaucouleurs plus an exponential with respect to the Hubble morphological T–type. Galaxies of all morphological types are divided in bins of absolute magnitude with an equal number of objects.

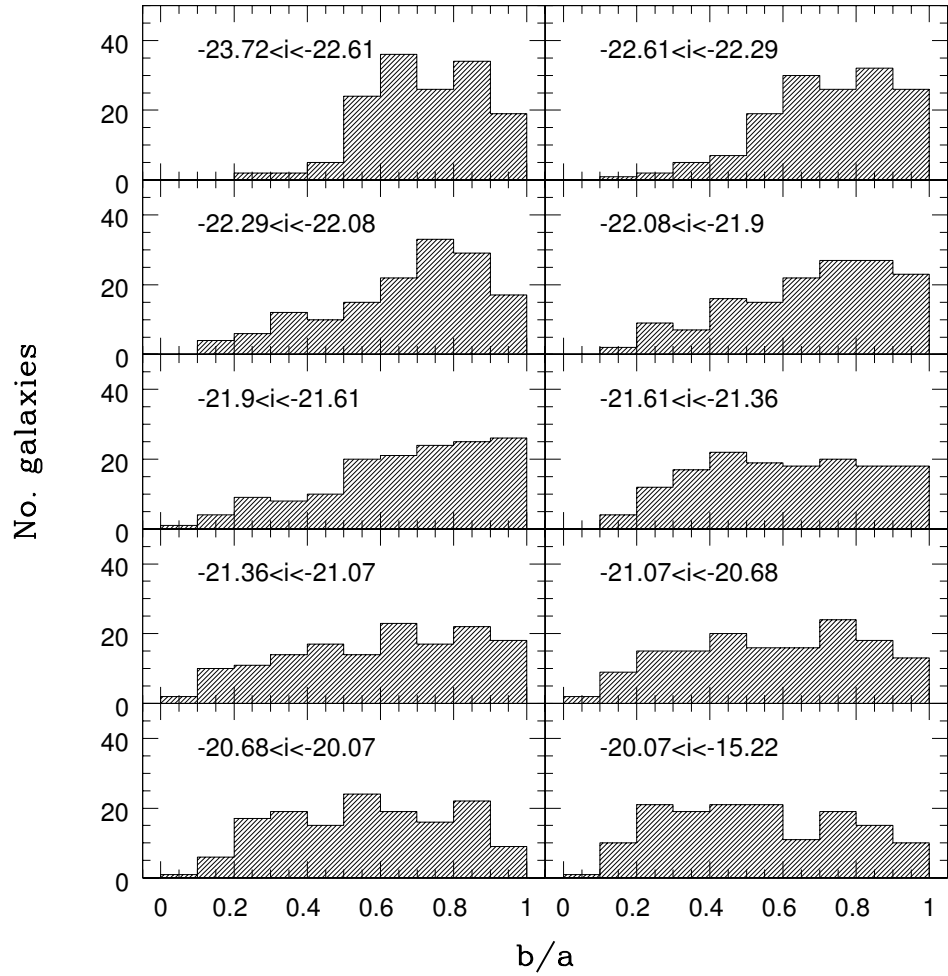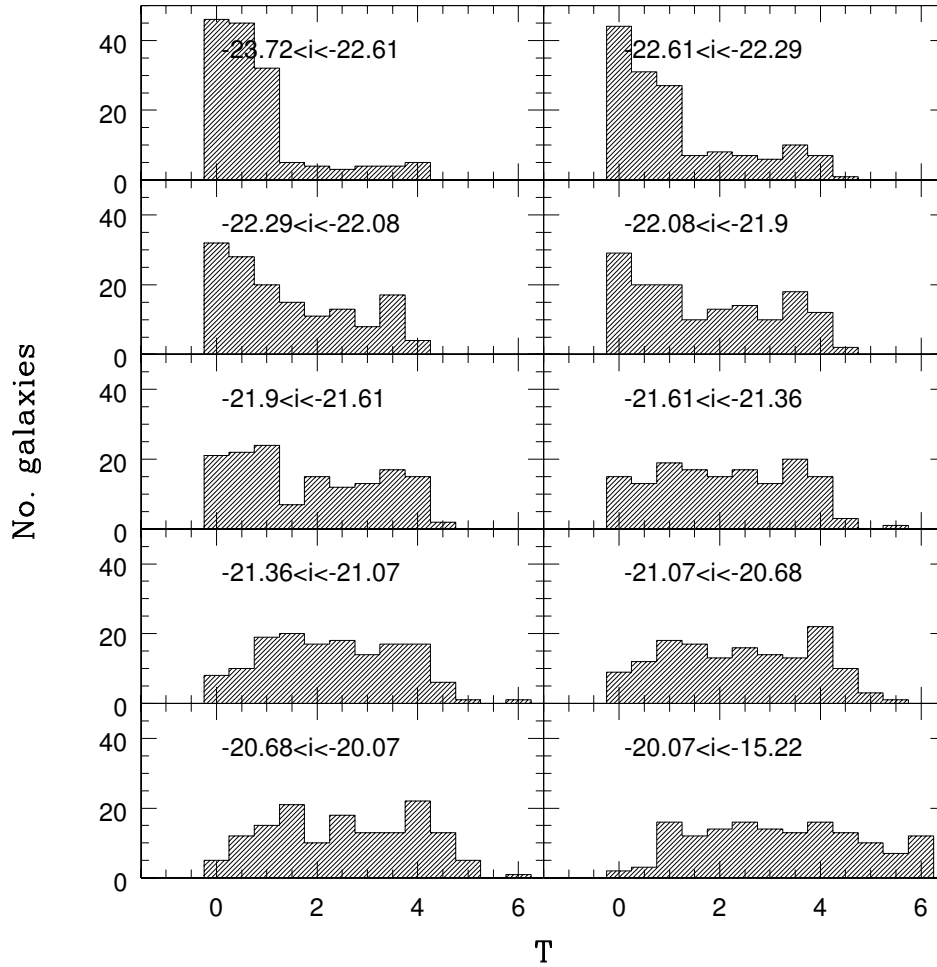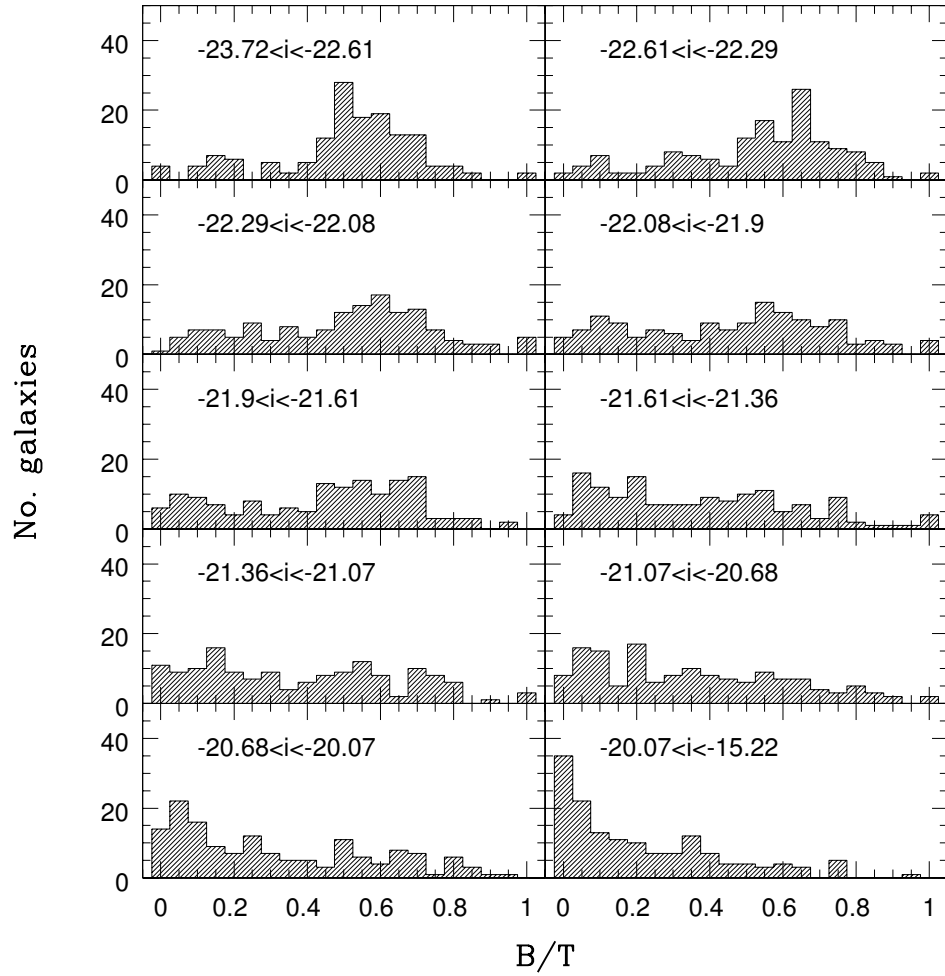Figure 3.10: Distribution of the 1469 galaxies with redshift in the *i* band modelled by a de Vaucouleurs plus an exponential with respect to the bulge–to–disk ratio. Galaxies of all morphological types are divided in bins of absolute magnitude with an equal number of objects.

bulge to disk decomposition is performed. On the spectroscopic sample we perform a further selection which reduces the number of objects we use to estimate the luminosity in bulges and disks to the numbers in Table 3.2. We decide to consider only the galaxies for which the reduced chi–squared given by the decomposition routine is more than 0.35 and in addition we remove three objects in the sample for which the k–correction is not reliable due to bad photometric data in the bluest and reddest bands.

In order to compute the amount of total light which comes from the two different photometric components of galaxies, we analyse the fraction of light in the disk component for 10 luminosity bins in the i and r band containing the same number of objects.

The distribution of the apparent axial ratio of spiral galaxies is expected to be roughly constant since disks are randomly oriented. In Figure 3.8 we show the axial ratio for the disk component alone in our decomposition: while for the faintest galaxies it is indeed flat, in the brightest bins there is a bias towards high b/a, and for the brightest galaxies there are almost none which have $b/a < 0.5$. Since in these bins we have mostly early–types galaxies, according to the visual classification (Figure 3.9), this is showing that few very luminous galaxies actually have real thin disks detectable by the fitting algorithm which is using the two components to improve fits to ellipsoidal galaxies where there are isophote twists or significant variations of ellipticity with radius.

In order to circumvent this problem we use in our analysis only the galaxy in each absolute magnitude bin which have $b/a < 0.5$, which we believe to be real disks, and we assume that the same number of disk systems have $b/a > 0.5$, assuming a uniform distribution.

For each bin k we estimate the fraction of the light in the disk component

$$f_{disk,k} = \frac{L_{disk,k}}{L_{tot,k}} \tag{3.6}$$

where $L_{disk,k}$ is the luminosity of a galaxy in bin k coming from the disk and $L_{tot,k}$ is the total luminosity in that bin. Since we assume that we can rely on our decomposition only for edge–on systems

$$f_{disk,k} = \frac{L_{b/a<0.5,disk,k} + L_{b/a>0.5,disk,k}}{L_{tot,k}} \tag{3.7}$$

where $L_{b/a<0.5,disk,k}$ is the luminosity due to disks in the bin k for edge–on galaxies. The light coming from disks with $b/a > 0.5$ is taken into account. We consider that, due to dust attenuation inside the galaxy as the inclination of a disk galaxy increases, the reduction of its disk light also increases whereas the attenuation of the bulge is little affected. Adopting a standard empirical description for the extinction, A_λ, as a function of the inclination

i in the pass–band λ

$$A_\lambda = \gamma_\lambda \log(a/b), \tag{3.8}$$

as a correction to face–on orientation, and following Tully et al. (1998) we obtain:

$$f_{disk,k} = 2.56 \cdot \frac{L_{b/a<0.5,disk,k}}{L_{tot,k}}. \tag{3.9}$$

The bulge to total ratio B/T is one of the structural parameters which enters our model. We use it to derive the luminosity of the disk component for each single edge–on galaxy in the bin, $L_{b/a<0.5,disk,k,i}$, so that

$$L_{b/a<0.5,disk,k} = \sum_i^{N_{b/a<0.5,k}} L_{b/a<0.5,disk,k,i} =$$

$$\sum_i^{N_{b/a<0.5,k}} \left(1 - BT_{b/a<0.5,k,i}\right) \cdot L_{b/a<0.5,k,i} \tag{3.10}$$

and we obtain this final formula

$$f_{disk,k} = 2.56 \cdot \frac{\sum_i^{N_{b/a<0.5,k}} \left(1 - BT_{b/a<0.5,k,i}\right) \cdot L_{b/a<0.5,k,i}}{L_{tot,k}}. \tag{3.11}$$

In each absolute magnitude bin the disk contribution to luminosity density is given by the total luminosity density in the bin $\Phi_{tot,k}$, according to the Blanton et al. (2003b) luminosity function, multiplied by the fraction of light in disks $f_{disk,k}$.

$$\Phi_{disk,k} = \Phi_{tot,k} \cdot f_{disk,k}. \tag{3.12}$$

The sum over all absolute magnitude bins provides the total disk contribution to the luminosity density and a comparison with the total luminosity density in a specific band–pass gives the final result, the fraction of all light coming from disks in the local universe.

   The behaviour of the fraction of light in the disk component in different magnitude bins is shown in Figure 3.11–3.12 for the galaxies modelled in the i and r band respectively. The last magnitude bin (of the ten we consider) is split into two to better sample the fainter end. There is a clear increase of the fraction of light in the local universe which resides in the disk component when we move towards fainter objects. A decrease of the fraction of pure bulge galaxies, namely galaxy without a detected disk, with decreasing magnitude is clearly visible in Figure 3.13–3.14.

Both our sample and the one used by Blanton et al. (2003b) to derive the luminosity function do not differ significantly, and the two data samples are compatible with being random sampling of the same, unknown distribution. We are therefore confident of the applicability of our results to their luminosity function. The final result we obtain for the total fraction of the light in the disk component in the local universe is of the order of $(51 \div 55 \pm 2)\%$, independent of the bands and on the decomposition. The details are in Table 3.3.

Error analysis

A detailed error estimate is performed on the disk luminosity density we measure. As mentioned above, in each bin the disk luminosity density is given by the product of the total luminosity density times the fraction of the light due to disks (3.12). The error propagation gives the formula:

$$\sqrt{\left(\frac{\partial \Phi_d}{\partial \Phi_{tot}}\right)^2 \cdot \sigma^2_{\Phi_{tot}} + \left(\frac{\partial \Phi_d}{\partial \bar{f}_d}\right)^2 \cdot \sigma^2_{\bar{f}_d}} \qquad (3.13)$$

Here we simply want to summarize the sources of errors which are present in this kind of study even if for different reasons we do not consider some of them in our analysis. The errors in the measured redshift are typically less than $\sim 10^{-4}$ so they are negligible if compared to the others. An important source of uncertainty is given by the galactic extinction correction but since its estimation is beyond the scope of this work we do not introduce it in our error computation.

The sources of errors which enter our analysis are the ones for the fraction of light in disks due to the errors on the bulge fraction (B/T) from our modelling, which of course affect the absolute magnitude of the disk. Since we consider the mean value for the fraction of light in disks in each bin, together with the errors on the measurements we have to take into account the number of objects per bin. We know the mean value, $\bar{x}$, of the disk–to–total ratio, $(1 - BT_i)$, for the galaxies in the bin with $b/a < 0.5$. The standard error of the mean brings to the formula

$$\sigma_{\bar{x}_{disk,k}} = \sqrt{\frac{\sum_{i=1}^{N_{disk,k}}[(1 - BT_i) - \bar{x}]^2}{N_{disk,k} \cdot (N_{disk,k} - 1)}} \qquad (3.14)$$

In each bin galaxies are distinguished according to their inclination. We estimate the probability to observe a galaxy with a value of $b/a < 0.5$ as the ratio between the number of galaxies which are face–on and the total number of objects in the bin, $p = \frac{N_{disk,k}}{N_k}$. We are therefore dealing with a binomial distribution which gives an indication on how representative our
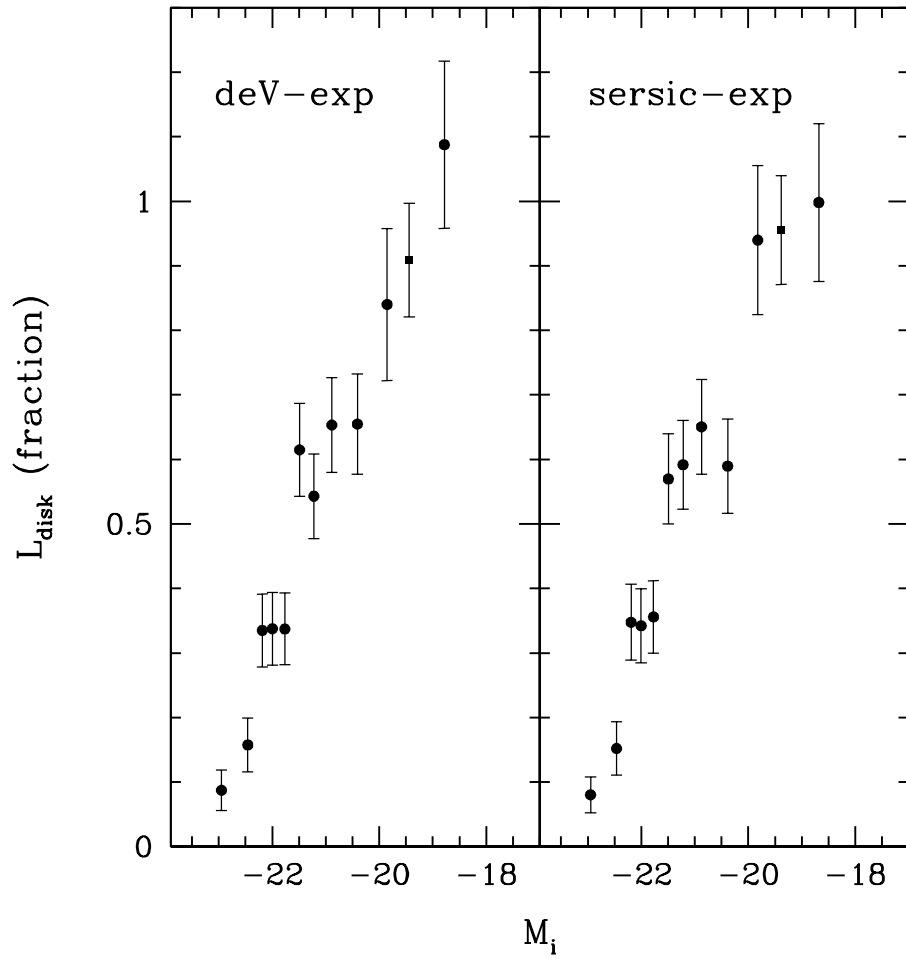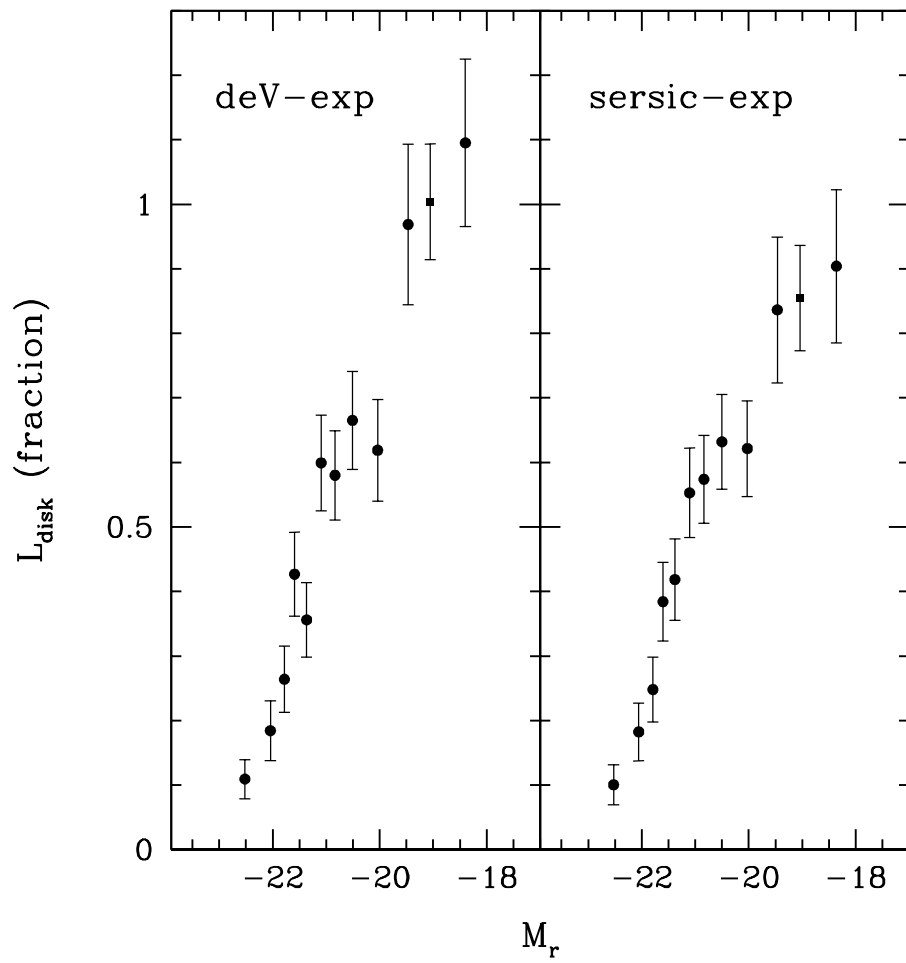
Figure 3.11: Luminosity fraction in disks for galaxies in the Sloan *i* band. The galaxies are modelled with two different sets of parametric functions: de Vaucoulours profile for the bulge and exponential for the disk (left panel) or Sérsic profile for the bulge plus exponential for the disk (right panel)

Figure 3.12: The same as Figure 3.11 but in the *r* band.

sample is. The standard deviation estimates how big the errors are due to the limited size of the sample. The error on the fraction of light in disks in each bin turns out to be

$$\sigma_{f_{disk,k}} = \frac{2.56}{N_k} \sqrt{\bar{x}^2 \cdot N_k \cdot p \cdot (1-p) + N_{disk,k}^2 \cdot \sigma_{\bar{x}}^2} \qquad (3.15)$$

To measure the total fraction of light in the disk component in the local universe we use the formula

$$F_{disk} = \frac{\sum_k f_{disk,k} \cdot L_k}{\sum_k L_k} \qquad (3.16)$$

where L_k is the total luminosity in one bin so that $L_{tot} = \sum_k L_k$ is the total luminosity in the universe and $L_{tot,disk} = \sum_k f_{disk,k} \cdot L_k$ is the total luminosity due to the disk component of galaxies. The error on this quantity is easily obtained from

$$\sigma_{F_{disk}} = \sqrt{\frac{\sum_k \left(\sigma_{f_{disk,k}} \cdot L_{disk,k}\right)^2}{L_{tot}^2}}. \qquad (3.17)$$

3.5 Discussion

The structural parameters of each galaxy in the two bands are in reasonably good agreement, their deviations being due mainly to errors in the decomposition process, possibly enhanced by slightly different sensitivities of the images in the two filters. It is also well known that the effect of dust attenuation is smaller in the reddest band so that images in the NIR better represent the true stellar distribution. It is then expected that the structural parameters we obtain in the i and r bands are slightly different. Nevertheless this difference cannot be too large since both bands are longwards the 4000–Å break, sampling the same stellar population.

3.5.1 Comparison between different fits

We already mentioned that the model we use has a total of 12 parameters. It is possible either to freeze some of them to a chosen value, for specific kind of study, or to let them free to assume all the possible values inside a range considered reasonable to be explored by the fitting algorithm.

Since our sample includes galaxies of different morphological types and consequently with a wide range of global and structural parameters of which
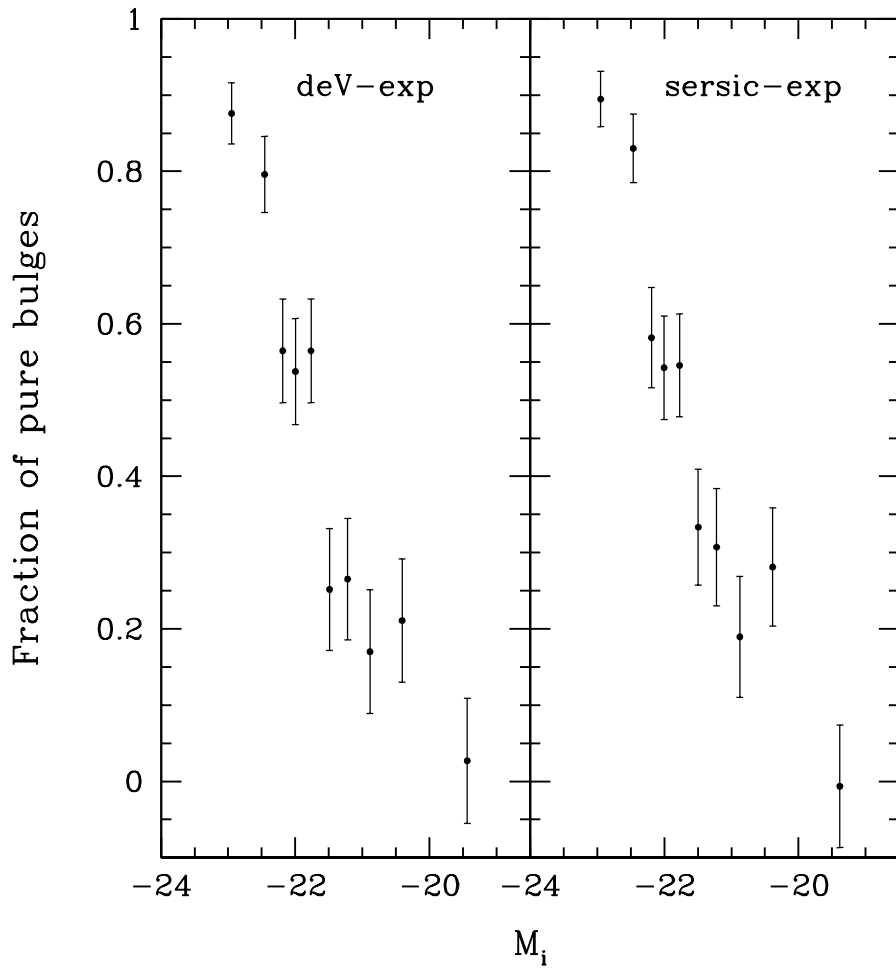
Figure 3.13: Fraction of pure bulge galaxies as a function of the absolute magnitude. Different parametric functions are considered: de Vaucouleurs plus exponential (left–panel) and Sérsic plus exponential (right–panel).
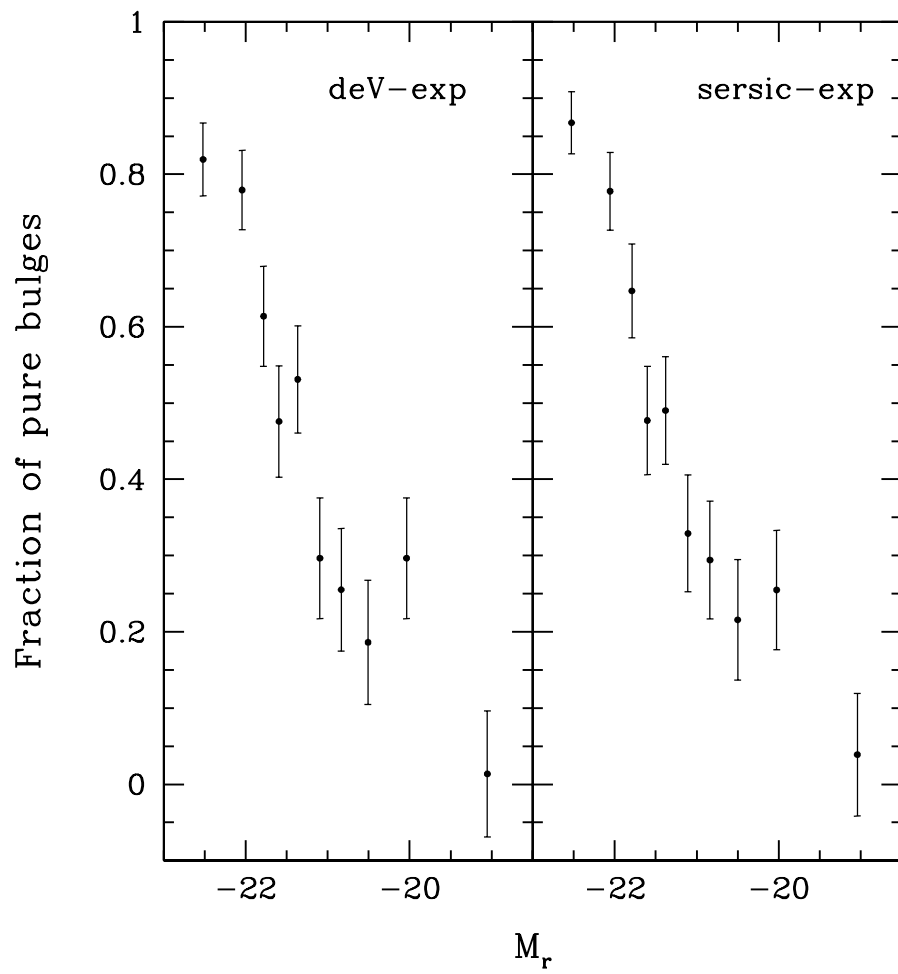
Figure 3.14: As Figure 3.13 but in the *r* band.
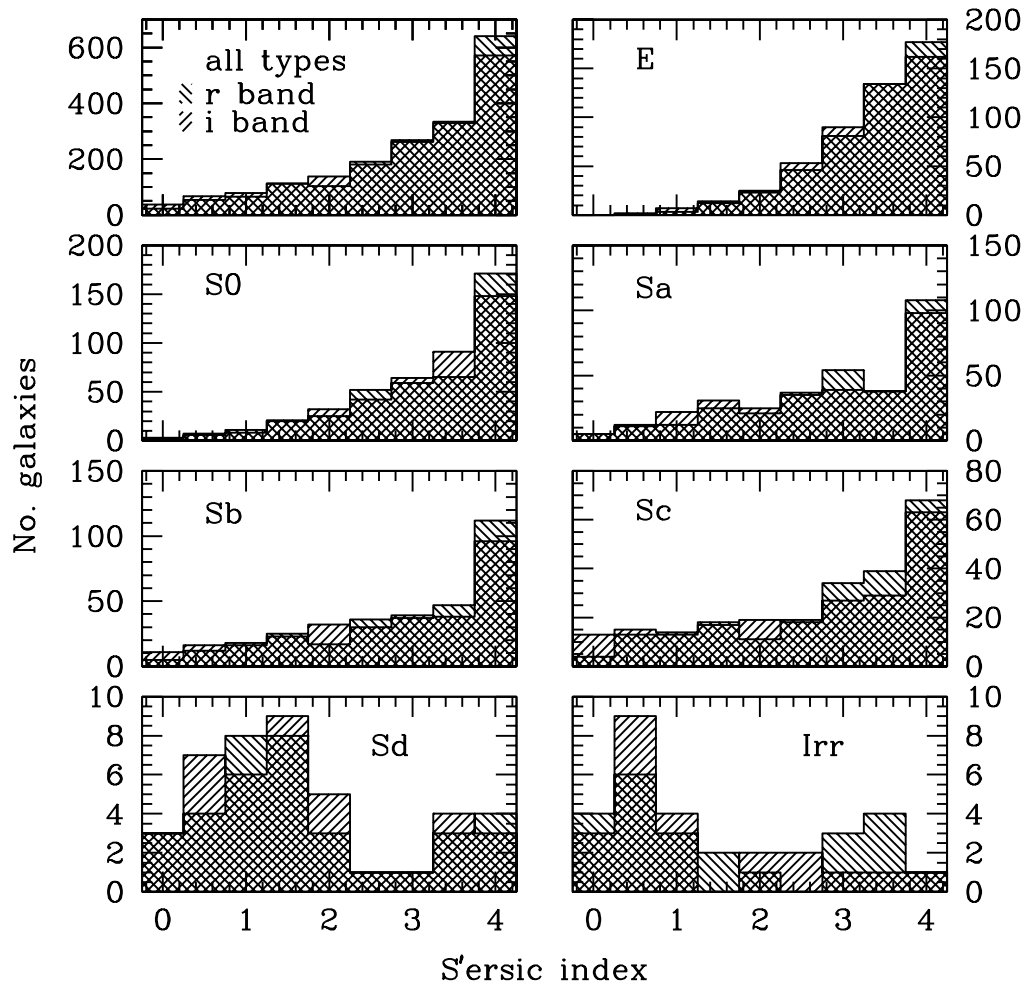
Figure 3.15: Distribution of the Sérsic index n. The upper–left panel shows the distribution for the total sample of 1790 and 1782 galaxies successfully modelled in the i and r band respectively. In the other panels the Sérsic index distribution is shown for the different morphological types.

we do not have an *a priori* knowledge, it is reasonable to set very relaxed lower and upper limits for each parameter we plan to explore.

Nevertheless in one set of our modelling we did the specific choice to fix the Sérsic index to the value of 4 in order to use the de Vaucouleurs profile to model the inner light component of the galaxies, since it is known from previous studies (Andredakis 1998; Courteau, de Jong & Broeils 1996; de Jong 1996b) that for galaxies at low redshift this analytic formula well describes the light distribution of many ellipticals while later–type galaxies are well described by a de Vaucouleurs bulge plus an exponential disk. In Table 3.2 it is shown that the number of galaxies successfully modelled decreases once we reduce the degrees of freedom. When the Sérsic index is let free to assume all the possible values between 0.2 and 4 we obtain the distribution shown in Figure 3.15. In the upper–left panel the Sérsic index distribution is shown for all the 1790 galaxies in the i band and the 1782 galaxies in the r band, out of the the total sample of 1862, which are modelled. There is a peak corresponding to the $r^{1/4}$ law. We confirm that this specific parametric function can be considered as a standard one for galaxy decomposition. From the other panels of Figure 3.15 it is evident that early–type galaxies are described as well with values of n smaller than 4, the same is true for the bulge of early–type spirals. For later–type spirals there is a clear peak for lower values of n close to 1, a double–exponential profiles is therefore a good description of the brightness distribution for these objects.

3.5.2   Comparison between different bands

In performing the galaxy modelling in the two different Sloan filters no fitting parameter is constrained to have the same value in both band-passes. This means that the thumbnail images in the i and r bands are fitted independently.

In Figure 3.16 and 3.17 the retrieved parameters in the Sloan i and r bands are plotted against each others for the 1636 galaxies modelled in both bands by fitting a de Vaucouleurs profile to the bulge and an exponential to the disk. The same is shown in Figure 3.18 and 3.19 for the 1766 galaxies modelled in both bands by fitting a Sérsic profile to the bulge and an exponential to the disk.

In the apparent magnitude plot there are only few isolated points while the others correlate well, the shift being due to the different zero points and the scatter in the color. The particular "arrow shape" of the bulge–to–total light ratio can be easily explained since galaxies which result in pure bulge objects in one band can actually present a faint disk that can be detected in the other band, resulting in a smaller value for the bulge–to–disk ratio. There is a quite good agreement between the values of the scalelengths for the bulge and the disk component of galaxies measured in different filters,

we interpret this result as a sign of the absence of color gradients in the structural subcomponents. Since a correlation is seen for the majority of the quantities,we conclude that the fit can be regarded as robust.
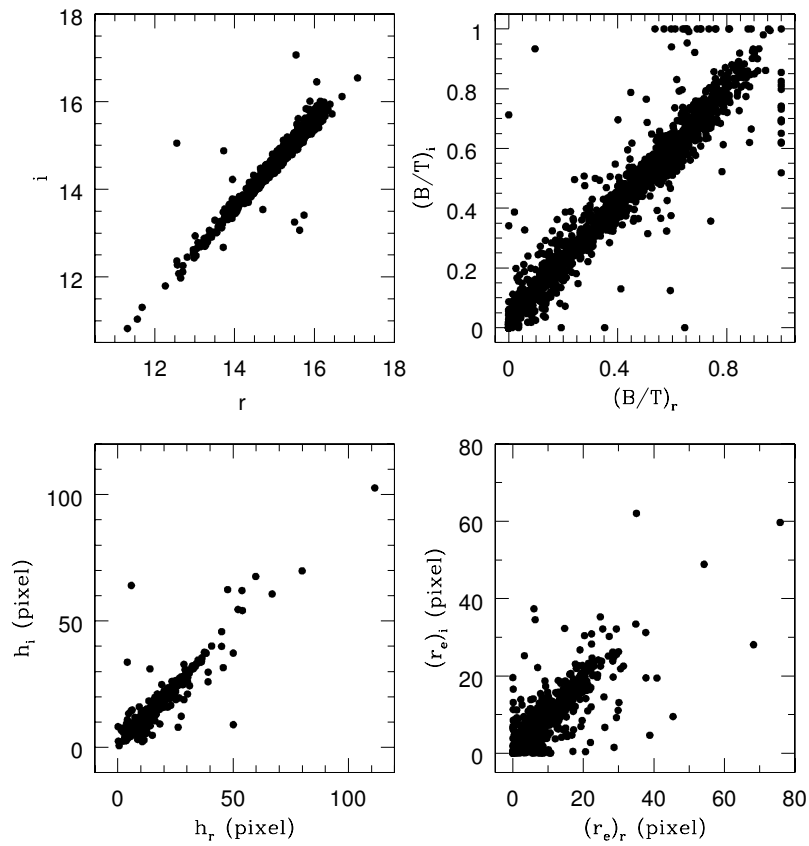
Figure 3.16: The total flux (upper–left), the bulge fraction (upper–right), the disk scalelength (lower–left) and the effective radius of the bulge (lower–right) in the i and r bands are plotted against each other for the 1636 galaxies modelled in both bands by fitting a de Vaucouleurs profile to the bulge and an exponential to the disk.
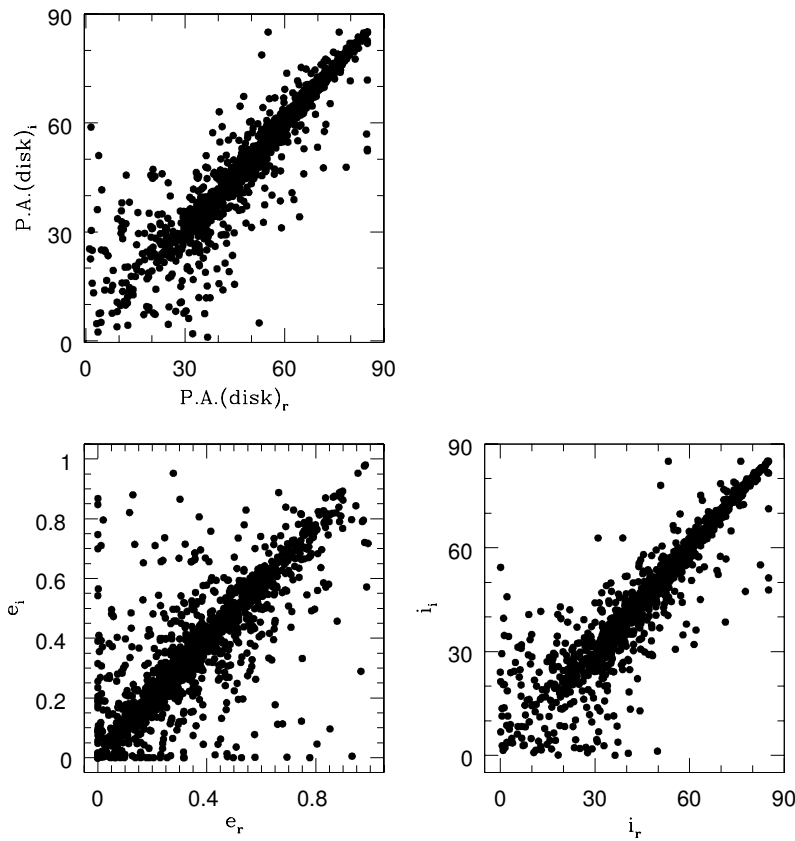
Figure 3.17: The position angle of the disk (upper–left), the ellipticity of the bulge (lower–left) and the inclination angle of the disk (lower–right) in the i and r bands are plotted against each other for the 1636 galaxies modelled in both bands by fitting a de Vaucouleurs profile to the bulge and an exponential to the disk.
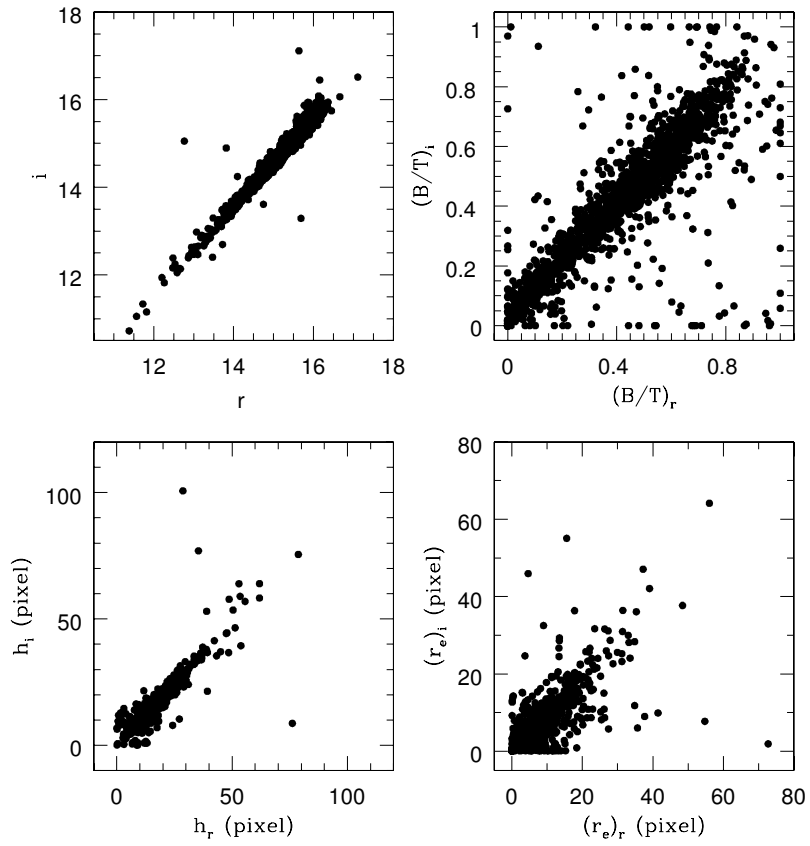
Figure 3.18: The same as Figure 3.16 but for the 1766 galaxies modelled in both bands by fitting a Sérsic profile to the bulge and an exponential to the disk.
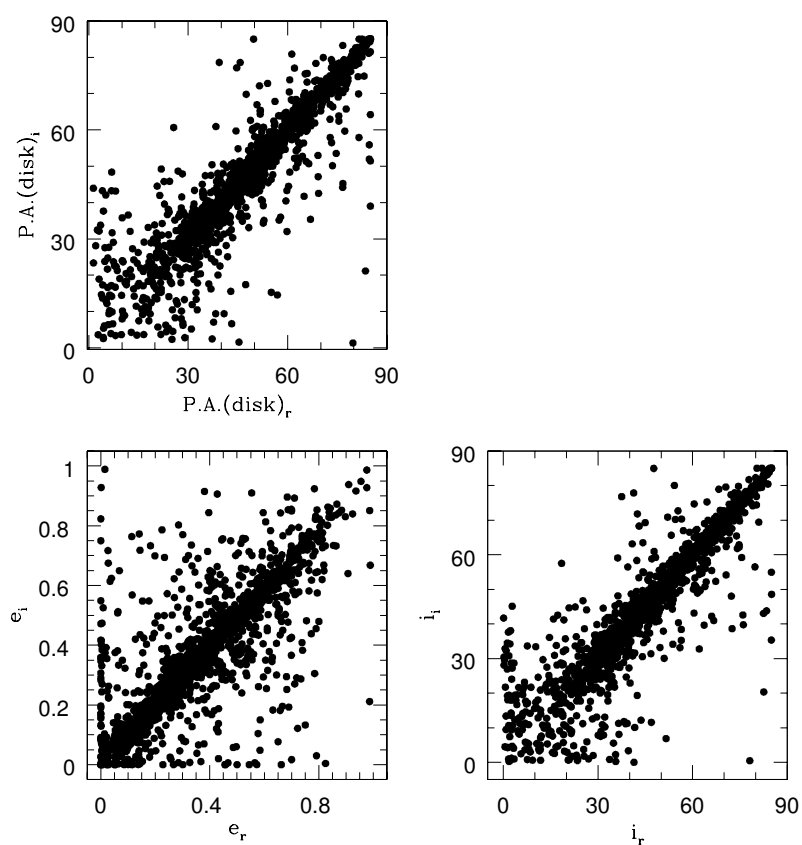
Figure 3.19: The same as Figure 3.17 but for the 1766 galaxies modelled in both bands by fitting a Sérsic profile to the bulge and an exponential to the disk.

Chapter 4

Morphological Classifiers

In this chapter we study the relations between quantitative morphological classifiers using our complete magnitude limited sample of 1862 galaxies drawn from the Sloan Digital Sky Survey. The sample includes bright objects, $r \leqslant 15.9$, in the nearby universe, $z \leqslant 0.12$. It contains ellipticals, lenticulars, early and late–type spirals and irregulars. We consider structural parameters, non-parametric and model–dependent ones, and photometric parameters which are suitable for quantitative, automatic and objective galaxy classification. We first calibrate these parameters using the Hubble type, since "eye–ball" classification is provided for all the galaxies in the sample. We find that rest–frame galaxy colours, concentration index, bulge–to–disk ratio, effective surface brightness, mass–to–light ratio, residual and asymmetry parameters define a multi–parameter space in which galaxies of all morphological types are located according to well defined physical properties. We conclude that the quantitative morphological classifiers we select allow us to build galaxy samples according to their stellar masses, mean stellar ages and gas–phase metallicities.

4.1 Introduction

Due to great improvement in observational techniques, digital sky surveys are nowadays performed routinely in various wavelengths, covering the entire electromagnetic spectrum, over extended areas on the sky. Photometric surveys are often supported by spectroscopic follow–up. Automatic pipelines process the data and spectro–photometric information is therefore available for an unprecedented number of objects. Age–old problems can be studied with the advantage of good statistics while new interesting research fields can be investigated, especially thanks to the advent of multi–object spectroscopy.

In galaxy formation and evolution studies it is often required to deal with morphologically classified galaxy samples. The cosmic evolution of

galaxy morphology (Lilly et al. 1998; Marleau & Simard 1998), the study of the Fundamental Plane of spheroids (Djorgovski & Davis 1987) and of the Tully–Fisher relation of spiral galaxies (Tully & Fisher 1977) and the investigation of the morphological segregation of galaxies (Dressler 1980) are only a few examples of studies for which samples with precise morphological properties are needed.

The morphological classification of galaxies aims to divide galaxies into types according to their shape. The appearance of galaxies is strongly dependent on projection effects: the disk of a galaxy is easily visible in edge–on systems while it could be undetectable for face–on systems if a spiral structure is not present or the resolution is not high enough. Galaxy morphology also depends on the effect of dust extinction, which is smaller in the near–IR, and on the observing wavelength. The photometric band in which we observe becomes important when observing galaxies at different redshifts. The outcome of the classification will depend on the rest–frame wavelength sampled. Morphological k–correction can be quite significant and it plays an important role when we want to disentangle evolutionary effects from simple bandpass shifting.

Despite its subjective nature, visual classification has a long tradition. The most used galaxy classification scheme was introduced by Hubble (1939) and later on, after many modifications, brought to completion by Sandage (1961). Galaxies are placed in the Hubble scheme according to three main visual properties: the predominance of their bulge component; the degree to which spiral arms are resolved into stars and HII regions; and the tightness with which spiral arms are wound. When dealing with large datasets, such as the ones provided by large surveys, it is necessary to find quantitative measures which correlate with the Hubble scheme in order to perform automated, reproducible and objective classifications. Many attempts have been made and classifications using colours, spectroscopic features or purely photometric ones have been proposed. Strateva et al. (2001) show that galaxies have a bimodal $u - r$ colour distribution, corresponding to early and late morphological types, which can be clearly separated by a $u - r = 2.22$ colour cut. Spectroscopic features such as the 4000–Å break strength ($D_n 4000$) and the Balmer absorption line $H\delta$ have shown to be powerful probe of the recent star formation history of a galaxy (Kauffmann et al. 2003). In particular a value of $D_n 4000 = 1.8$ can be used to separate galaxies dominated by an old stellar population from galaxies with more recent star formation. A classification scheme which combines spectral and structural parameters was introduced by Whitmore (1984) and revised by Bershady et al. (2000). Their multivariate photometric space can be used to reliably classify galaxies at different redshifts in a fully quantitative way.

It is worth mentioning that, although purely based on appearance, the so called "Hubble tuning fork" correlates well with physical galaxy characteristics such as: stellar masses, baryonic specific angular momentum, stellar

ages, mean disk surface brightness, stellar densities and cold gas content. Galaxy morphology is intrinsically related to the formation and the subsequent evolution of the galaxy. It is indeed the result of physical processes such as star formation and interactions and mergers with other galaxies (Conselice et al. 2003).

In this work we attempt to expand the study of Bershady et al. (2000) by adding multi–colour data with high resolution spectroscopy and higher order statistics. We also introduce parametric measures derived from the decomposition of the surface brightness profile of a galaxy into a bulge and a disk.

We therefore present an overview of quantitative morphological classifiers. Among them we choose the ones whose combination better allows to select a sample of morphologically classified galaxies with only a small contamination from other galaxy types. The final goal is to actually deal with samples of galaxies with well defined physical properties. Therefore we turn our attention to mean stellar ages, gas–phase metallicities and stellar masses and we look at how they distribute on the multi–parameter space we investigate.

This chapter is organized as follows. In section 4.2 we present the sample used. Section 4.3 briefly describes the photometric and spectroscopic data we use and the fitting algorithm adopted to fit the galaxy light distributions. The quantitative morphological classifiers we investigate are reviewed in section 4.4. In section 4.5 we report on the possibility to select clean samples on the basis of physical properties. We end in section 4.6 with some discussion and a listing of our conclusions.

The Hubble constant is quoted as $H_0 = 100h$ km s^{-1} Mpc^{-1}. We assume throughout this chapter, unless otherwise stated, $h = 0.7$, $\Omega_M = 0.3$ and $\Omega_\Lambda = 0.7$.

4.2   Sample of galaxies

A detailed description of the sample of galaxies analysed in this chapter can be found in 3. We now review only the information that is relevant for the study presented here.

We use an homogeneous sample of 1862 galaxies drawn from the Sloan Digital Sky Survey (SDSS; (York et al. 2000; Stoughton et al. 2002)) for which a morphological eye classification, using the g band image of each galaxy according to the *Hubble Atlas of Galaxies* (Sandage 1961), is performed (Nakamura et al. 2003). The sample is limited to galaxies with $r \leqslant$ 15.9 mag after correction for foreground galactic extinction using the reddening maps of Schlegel, Finkbeiner, & Davis (1998). As a result the sample contains mostly luminous and physically large galaxies. Photometric data are provided in u, g, r, i, and z bands and spectroscopic follow–up was car-

Galaxies modelled						
Band	de Vaucouleurs+exp			Sérsic+exp		
	Photo	Spectra	$b/a < 0.5$	Photo	Spectra	$b/a < 0.5$
u	1449	1245	488	1489	1281	527
g	1630	1403	470	1746	1505	501
r	1689	1451	493	1782	1530	506
i	1715	1471	494	1790	1534	492
z	1726	1483	530	1788	1536	518

Table 4.1: Number of galaxies in the u, g, r, i and z bands for which the bulge–to–disk decomposition is performed fitting a de Vaucouleurs plus exponential and a Sérsic plus exponential models to the bulge and the disk components of the galaxies. The "Photo" columns refer to galaxies in the photometric sample; the "Spectra" columns refer to galaxies with redshift; the "$b/a < 0.5$" columns are for the galaxies with redshift, successfully modelled by the algorithm, for which the axial ratio is less then 0.5 (edge–on galaxies).

ried out for 1588 galaxies in the sample. More details concerning the SDSS photometric system may be found in Fukugita et al. (1996) and Smith et al. (2002). Information related to the photometric monitoring system and the SDSS camera can be found in Gunn et al.(1998) and Hogg et al.(2001). Details of the spectroscopic target selection of galaxies are given in Strauss et al. (2002).

Our sample contains galaxies of all morphological types although Table 3.1 shows that it is biased towards early–type objects with late–type galaxies, in particular irregulars, being under–represented. This is a common problem in magnitude limited samples since low surface brightness objects tend to drop out of the sample.

4.3   The data and the reduction

In this section we provide a brief review of the observed and derived parameters of galaxies studied in this chapter.

The photometric data are taken from the SDSS data base. They are obtained from an automatic pipeline called PHOTO (Lupton et al. 2001). All magnitudes quoted in this work are Petrosian magnitudes since PHOTO uses a modified form of the Petrosian (1976) photometric system, which is designed to measure a constant fraction of the total light independent of the surface brightness limit. The Petrosian flux is defined as

$$F_P = 2\pi \int_0^{2r_P} I(r)\,dr \qquad (4.1)$$

where $I(r)$ is the azimuthally averaged surface brightness profile, and r_P is the Petrosian radius. r_P is defined to be the radius where the local surface brightness averaged in an annulus equals 20 per cent of the mean surface brightness interior to this annulus

$$0.2 = \frac{2\pi \int_{0.8r_P}^{1.25r_P} \frac{I(r)rdr}{\pi r^2(1.25^2 - 0.8^2)}}{2\pi \int_0^{r_P} \frac{I(r)rdr}{\pi r^2}}. \tag{4.2}$$

We k-correct the magnitudes of our sample to $z = 0.1$ using the k–correction code by Blanton et al. (2003), $v2\_16$. From the PHOTO output we also consider the radii enclosing 50 and 90 per cent of the Petrosian flux, R_{50} and R_{90}. The redshifts for our spectroscopic sample are obtained with the spectroscopic pipelines IDLSPEC2D and SPECTRO1D. The errors on the measured redshifts are typically less than 10^{-4}.

Using **Gim2D** (Simard et al. 2002), a two–dimensional surface brightness decomposition routine, we fit two sets of parametric functions to the bulge and disk components of all the galaxies in our photometric sample. The more general Sérsic $r^{1/n}$ profile (Sersic 1968) and the de Vaucouleurs $r^{1/4}$ law (de Vaucouleurs 1948) are used to model the light in the bulge component while we assume that the light in the disk component has an exponential distribution. More details about the bulge–to–disk decomposition performed for this sample of objects can be found in section 3.3. The de Vaucouleurs profile has been successful in characterising the light distribution of many ellipticals and bulges. This success is in part due to the limits of previous observations. The higher spatial resolution and the better photometry achieved in the last decades have allowed to perform detailed photometric studies and to reveal that the Sérsic model is more appropriate to describe the brightness distribution of bulges of disk galaxies. A total of 12 structural parameters and 6 asymmetric and residual indices are obtained as a result of our decomposition. Here we concentrate our attention on the ones which turn out to be of a certain interest in order to provide a quantitative and repeatable morphological classification.

In Table 4.1 we report the number of galaxies in the u, g, r, i and z band for which we successfully derived structural parameters from the fitting algorithm. The photometry in the u band is low quality and it strongly determines the decomposition success–rate in this band, which is lower with respect to the others. In the same photometric band the number of galaxies well fitted by a Sérsic law is higher than the number of galaxies fitted with a de Vaucouleurs profile. This is expected since there is an additional degree of freedom, the Sérsic index. The "$b/a < 0.5$" column is considered for coherence with what is claimed in section 3.4.2 and refers to the galaxies for which the disk axial ratio is smaller than 0.5 (edge–on systems).

Stellar masses, gas–phase metallicities and r band magnitude–weighted

mean stellar ages are included in our study. These quantities are all measured using big samples of galaxies drawn from the SDSS with spectroscopic information and the latest stellar evolutionary synthesis model (Bruzual & Charlot 2003).

Stellar masses are taken from Kauffmann et al. (2003). They are derived using a method which relies on spectral indicators of stellar ages and fraction of stars formed in recent bursts. In particular this method makes use of two stellar absorption features, the 4000–Å break strength and the Balmer absorption line index Hδ. The $D_n(4000)$ index is small for star–forming galaxies with young stellar population and increases for old, metal–rich galaxies. Strong Hδ absorption lines are present in early–type galaxies and are related to bursts of star formation that ended $\sim 0.1 - 1$ Gyr ago. Gas–phase oxygen metallicities are measured by Tremonti et al. (2004) for ~ 53000 star–forming galaxies at $z \sim 1$. The r band luminosity–weighted mean stellar ages, $< age >_r$, are obtained from Gallazzi et al. (2004). The error on this measurement is quite large due to the strong dependence of the 4000–Å break on metallicity at ages of more than 1–2 Gyr.

4.4   Morphological classifiers

Quantitative morphological classifiers connected to galactic structure but also with a clear physical meaning are a must since large samples of galaxies spanning a wide redshift range are becoming available. On one side orientation effects and the difficulty to identify faint structures can lead to a wrong classification, on the other side many galaxies do not fall into any Hubble class due to a real peculiar shape.

We briefly mentioned in the introduction the attempts already performed in order to define a quantitative multi–parameter space for the classification of nearby and distant galaxies. In comparison to previous studies we have the advantage of dealing with

- a sample of 1862 galaxies, therefore better statistics;

- photometric data in 5 bands, from ultraviolet to near–IR, obtained under the same observing conditions. They form an homogeneous sample;

- spectroscopic information for 1588 objects;

- additional morphological parameters linked to the galaxy structure, derived from the bulge–to–disk decomposition;

- stellar masses, gas–phase metallicities and mean stellar ages.

The parameters derived from the image structure are the bulge–to–disk ratio (B/T), the Sérsic index (n) and two residual parameters (S and G2), all

obtained from the galaxy fit, and the concentration index (c). We consider various rest–frame galaxy colours as the only pure photometric parameters. In the final classification we introduce the average rest–frame surface brightness within the effective radius, μ, and the mass–to–light ratio defined as the total stellar mass of a galaxy divided by its observed luminosity.

We show in this section how different morphological classifiers behave as a function of the qualitative Hubble type. We notice that for some of them the trend with respect to the Hubble type change according to the observing photometric band. This is the preliminary step before finally presenting in section 4.5 the correlations between the best classifiers we locate.

Throughout this chapter the completeness of a given parameter x is defined so that in the completeness plots the solid line represents the completeness of late–type galaxies when for a given value x_1 of the parameter x we select a sample with $x < x_1$, while the dotted line is the completeness of early–type galaxy sample with $x \geqslant x_1$. The contamination from the opposite galaxy type is also shown. In the contamination plots the solid line is the contamination from early–type galaxies to the late–type galaxy sample with $x < x_1$, while the dashed curve is the contamination from late–type galaxies to the early–type sample with $x \geqslant x_1$.

4.4.1 Visual classification

Since the introduction of the Hubble classification scheme, astronomers have been looking at ways to classify galaxies. The main shortcoming is the subjectivity of the procedure. When comparing the visual morphological classification performed by independent observers, Naim et al. (1995) found that even if the agreement between them is acceptable the rms scatter among classifiers is pretty high, ~ 1.8. The dispersion tends to decrease with increasing angular diameter and, in some cases, with increasing axial ratio.

All the galaxies in our sample are visually classified independently by four astronomers (Nakamura et al. 2003) and the median of their classification is taken as final value for the T-type parameter. In the adopted nomenclature T=0 corresponds to ellipticals (E), T=1 are lenticulars (S0), T=2 are Sa, T=3 are Sb, T=4 are Sc, T=5 are Sd and T=6 irregular galaxies. When no classification is assigned T= -1. The "by–eye" classification performed on the galaxies in our sample tends to classify some lenticulars as ellipticals, and spiral galaxies into somewhat later types (Shimasaku et al. 2001). The classifications agree within $\Delta T \leqslant 1.5$.

4.4.2 colour indices

The colours of galaxies correlate with morphology since they reflect their dominant stellar population and they are related to galactic star formation history. Various studies have already been performed to investigate the

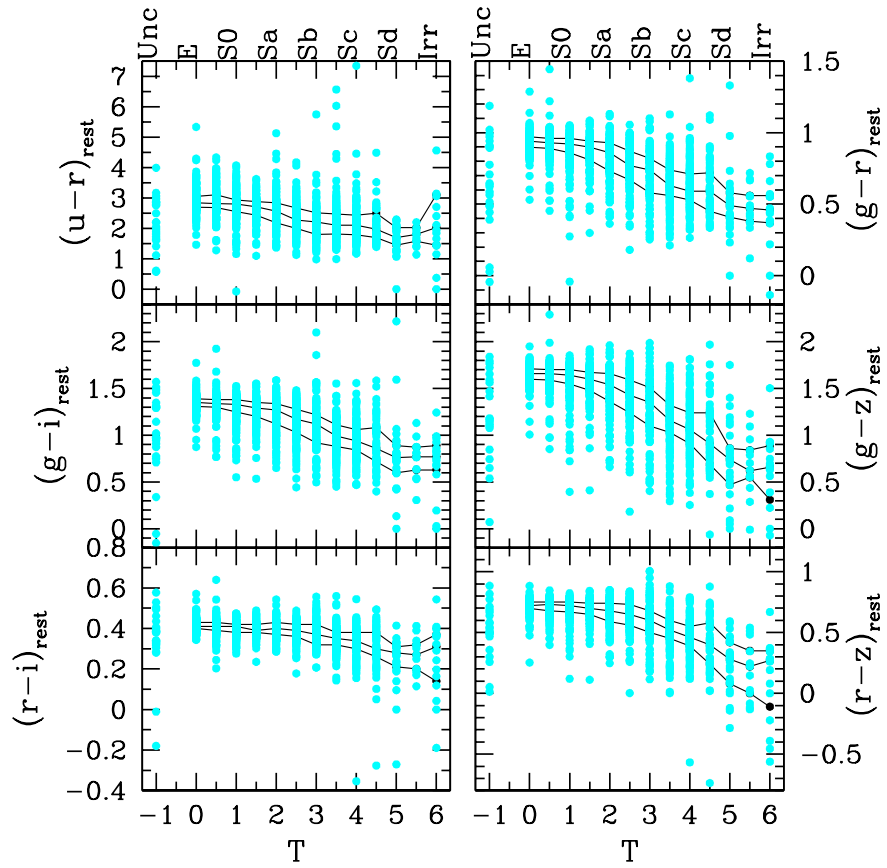Figure 4.1: Distribution of colours of galaxies plotted against the Hubble type for all the galaxies in our photometric sample. The solid lines show the median, the upper and the lower quartiles of the distribution.
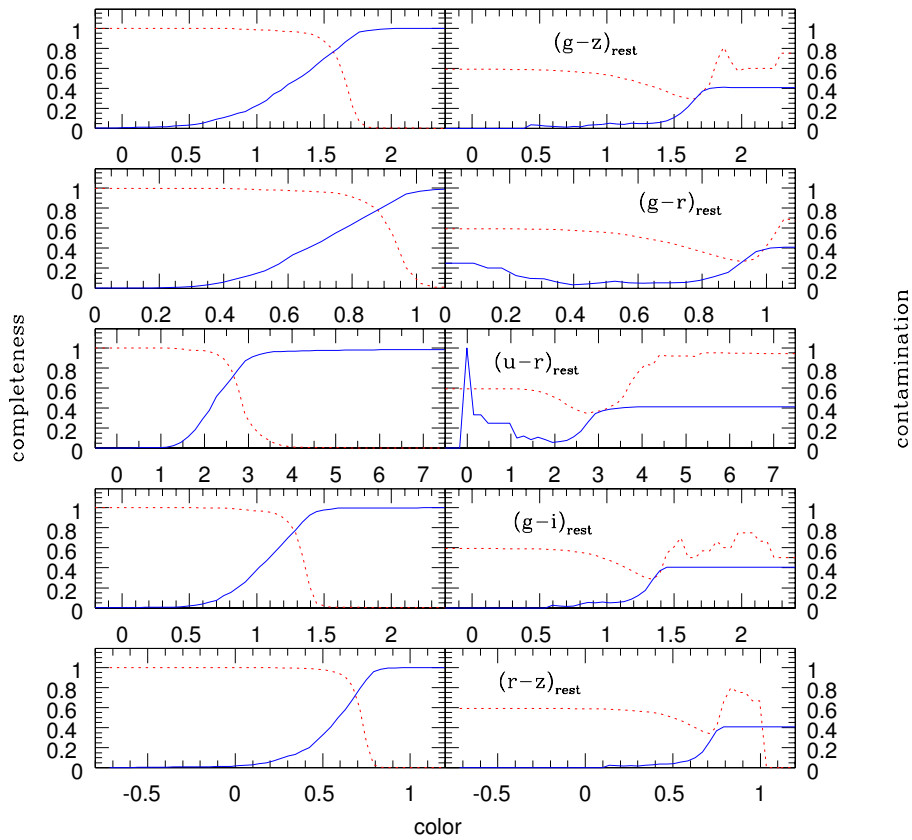
Figure 4.2: Completeness and contamination of early ($T < 1.5$) and late–type ($T \geqslant 1.5$) galaxies as a function of colours. The solid and dotted lines are for late and early–type galaxies respectively.

relations between colours, morphological types, intrinsic luminosities and inclinations. Strateva et al. (2001) use SDSS galaxies to claim that a colour separator $u - r = 2.22$ distinguishes early (E,S0 and Sa) and late–type galaxies while a detailed study of the photometric properties of a small sample of SDSS galaxies is performed by Shimasaku et al. (2001). The distribution of six rest–frame colours, including $u - r$, against the Hubble type for all the galaxies in our spectroscopic sample is shown in Figure 4.1. The median, upper and lower quartiles of the distribution are represented by the solid lines. We observe lower dispersion and redder colours for early–types and higher dispersion and bluer colours when moving towards later–types. The trend is expected. We try to choose among the different colours the one which better allows us to select early ($T < 1.5$) and late–type ($T \geqslant 1.5$) objects. We observe (see Figure 4.2) that it is possible to build samples with a completeness of $\approx 80\%$ and a contamination of $\approx 15 - 35\%$ independently of the choice of the colour. The best behaviour being perhaps the one of $g - r$ due to the lower contamination. We conclude that galaxies can be divided into blue and red subsamples, as expected since different morphological types are dominated by different stellar populations.

4.4.3 Concentration index

Morgan (1958,1959) was the first to consider the central light concentration as a primary classification parameter. In the Hubble sequence galaxies are placed according to the predominance of their bulge component and therefore a correlation between Hubble type and concentration is expected. The light profile of early–type galaxies is more centrally concentrated. The advantage in using the concentration instead of the Hubble type is that the former is a quantitative parameter.

In many studies (Doi, Fukugita, & Okamura 1993; Abraham et al. 1994; Bershady, Jangren, & Conselice 2000) the concentration index is defined using multi–aperture isophotal photometry and therefore it depends on the galaxy's distance and apparent surface brightness. The definition of the concentration index as the ratio between the radii that enclose 75% and 25% of the total light (de Vaucouleurs 1977) is adopted by Scodeggio et al. (2002), who point out the need for good image resolution when measuring this parameter. In order to be consistent with previous Sloan studies (Blanton et al. 2001; Shimasaku et al. 2001; Strateva et al. 2001) we define the concentration index as $c = R_{90}/R_{50}$. Due to the definition of Petrosian quantities, our concentration parameter is distance and apparent brightness independent. All authors show that the concentration parameter correlates well with the "by–eye" classification into Hubble types, although early–type samples result to be contaminated by Sa galaxies (Shimasaku et al. 2001).

The distribution of the concentration index in the g, r, i and z bands for all the galaxies in our photometric sample is shown in Figure 4.3. We
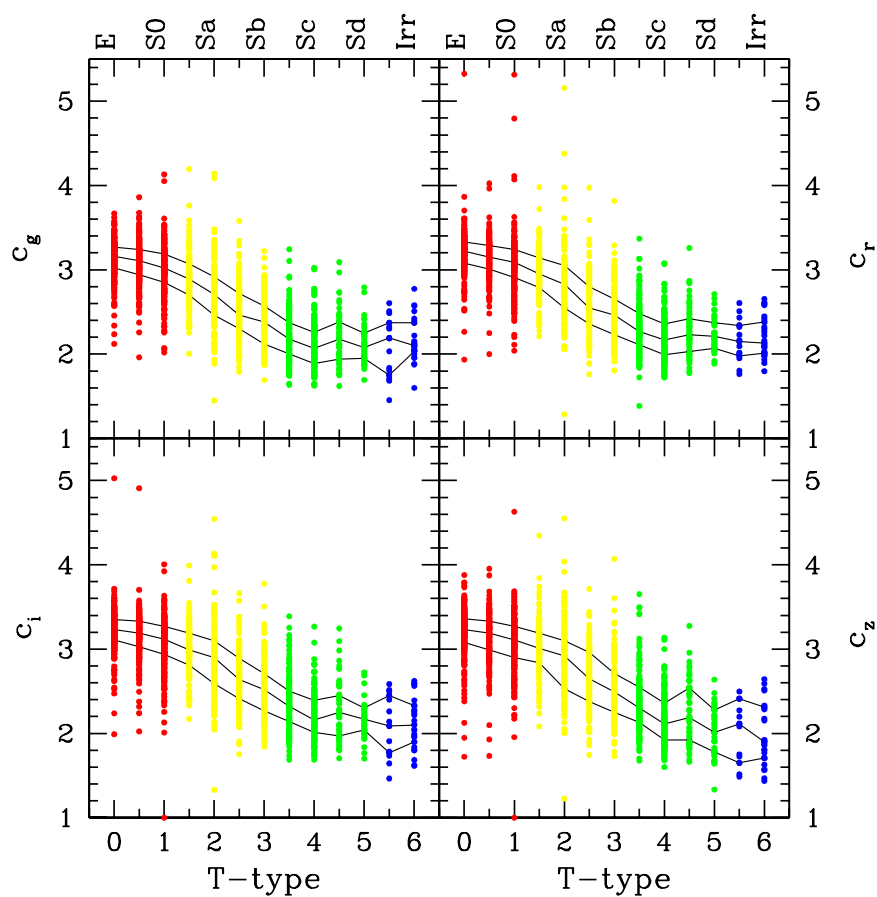
Figure 4.3: Distribution of the concentration index (c=R90/R50) as a function of the Hubble type in the g, r, i and z bands. All the galaxies in the photometric sample are plotted. The solid lines show the median, the upper and the lower quartiles of the distribution.
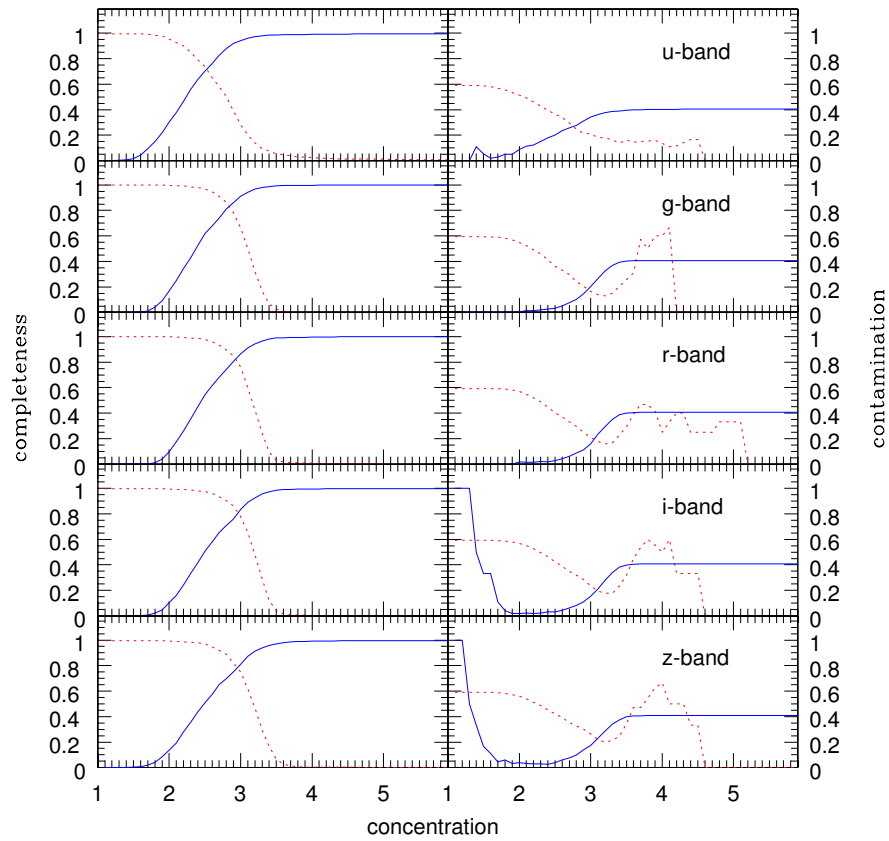
Figure 4.4: Completeness and contamination of early ($T < 1.5$) and late–type ($T \geqslant 1.5$) galaxies as a function of concentration index. Going from the upper to the lower panels the trends are shown for the concentration in the u, g, r, i and z bands. The solid and dotted lines are for late and early–type galaxies respectively.

confirm that there is a general correlation between the concentration and the Hubble type. The median of the distribution decreases going from ellipicals to irregulars with not too high a dispersion. In Figure 4.4 we quantify the goodness of this morphological classifier in the 5 Sloan bands. On the left panel the solid and dotted lines represent the completeness for late and early–types respectively while in the right panels the solid and dotted lines represent the contamination to late–type from early–types and vice–versa. The contamination from later–types when selecting $T \leqslant 1.5$ samples is always pretty high independently of the photometric band. On the other hand it is possible to produce clean samples of late–type objects (very low contamination from early–types) if we accept to reduce the completeness. We do not want to suggest here a better value of c for the selection of clean samples, since it depends on the wavelength and on the goal one has in mind. We simply want to stress that even if the concentration index is a very powerful tool it works better when supported by additional parameters aiming to quantify the residual substructures, as we show in section 4.4.6.

4.4.4 Bulge–to–disk ratio

The bulge–to–total light ratio, also known as bulge–to–disk ratio (B/T), is defined as the fraction of the total galaxy light contained in the bulge component. It provides a measure of morphology since it is sensitive to how centrally concentrated is the galaxy surface brightness profile. Since the Hubble tuning fork can be considered as a sequence of increasing predominance of the bulge component of galaxies, it is expected that the B/T is able to distinguish between spheroidal and disk–like galaxies.

B/T is an output structural parameter of the decomposition code which therefore provides quantitative and repeatable morphological classification, in addition to measurements of internal structures.

Galaxies with a given morphology have a fairly wide range in the bulge–to–disk ratio. Nevertheless this structural parameter correlates well with the Hubble type, the median of B/T decreases going from ellipticals to irregulars. This trend is clearly visible in Figure 4.5 where the distribution of B/T against the Hubble type is plotted for the galaxies in our photometric sample whose surface brightness distribution is modelled (see Table 4.1). Figure 4.5 contains 4 large panels. The upper ones correspond to galaxies which are modelled using a de Vaucouleurs law for the bulge and an exponential profile for the disk while in the lower ones we modelled the two photometric components with a Sérsic plus an exponential profile. The values of B/T are in general smaller for early–type galaxies when modelled with a Sérsic profile and they show a higher dispersion for later types. The panels on the right differ from the ones on the left in the fact that only the values of B/T for galaxies with an axial ratio smaller than 0.5 are present. We are showing them in order to be consistent with what we claim in section 3.4.2. The
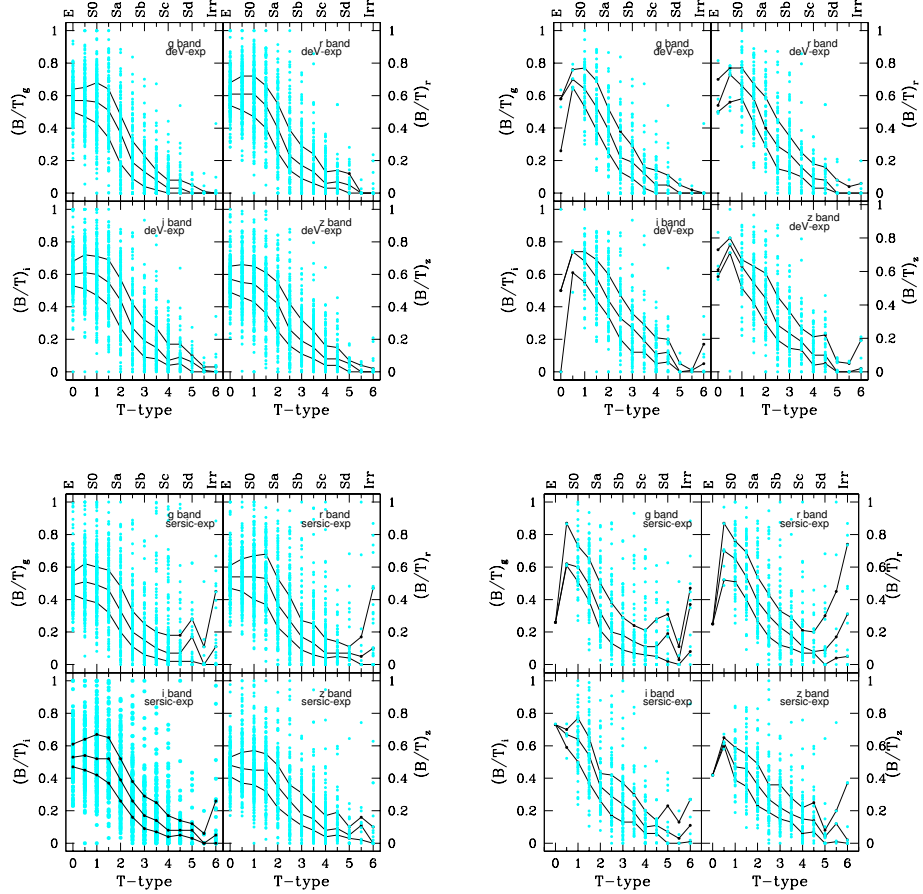
Figure 4.5: Distribution of the bulge–to–disk ratio (B/T) as a function of the Hubble type in the g, r, i and z bands. The plots on the left are for all the galaxies in the photometric sample while the ones on the right–hand side are constrained to the galaxies with a disk axial ratio b/a smaller than 0.5. A de Vaucouleurs plus exponential profile is fitted to the galaxies in the upper panels, while a Sérsic plus exponential model is applied to the galaxies in the lower panels. The solid lines show the median, the upper and the lower quartiles of the distribution.
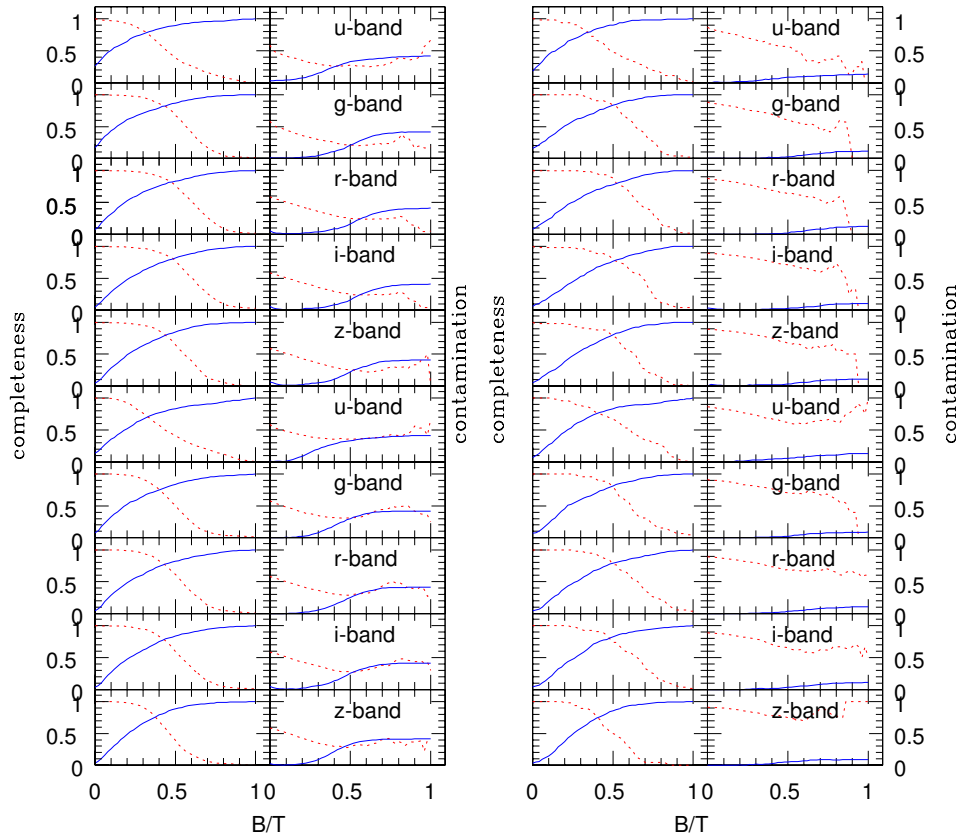
Figure 4.6: Completeness and contamination of early $(T < 1.5)$ and late–type $(T \geqslant 1.5)$ galaxies as a function of the bulge–to–total light ratio. The distributions in the 5 photometric bands $(u, g, r, i$ and $z)$ for a de Vaucouleurs plus exponential profile (first five rows) and a Sérsic plus exponential fit (last five rows) are shown going from the upper to the lower panels. The plots on the left are for all the galaxies in the photometric sample while the ones on the right–hand side are constrained to the galaxies with a disk axial ratio b/a smaller than 0.5. The solid and dotted lines are for late and early–type galaxies respectively.

behaviour of B/T does not change when we consider only edge–on systems. Each of the 4 panels is composed of 4 graphs. The only difference is the photometric band in which B/T is measured.

Figure 4.6 shows clearly that B/T can successfully be used to distinguish E/S0 galaxies from spiral galaxies. The large panels differ in the fact that the one on the right is for highly inclined systems ($b/a < 0.5$) while the one on the left includes all the galaxies in the 5 photometric bands for which the decomposition into bulge and disk is available. In the two columns which composed each panel we find the completeness on the left–hand side and the contamination on the right–hand side. Finally, the first five rows show the results for a de Vaucouleurs plus exponential fit (in the u, g, r, i and z bands from up to bottom) and the last five rows for a Sérsic plus exponential decomposition.

When looking at the complete sample we observe that for galaxies modelled with a de Vaucouleurs plus exponential profile the completeness of the two samples balances when B/T ≈ 0.45 at $\approx 80\%$. The only exception is given by the u band, that we actually advise not to use since the photometry is very poor. In the case of a Sérsic plus exponential fit the completeness of the two samples is smaller, $\approx 75\%$, at the point of balance, which is actually reached at a lower value of B/T. The contamination to late–type from early–type (solid line) can be very small, it is therefore possible to construct clean samples of late–type galaxies. The opposite it is not true since, above all for the decomposition with a Sérsic law, the contamination is never smaller than $\approx 30\%$. Samples of edge–on systems tend to exclude early type objects. As a consequence the completeness of early and late–type samples still balances at $\approx 80\%$ but the contamination to late–type galaxies from early–type is less than $\sim 10\%$. The opposite happens for the contamination to early–type from late–type objects which is extremely high.

Despite the model dependent nature of this structural parameter we demonstrate that it is a good morphological classifier with a well quantified behaviour.

4.4.5   Sérsic index

It was long believed that the light profile of ellipticals and spiral bulges could be described by the de Vaucouleurs $r^{1/4}$ law while the light distribution in disks was well fitted by the exponential profile. Further studies demonstrated that the more general, $r^{1/n}$, Sérsic profile was more suited to better characterize the galaxy brightness profile. Although we do not use the Sérsic parameter in our final classification, we show in Figure 4.7 the distribution of the Sérsic index for the whole photometric sample and the 7 morphologically classified subsamples in the g, r, i and z bands. It is evident that many ellipticals and bulges of spirals have less cuspy cores and all the range of values is covered. In agreement with Khosroshahi et al. (2004) we
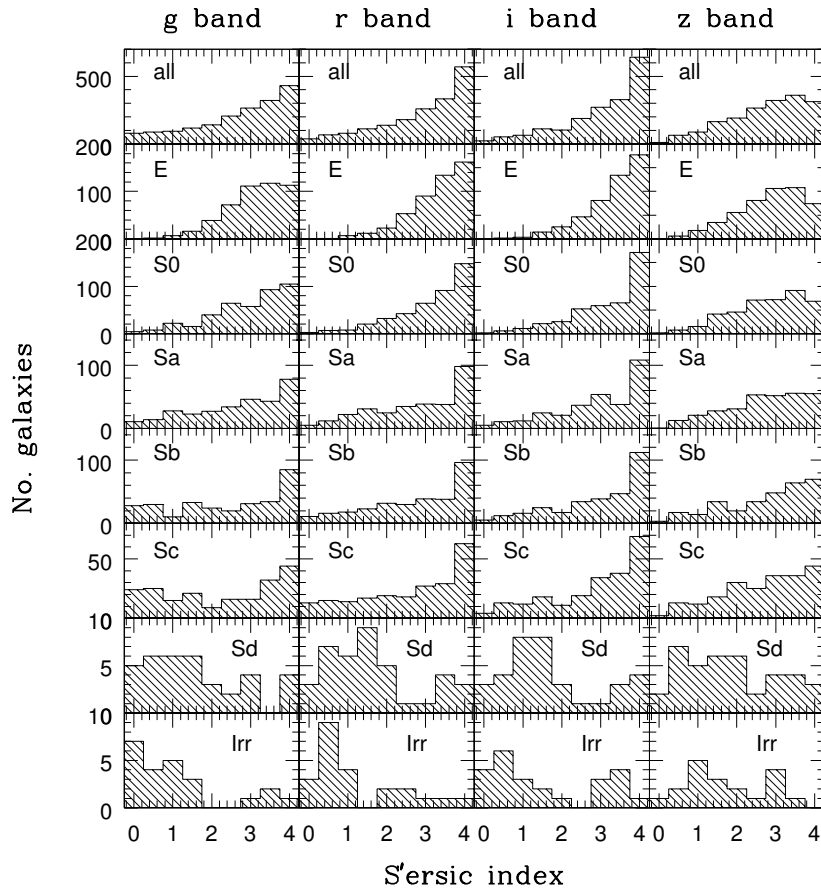
Figure 4.7: Distribution of the Sérsic parameter n for the galaxies in our photometric sample which are decomposed and have a $\chi^2 > 0.35$. The different columns are for the g, r, i and z bands; while the 8 lines show the distribution of the whole sample and of the elliptical, lenticular, early–spiral, late–spiral and irregular galaxies (from the upper to the lower panel).
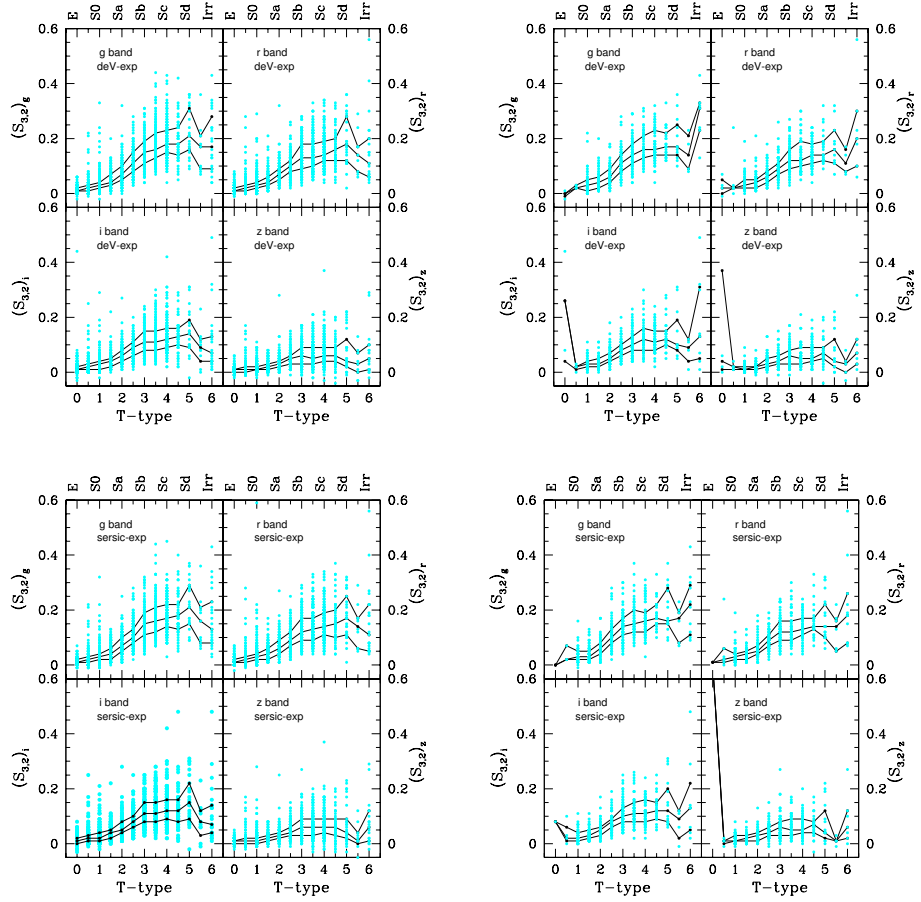
Figure 4.8: As Figure 4.5 but for the residual parameter $S_{3,2}$.

find that n does not correlate with the absolute magnitude and cannot be used as a distance indicator as suggest by Young & Currie (1994).

4.4.6   Residual and asymmetry parameters

Additional information on the morphology of galaxies can be derived from residuals from the smooth model fits and from the analysis of asymmetries in the galaxy light distribution.

For each modelled object two residual parameters, R_T and R_A, are calculated on the residual image within 10 circular apertures whose radii are multiples of the seeing–deconvolved half light radius, r_{hl}, so that the same fraction of the area is sampled for each galaxy. According to Schade et al. (1995)
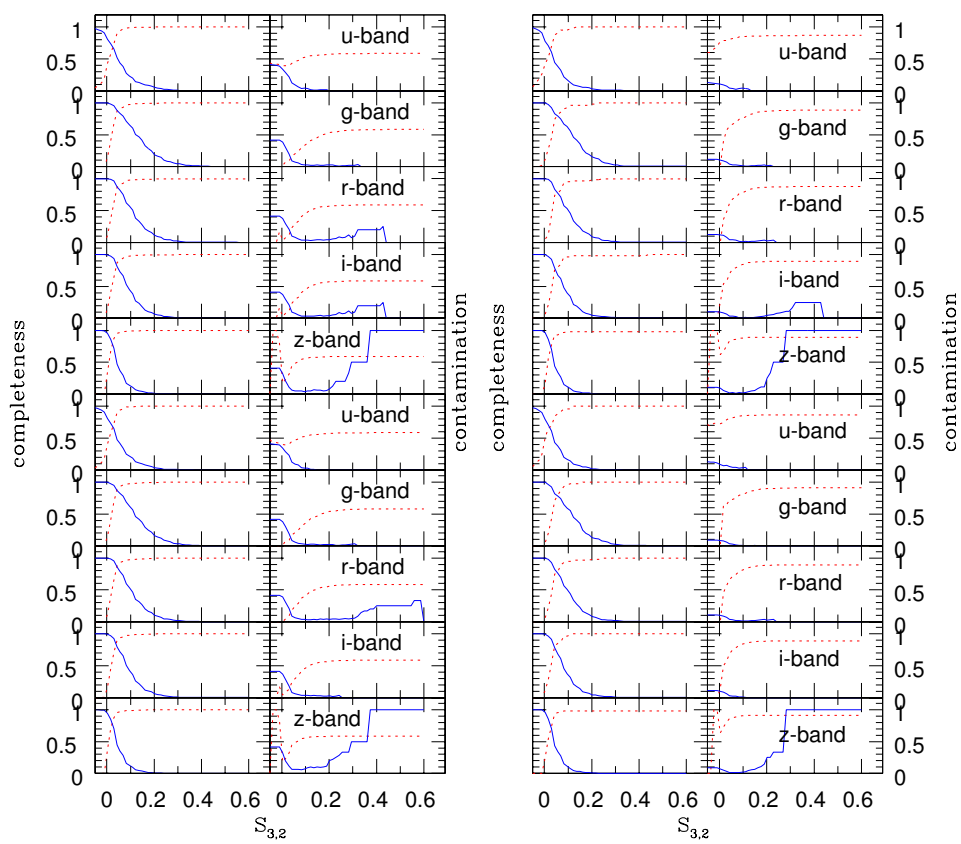
Figure 4.9: As Figure 4.6 but for the residual parameter $S_{3,2}$.
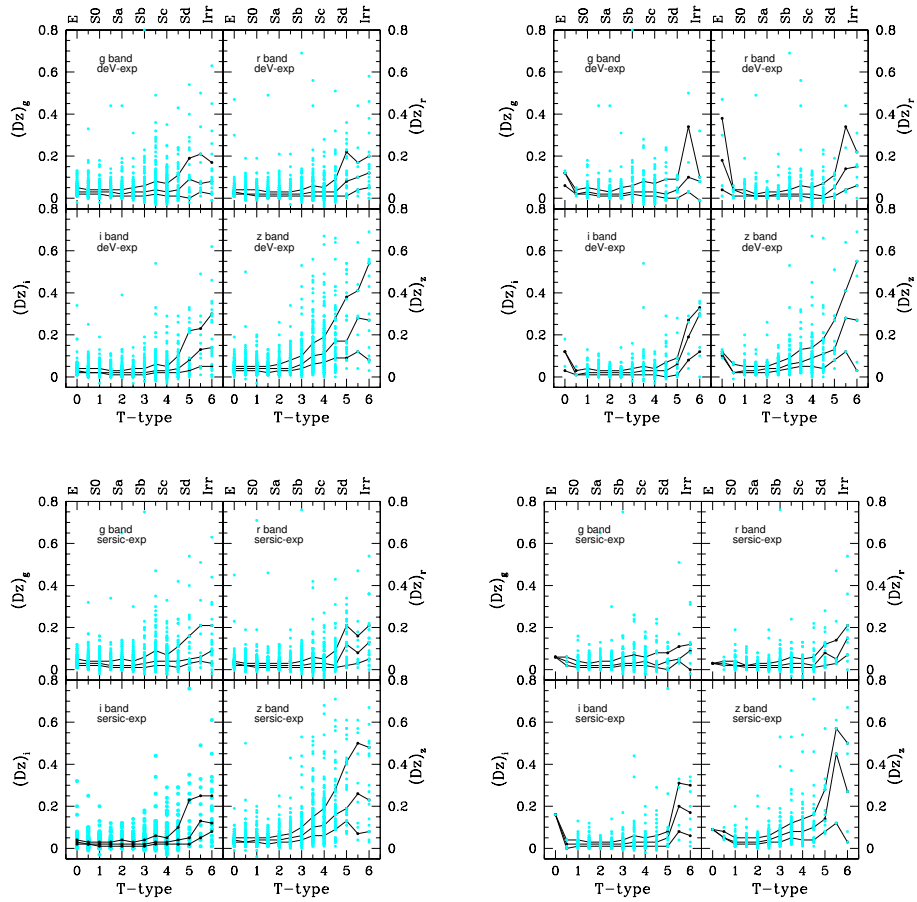
Figure 4.10: As Figure 4.5 but for the asymmetry index Dz.
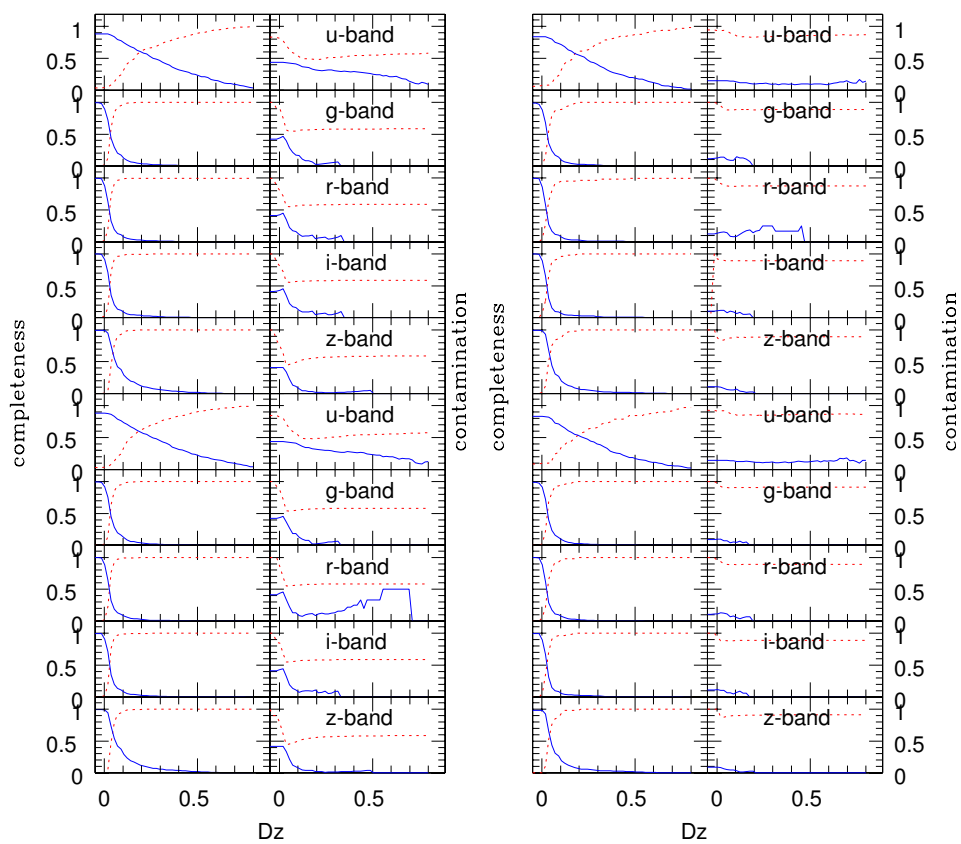
Figure 4.11: As Figure 4.6 but for the asymmetry index Dz.

$$R_T = \frac{\Sigma \frac{1}{2}|R_{ij} + R_{ij}^{180}|}{\Sigma I_{ij}} - \frac{\Sigma \frac{1}{2}|B_{ij} + B_{ij}^{180}|}{\Sigma I_{ij}}, \qquad (4.3)$$

and

$$R_A = \frac{\Sigma \frac{1}{2}|R_{ij} - R_{ij}^{180}|}{\Sigma I_{ij}} - \frac{\Sigma \frac{1}{2}|B_{ij} - B_{ij}^{180}|}{\Sigma I_{ij}}. \qquad (4.4)$$

where R_{ij} and R_{ij}^{180} are the flux measured in the residual image at pixel position (i, j) and the (i, j) rotated by 180°; B_{ij} and B_{ij}^{180} are similar quantities computed over pixels flagged as background in the segmentation image; and I_{ij} is the flux at the position (i, j) on the observed galaxy image. Following Im et al. (2002) we define the residual parameter $S = R_T + R_A$. The residual substructure parameter S provides a measure of the total substructures, like spiral features, dust lanes, bars and HII regions present in a galaxy. We use a fixed radius, $r = 2r_{hl}$, corresponding to two times the radius which includes half of the total light of the galaxy, in order to quantify these substructures, since we expect the largest residuals to be in that region.

Figure 4.8 shows that the residual substructure parameter correlates with the Hubble type. It increases with T, which is expected since it quantifies the deviation of the surface brightness profile of the galaxies from the bulge plus disk model we assume. Since no attempt is performed to parametrize bar structures, spiral arms, clumps or other non–smooth and asymmetrical components we should find them in the residual image and quantify them with S. Therefore elliptical galaxies, characterised by a smooth light distribution, have a very low value of S which indeed increases for late–spirals and irregulars. From Figure 4.8 it is clear that the trend of the residual structure parameter depends on the observing photometric band. The trend is pretty flat in the reddest z band. The two main reasons are that: most of the galaxy's substructures are related to star formation events, and bluer bands are more sensitive to them; the photometry in the g and r band is deeper and it allows to detect fainter structures. The residual structure parameter is a good substructures quantifier and it is effective in separating early from late–type galaxies in the g and r bands. Nevertheless the contamination from late–type galaxies in early–type sample and vice–versa is always extremely high. However, the use of this parameter in combination with other morphological quantifiers can have interesting applications, for e.g. in cleaning E/S0 sample from Sa galaxies.

In section 3.4.1 we introduce a residual parameter, that measures the absolute strength of the residuals, defined as the ratio between the absolute value of the residual light over the luminosity of the model image

$$G_2 = \frac{\sum |D_{ij}|}{L_{model}} \tag{4.5}$$

where the total counts in the residual image, $\sum D_{ij}$, simply result in the difference between the luminosity of the observed and modelled galaxy. It is a measure of the goodness of the fit and it behaves in a similar manner to the residual substructure parameter described above. Due to its simple definition it is worth including it in our study.

We finally want to mention another important residual asymmetry parameter, Dz, that can be retrieved as output of the bulge–to–disk decomposition. It is measured outside the half–light radius of the galaxy and it is the sum, normalized to the total object flux, of the fluxes in the pixels with symmetrical counterparts with respect to the object center which do not belong to the object. As consequence of its definition it is sensitive to tidal arms caused by galaxy mergers. These cold arms cannot form from hot systems like ellipticals, since the velocity dispersion of the stars has to be low in order to create these narrow features. Dz is not relevant in our study, since we are dealing with isolated galaxies, but can be use for high–redshift studies to select interacting galaxies.

4.5 The classification

The Hubble classification scheme is still widely used by astronomers, although we do not give any longer an evolutionary meaning to the "early" and "late" type nomenclature. Since all the galaxies in our sample are classified into Hubble types, we keep open in Figure 4.12 and 4.13 the possibility to locate ellipticals, lenticulars, spirals and irregulars in the observational multi–parameter space we define. In our classification we have model–dependent parameters and the mentioned figures show that all the correlations we investigate have the same trend when the decomposition is performed using a de Vaucouleurs profile for the bulge component and an exponential for the disk as when a Sérsic law is chosen to fit the galactic bulge.

Some of these relations are studied in detail by Bershady et al. (2000) who identify colour, concentration, asymmetry and surface brightness as the sufficient parameters needed to define a quantitative classification system. They claim the best correlation to be the one between concentration index and colour and they also provide 6 cuts in their four–dimensional space to identify early, intermediate and late type spirals. High concentration objects have high surface brightness and red colours. They are early–type galaxies. Since we want to find a more physical alternative to the Hubble classification, we simply point out that other interesting relations arise. Among them the choice of $(B/T)_r > 0.4$ and $c_r > 2.9$ are good to select sample of E/S0. To

Figure 4.12: Correlations between the photometric and structural quantities which define our multi–parameter space. The points refer to the 894 galaxies in our spectroscopic sample which are successfully modelled, with a de Vaucouleurs plus exponential model, separately in the 5 photometric bands and for which we have the stellar masses. The points are colour–coded according to the Hubble–type given by the visual classification.

Figure 4.13: Correlations between the photometric and structural quantities which define our multi–parameter space. The points refer to the 1040 galaxies in our spectroscopic sample which are successfully modelled, with a Sérsic plus exponential model, separately in the 5 photometric bands and for which we have the stellar masses. The points are colour–coded according to the Hubble–type given by the visual classification.
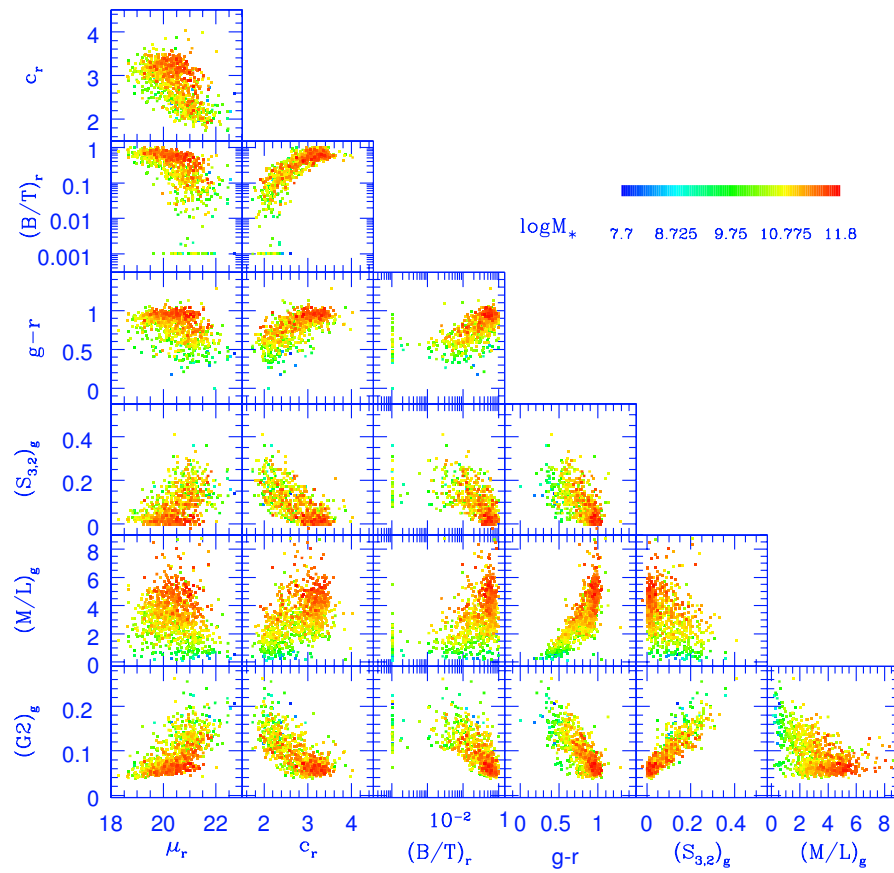
Figure 4.14: As in Figure 4.12 but the point are colour–coded according to their stellar masses.
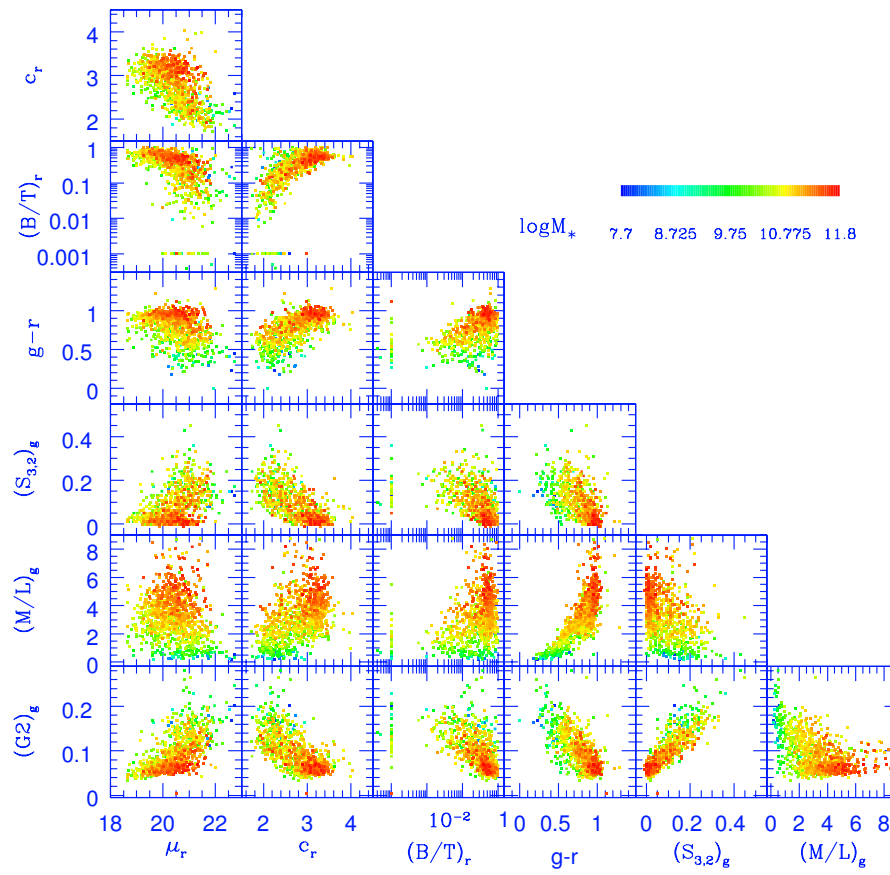
Figure 4.15: As in Figure 4.13 but the point are colour–coded according to their stellar masses.
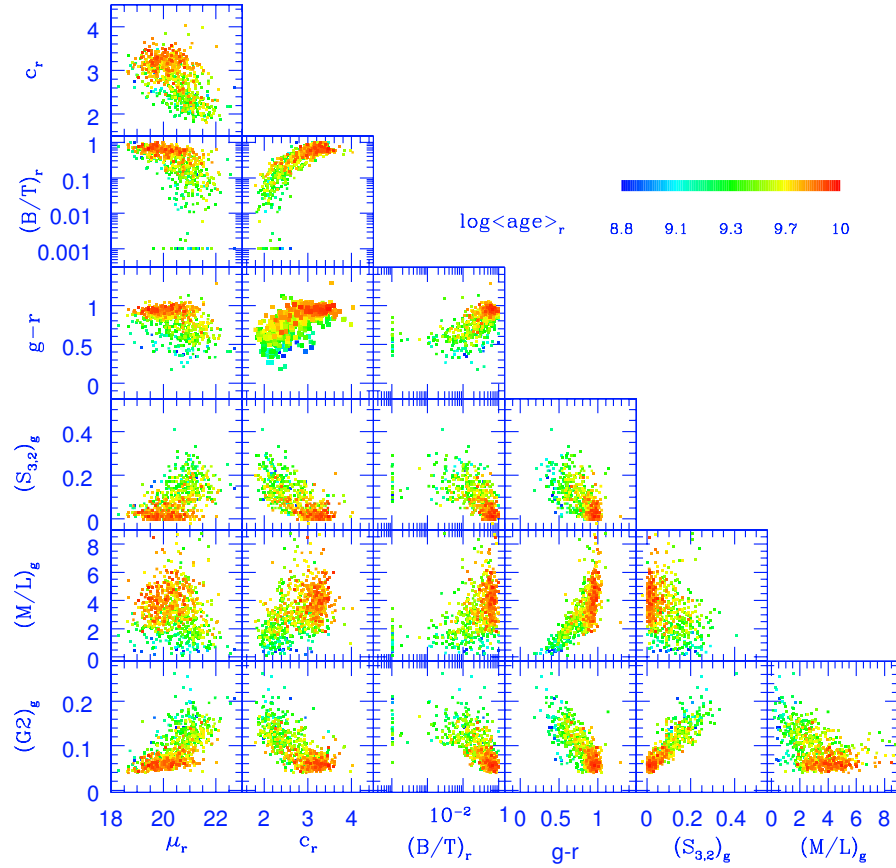
Figure 4.16: Correlations between the photometric and structural quantities which define our multi–parameter space. The points refer to the 727 galaxies in our spectroscopic sample which are successfully modelled, with a de Vaucouleurs plus exponential model, separately in the 5 photometric bands and for which we have the stellar masses and mean stellar ages. The points are colour–coded according to r band magnitude–weighted mean stellar ages.
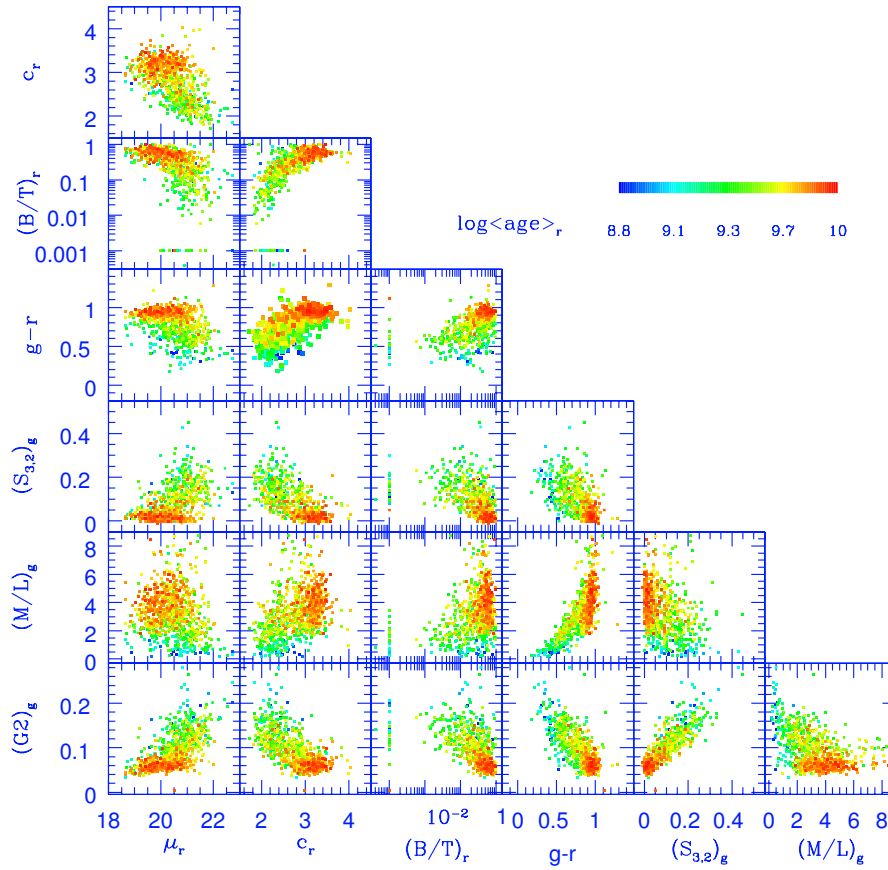
Figure 4.17: Correlations between the photometric and structural quantities which define our multi–parameter space. The points refer to the 842 galaxies in our spectroscopic sample which are successfully modelled, with a Sérsic plus exponential model, separately in the 5 photometric bands and for which we have the stellar masses and mean stellar ages. The points are colour–coded according to r band magnitude–weighted mean stellar ages.
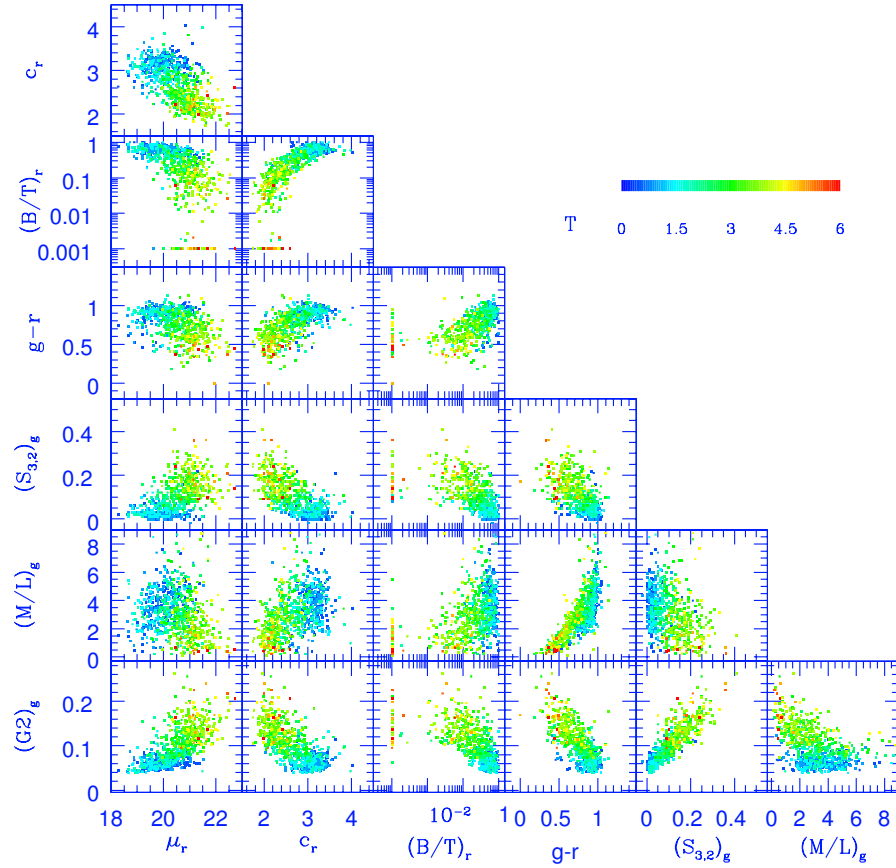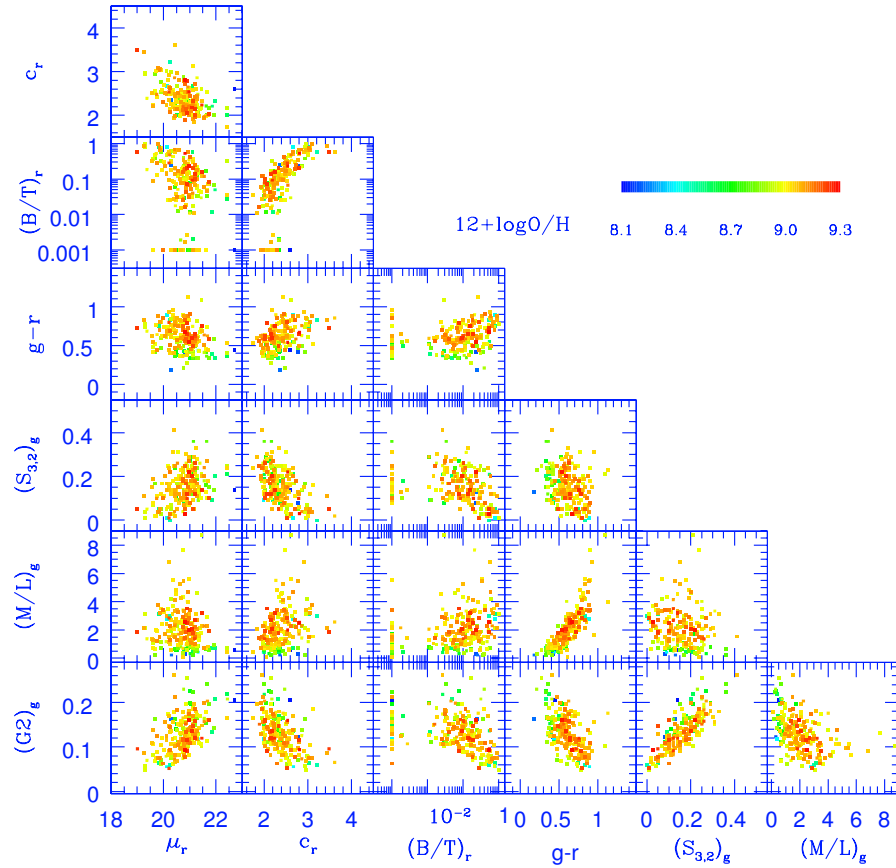
Figure 4.18: Correlations between the photometric and structural quantities which define our multi–parameter space. The points refer to the 213 galaxies in our spectroscopic sample which are successfully modelled, with a de Vaucouleurs plus exponential model, separately in the 5 photometric bands and for which we have the stellar masses and gas–phase metallicities. The points are colour–coded according to the value of $12 + logO/H$.
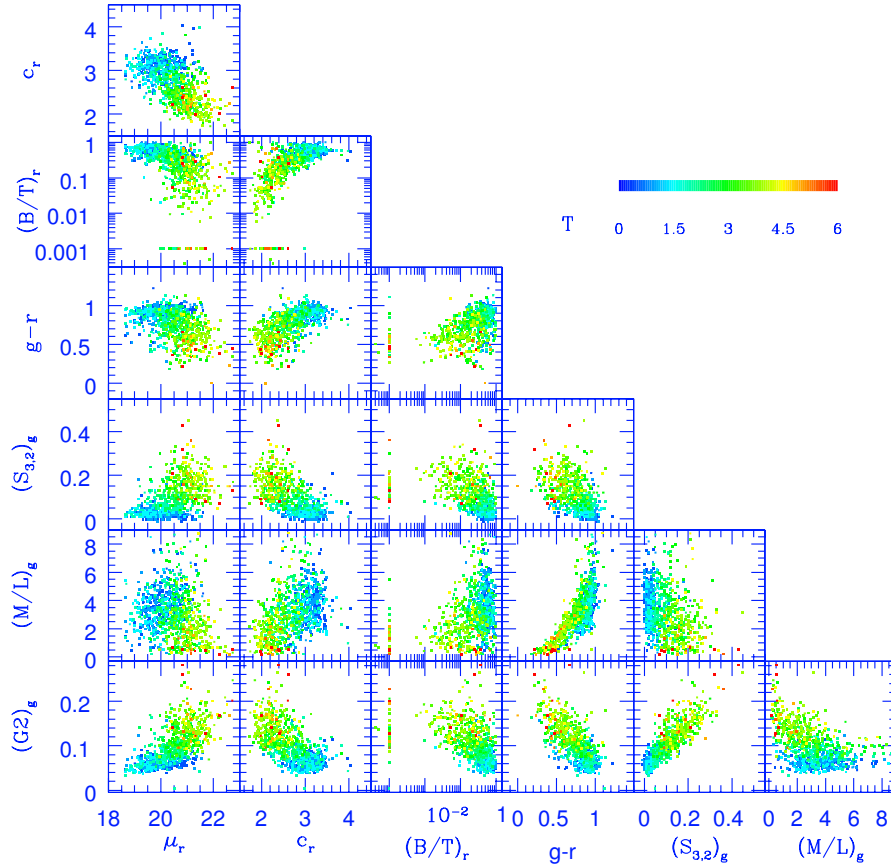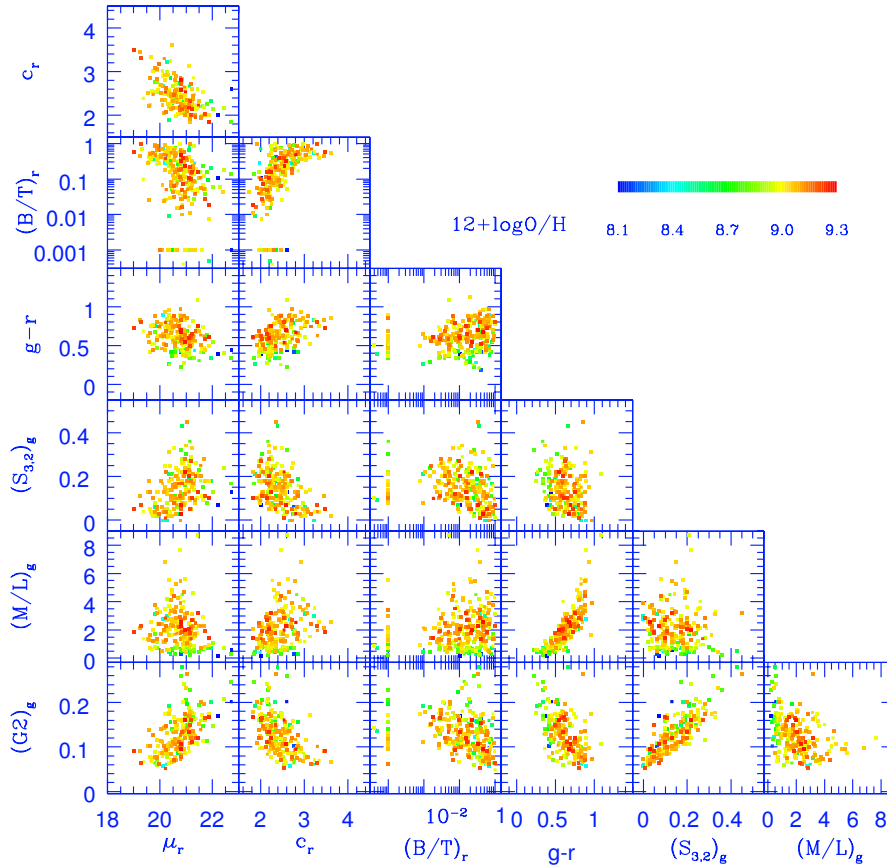
Figure 4.19: Correlations between the photometric and structural quantities which define our multi–parameter space. The points refer to the 270 galaxies in our spectroscopic sample which are successfully modelled, with a Sérsic plus exponential model, separately in the 5 photometric bands and for which we have the stellar masses and gas–phase metallicities. The points are colour–coded according to the value of $12 + logO/H$.

clean the sample from contamination of Sa galaxies one could use relations between residual parameters ($S_{3,2}$ and $G2$) with the concentration and the bulge–to–disk ratio.

The goal of this study is to show the possibility to select samples of galaxies with well defined physical properties. Therefore we extend our analysis including four parameters which describe the star formation history of the galaxy.

The 21 relations we investigate are colour–coded in Figure 4.14 and 4.15 with stellar masses, in Figure 4.16 and 4.17 with luminosity weighted mean stellar ages, and in Figure 4.18 and 4.19 with gas–phase metallicities. We comment on the most interesting correlations found in order to guide the reader through the plots.

In Figure 4.14 and 4.15

- high concentration objects are more massive (B/T vs c), but at the same high concentration the ones with higher surface brightness are less massive (c vs μ);

- the Kormendy relation (Kormendy 1977) is verified on all the plots which involve μ, except the one with M/L;

- very massive galaxies have high mass–to–light ratio. Low–mass galaxies instead span a wide range of M/L but they can be separated in colour. The spread in M/L increase towards redder colours;

- the dispersion in the g-r colour is larger when the mass–to–light ratio is measured in redder bands;

- the mass–to–light ratio clearly increases with mass.

When considering gas–phase metallicities our sample becomes smaller, 213 objects if the decomposition is performed with de Vaucouleurs plus exponential fit and 270 for the Sérsic plus exponential model. In Figure 4.18 and 4.19 we cannot claim any clear behaviour of the gas–phase metallicities in the correlations we identify. Nevertheless the comparison of these plots with the ones colour–coded with other quantities allows us some observations. Galaxies with old mean stellar ages and high masses (early–type, if we stay on the Hubble classification) show very high metallicities. To measure gas–phase metallicities we need nebular emission lines, therefore galaxies with on–going star formation. The fact that we calculate the value 12+logO/H for early systems means that they are forming stars. Gas–phase metallicities are measured from the SDSS spectra which are taken with 3 arcsec diameter fibers and sample therefore only the physical conditions at the center of the galaxy. Since no aperture correction is performed, the star formation activity is on–going at the center of these early–type systems. We also observe that the metallicities reached by these objects are very high. We confirm

the mass–metallicity relation (Tremonti et al. 2004) and that at the center of bulges stars form from a more metal enriched gas.

From the comparison of the plots colour–coded with the mean stellar ages and with the stellar masses we observe that:

- low values of the residual parameters ($S_{3,2}$ and $G2$) select old, massive galaxies. The constraint on the age being stricter;

- low mass galaxies have young stellar population.

4.6 Discussion & Conclusions

We use a sample of 1875 objects drawn from the Sloan Digital Sky Survey to show how photometric and structural parameters of galaxies can be successfully used to create galaxy samples with clearly defined physical properties. All the galaxies in our magnitude limited sample are morphologically classified by eye in 7 groups which cover all the Hubble morphological types. For 1588 of them a spectroscopic follow–up is performed. For all the galaxies in the photometric sample we perform a two–dimensional bulge to disk decomposition using different sets of parametric functions to model the light distribution. We assume that the disk is well described by an exponential profile while the bulge is fitted with a de Vaucouleurs law as well as with a more general Sérsic profile. We investigate how rest–frame colours, concentration index, bulge–to–disk ratio, residual and asymmetry parameters correlate with the Hubble type and we focus on their ability to select clean samples of early and late–type objects. We then define an observational multi–parameter plane including, in addition to the already mentioned parameters, the mean surface brightness within the effective radius and the mass–to–light ratio. Focusing on galaxy evolution, we notice that the study of asymmetric residuals is fundamental. Asymmetric features can be observed on the galaxy residual image and quantified by a set of indices in the presence of a star–forming regions or a recent merger event. The residual images of elliptical galaxies would therefore appear lacking in structures and to be pretty smooth in contrast to the residual image of spiral galaxies where regions of intense star formation and spiral arms are easily visible.

We finally show that galaxy structural parameters strongly depend on stellar masses and mean stellar ages, while the same is not observed for gas–phase metallicities. A strong correlation is also present between stellar masses and mean stellar ages, with massive galaxies having old stellar population. We conclude that the multi–parameter space we propose allows us to separate old, massive, bulge–dominated systems and young, low–mass, disk–dominated ones.

With our observational plane we cannot provide any constraint to select galaxies with a given metallicity since no correlation between structural

parameters and gas–phase metallicities is identified. Nevertheless an interesting additional application of our method allows us to select a group of early–type galaxies with on–going star formation which are not AGNs. This class of galaxies is expected in the hierarchical structure formation scenario (Kauffmann, White & Guiderdoni 1993) where elliptical galaxies form from major merger and are relatively young objects. Observationally they have been observed (Dressler & Gunn 1983) and are called E+A galaxies. In a recent paper Fukugita et al. (2004) identify three of these objects in our sample but using a different method. Surprisingly their objects are not the same ones for which we observe on–going star formation.

Chapter 5

Structural parameters

The correlations of the fundamental structural parameters of galaxies are investigated for a sample of 1865 morphologically classified galaxies in the u, g, r, i, z Sloan bands. The goal of this chapter is to examine the properties of galactic bulges and disks. In particular we consider the parameters which enter into the parametric functions commonly used to fit the galaxy light distribution: effective radius r_e and surface brightness μ_e of the bulge and disk scalelength r_h and central surface brightness μ_0 of the disk. We find that all disks obey the same luminosity–size relation while bulges of different morphological types lie on different slopes in the r_e–M_{bulge} plane. We also find that a correlation exists between disk and bulge structural parameters and in particular between r_e and r_h for early–type systems. We interpret this as observational support for secular evolution models.

5.1   Introduction

Galaxies come in a large variety of shapes, dimensions, colors and luminosities. In the last decades it has become possible to observe the diverse details of galaxies out to very large distance and very faint surface brightness owing to the latest generation of telescopes and satellites.

A major goal in contemporary astrophysics is to determine how galaxies formed and evolved. As we approach this goal it is fair to ask if the structure of galaxies provides any clues towards solving this problem. It is widely accepted that the morphological appearance of galaxies is related to their formation and evolution, and in general to the galaxy environment (Dressler 1980). In some previous studies the properties of bulges and disks have already been investigated (Andredakis, Peletier & Balcells 1995; de Jong 1996c), nevertheless these lack completeness. They consider only late–type galaxies, they do not consider different decompositions for early and late–type spirals, they use small and inhomogeneous samples.

The chapter is organized as follows. In section 5.2 we present the sam-

ple used and briefly describe the photometric, spectroscopic and model–dependent data. The correlations between bulge and disk properties are analysed in section 5.3. We summarize our conclusion and discuss their implication for galaxy evolution in 5.4

The Hubble constant is quoted as $H_0 = 100h$ km s^{-1} Mpc^{-1}. We assume throughout this chapter, unless otherwise stated, $h = 0.7$, $\Omega_M = 0.3$ and $\Omega_\Lambda = 0.7$.

5.2 The data

The sample we are using as well as the image reductions we perform are well described in chapter 3. In particular we consider in this study only the galaxies in the spectroscopic sample with $z \geqslant 0.005$, in order to avoid strong effects from peculiar velocity flows. In this way we exclude 18 galaxies of which 2 have negative redshift. The mean seeing in the Sloan is 1.5 arcsec and the image scale is 0.396 pixel arcsec^{-1}. We have only 4 objects for which the half–light radius is smaller than 1.5 arcsec. We do not apply any cut in angular sizes since the 4 small galaxies in our sample are not so compact as to be affected by seeing. We end up with a magnitude limited sample of morphologically classified galaxies with $r \leqslant 15.9$ and $0.005 \leqslant z \leqslant 0.12$. Morphological classification is carried out by correlating results of several human classifiers.

We investigate the importance of inclination corrections in measuring the galaxy surface brightness. In doing that we use the major, *isoA*, and minor, *isoB*, semi–axis measured by the Sloan PHOTO pipeline and we derive the galaxy axis ratio. The surface brightness correction for inclination effects, taking internal extinction into account is

$$\mu = \mu' - 2.5C \log(isoA/isoB) \tag{5.1}$$

where the coefficient $0 \leqslant C \leqslant 1$ discriminates between fully transparent, $C = 1$, and optically thick, $C = 0$, galaxies. In the case of $C = 1$ the correction for highly inclined objects can reach a value of ~ 2 mag arcsec^{-2}. The average correction for our sample is ~ 0.48 mag arcsec^{-2}.

We use **Gim2D** (Simard et al. 2002) to perform a two–dimensional bulge–to–disk decomposition for all the galaxies in the u, g, r, i and z photometric bands. Structural parameters are retrieved using de Vaucouleurs and Sérsic parametric functions for the light distribution in the bulge component of the galaxies and the exponential profile for the disk.

The stellar masses measured by Kauffmann et al. (2003) are also used.

Band	deV + exp						Sersic + exp					
	β	ζ_e	γ	ζ_{eS}	δ	ζ_{lS}	β	ζ_e	γ	ζ_{eS}	δ	ζ_{lS}
u	0.42 ± 0.06	0.51	0.18 ± 0.06	0.23	0.11 ± 0.05	0.24	0.63 ± 0.05	0.70	0.30 ± 0.05	0.40	0.27 ± 0.04	0.52
g	0.64 ± 0.02	0.77	0.40 ± 0.04	0.44	0.10 ± 0.06	0.13	0.63 ± 0.02	0.80	0.44 ± 0.03	0.52	0.36 ± 0.04	0.46
r	0.61 ± 0.02	0.78	0.36 ± 0.03	0.47	0.15 ± 0.04	0.22	0.66 ± 0.02	0.83	0.39 ± 0.03	0.52	0.19 ± 0.04	0.30
i	0.64 ± 0.02	0.81	0.40 ± 0.03	0.53	0.20 ± 0.04	0.27	0.63 ± 0.02	0.83	0.41 ± 0.03	0.56	0.24 ± 0.04	0.35
z	0.65 ± 0.02	0.80	0.28 ± 0.03	0.45	0.14 ± 0.03	0.26	0.57 ± 0.02	0.80	0.31 ± 0.03	0.46	0.15 ± 0.03	0.30

Table 5.1: The least–squares fitting results of the parameters in the r_e–M_{bulge} relation. The data are shown for galaxies modelled with de Vaucouleurs plus exponential profile and Sérsic plus exponential fit in the 5 Sloan photometric bands. β, γ and δ are the exponents of the power laws describing the dependence between the luminosity and the bulge scalelength respectively for early–type systems ($0 \leqslant T \leqslant 1$), early–type spirals ($1 < T \leqslant 3$) and late–type spirals ($3 < T \leqslant 5$). The ζ columns are the correlation coefficients.

5.3 The analysis

In this section we analyse the statistics of bulge and disk parameters. We investigate how the intrinsic properties of the two photometric components of galaxies correlate with the morphological T–type of the Hubble visual classification. We then consider possible correlations between bulge and disk parameters independently. We finally look at the relationships between bulge and disk structural parameters. In the presented plots we consider only the objects for which the errors on the investigated quantities are smaller than 30% of the quantity itself therefore, to preserve clarity, we do not show error bars in the plots.

5.3.1 Galactic bulges

The photometric bulge component of the galaxies is modelled in our analysis in two ways: general Sérsic or de Vaucouleurs law. The effective radius of the bulge (r_e), enclosing half the total luminosity, and the effective surface brightness (Σ_e) are two of the parameters which describe these parametric functions. The Sérsic law in terms of luminosity assumes the form

$$\Sigma(r) = \Sigma_e \cdot \exp\left\{-b \cdot [(r/r_e)^{1/n} - 1]\right\} \qquad (5.2)$$

where $\Sigma(r)$ is the surface brightness at radius r, and Σ_e is the effective surface brightness. The parameter b is related to the Sérsic index n and set equal to $1.9992n - 0.3271$. The de Vaucouleurs profile is a special case of the previous one for $n = 4$. The $r^{1/4}$ law generally gives a good description of the light distribution in elliptical galaxies. The use of the same fitting function for the bulges of spiral galaxies is motivated by the assumption that they form in the same way. We actually show in section 4.4.5 that less
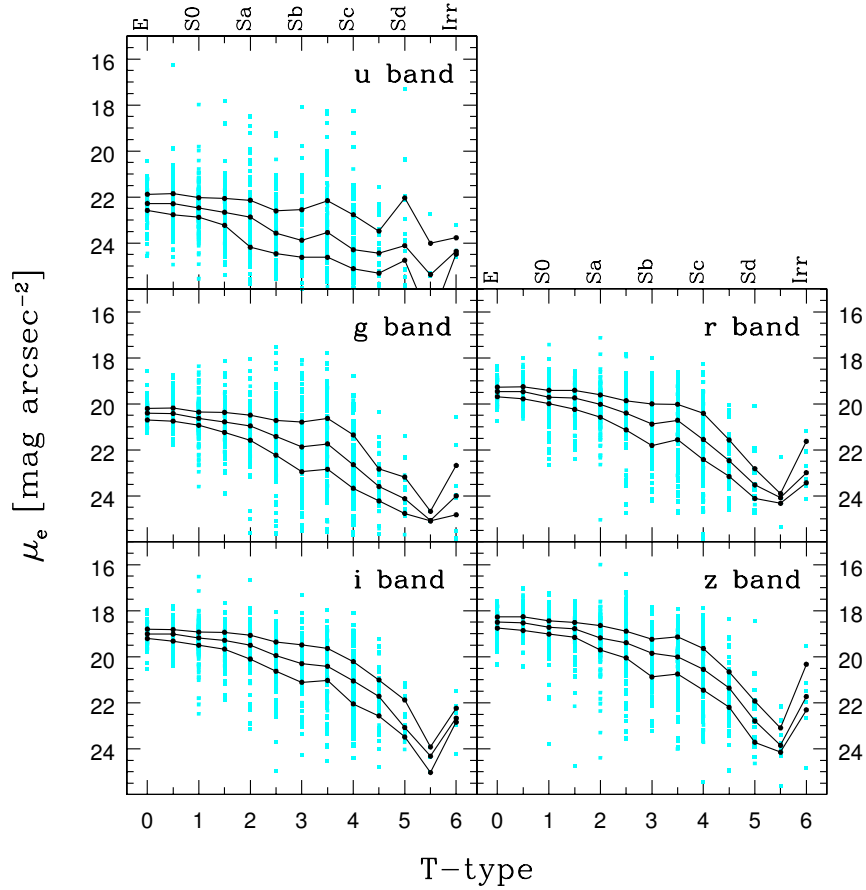
Figure 5.1: Intrinsic surface brightness of the bulge, corrected for galactic extinction, as a function of the Hubble morphological T–type. A Sérsic plus exponential profile is fitted to the galaxies surface brightness. Each point represents the value of μ_e for each galaxy successfully modelled in the u, g, r, i and z photometric bands. The solid lines show the median, the upper and the lower quartiles of the distribution.
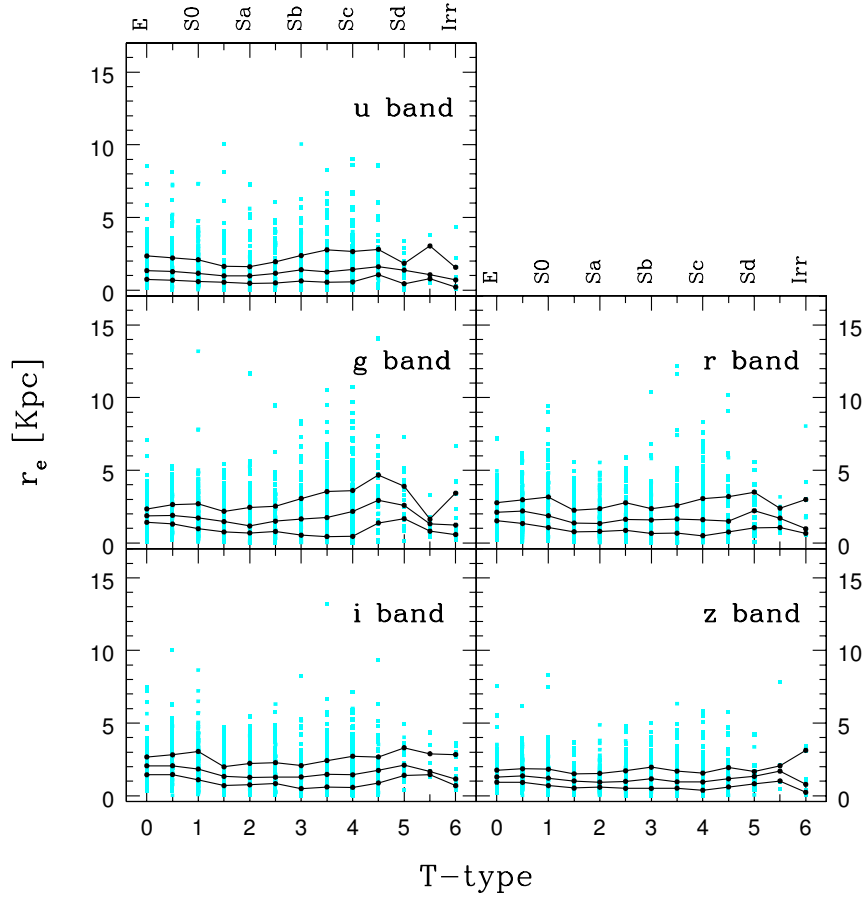
Figure 5.2: Effective radius of the bulge as a function of the Hubble morphological T–type. A Sérsic plus exponential profile is fitted to the galaxies surface brightness. Each point represents the value of r_e for each galaxy successfully modelled in the u, g, r, i and z photometric bands. The solid lines show the median, the upper and the lower quartiles of the distribution.
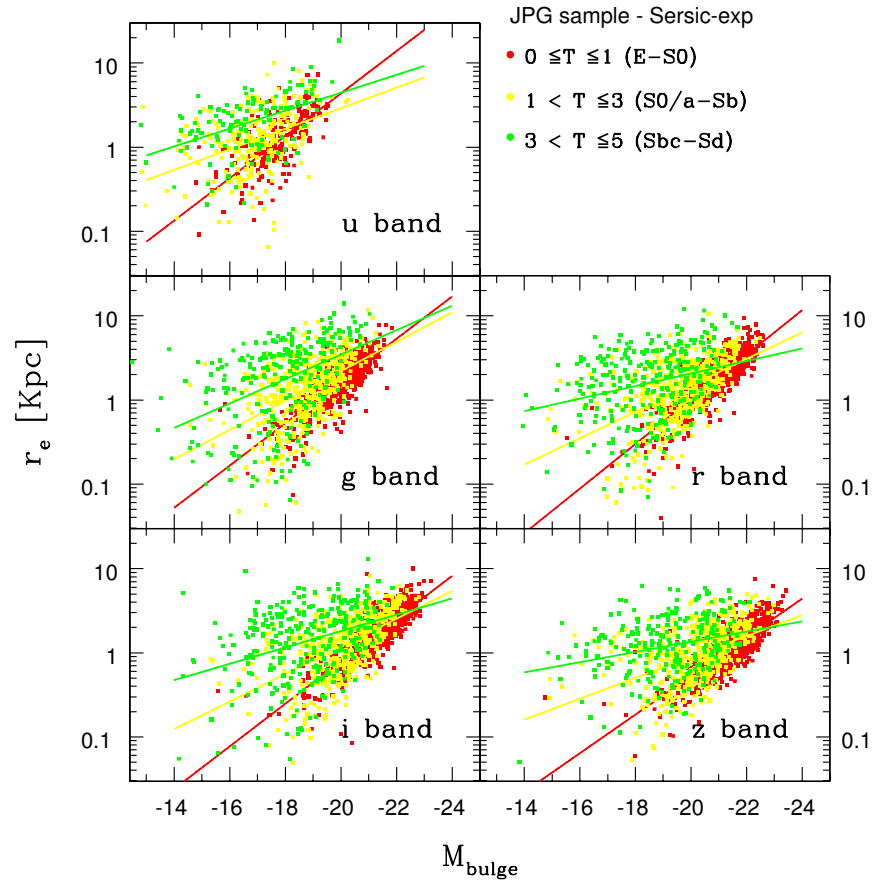
Figure 5.3: Relation between the effective radius of the bulge and the absolute magnitude of the bulge. Each point represents the value of r_e and M_{bulge} for galaxies successfully modelled in the u, g, r, i and z photometric bands using a Sérsic plus exponential profile. Red points are for early–type systems $(0 \leqslant T \leqslant 1)$, yellow points for early–type spirals $(1 < T \leqslant 3)$ and green points for late–type spirals $(3 < T \leqslant 5)$. The same color scheme applies to the solid lines. They are linear regression fits to the data.

cuspy profiles can give an equally good fit for elliptical galaxies and that the bulges of late–type spirals mostly have an exponential profile.

We derive the total flux in the bulge component by integrating equation 5.2 from $r = 0$ to infinity

$$F_{bulge} = 2\pi n \ e^k \ k^{-2n} \ r_e^2 \ \Gamma(2n) \ \Sigma_e \tag{5.3}$$

where Γ is the incomplete gamma function. In the particular case of de Vaucouleurs law

$$F_{bulge} = 7.214\pi \ r_e^2 \ \Sigma_e \tag{5.4}$$

The effective surface brightness of the bulge is then easily retrieved as

$$\mu_e = m_{bulge} + 2.5 \ \log(q \ \pi \ r_e^2) \tag{5.5}$$

where $q = 8 \, e^k \, k^{-2n} \, \Gamma(2n)$ and for $n = 4$ $q = 7.214$. It is worth noting that in measuring the apparent magnitude of the bulge, $m_{bulge} = m - 2.5 \ \log(B/T)$, we are considering the apparent magnitude of the galaxy, m, already corrected for foreground Galactic extinction, using the reddening map of Schlegel, Finkbeiner & Davis (1998), and for k–correction, using the routines in KCORRECT $v2\_16$ (Blanton et al. 2003). B/T is the bulge–to–disk ratio. The intrinsic surface brightness is finally obtained after a dimming correction, $10 \log(1 + z)$, is applied.

In this section we show results only for the case of bulge–to–disk decomposition performed with a Sérsic profile. In the case of a de Vaucouleurs fit the retrived μ_e and r_e do not show large discrepancies. Only the effective radius of the bulge is somewhat larger for all the morphological types and in all the photometric bands.

Figure 5.1 describes the distribution of the intrinsic surface brightness of the bulge for different galaxy types. We observe a mild decline which becomes steeper towards later galaxy types. Even if with a large scatter, in particular for intermediate types, there is a good correlation of μ_e with morphology. An increase of the intrinsic surface brightness is observed in all the photometric bands for irregular galaxies. This is possibly due to the fact that star forming galaxies typically show irregular morphology. Our sample is biased against later types so that the statistics for these objects is low and therefore the observed growth may not be real. The interesting result is that the bulges of early–type galaxies turn out to be more compact and more luminous compared to late–type galaxies.

Figure 5.2 has the purpose of showing that a wide range in bulge scale-lengths is covered by all galaxy types. The dispersion is smaller in the z

band. A possible explanation is related to the smaller effect of dust and to the fact that bulges are brighter in that band and therefore the fitting routine gives better results. We do not find any trend for the distribution of the effective radius of the bulge with respect to T-type. This is expected since the Hubble type is a scale–size independent parameter (de Jong 1996c).

The relation between the effective radius of the bulge and the absolute magnitude of the bulge is shown in Figure 5.3. We divide the galaxies in 3 groups according to their morphology: early–type systems with $0 \leqslant T \leqslant 1$, essentially elliptical and lenticular galaxies, early–type spirals with $1 < T \leqslant 3$ and late–type spirals with $3 < T \leqslant 5$. To quantify the observed relation between r_e and M_{bulge} we use a simple analytic formula to perform the fit

$$\log(r_e) = -0.4a M_{bulge} + b \tag{5.6}$$

where a and b are two fitting constants. The relation between r_e and the luminosity of the bulge is a power law, $r_e \propto L^{\beta,\gamma,\delta}$. The different exponents are for the three subsamples considered and their values are quoted in Table 5.1. The results for galaxies decomposed using a de Vaucouleurs profile are also shown for comparison in Table 5.1. As already mentioned, our choice to discuss only the relations obtained using the data retrieved with a Sérsic fit is justified by two main reasons. The final correlations do not depend on the decomposition used. Only in the u band the results are considerably different, mostly as consequence of the poor photometry in that filter. The second point is that the correlation coefficients are always slightly larger for a Sérsic fit, meaning that the correlations are more tight.

Figure 5.3 clearly shows that larger bulges are more luminous, as we expected. What is interesting to point out is that the bulges of galaxies with different morphology do not follow the same relation. It is evident that the bulges of ellipticals and lenticulars lie on a pretty tight ($\zeta \sim 0.8$) and steep ($\beta \sim 0.6$) slope. The exponent of the power law is more shallow for early ($\gamma \sim 0.4$) and late–type spirals ($\delta \sim 0.2$), and the dispersion for these two subsamples is much higher. Possible explanations are that the bulge component of galaxies either form or evolve in a different way in different galaxy types.

5.3.2 Galactic disks

In this section we examine the structural parameters of the disk galactic component. The exponential profile

$$\Sigma(r) = \Sigma_0 \exp^{-r/r_h} \tag{5.7}$$

is the parametric function normally used to fit the surface brightness profile of the disk. The face–on central surface brightness Σ_0 and the disk scale-
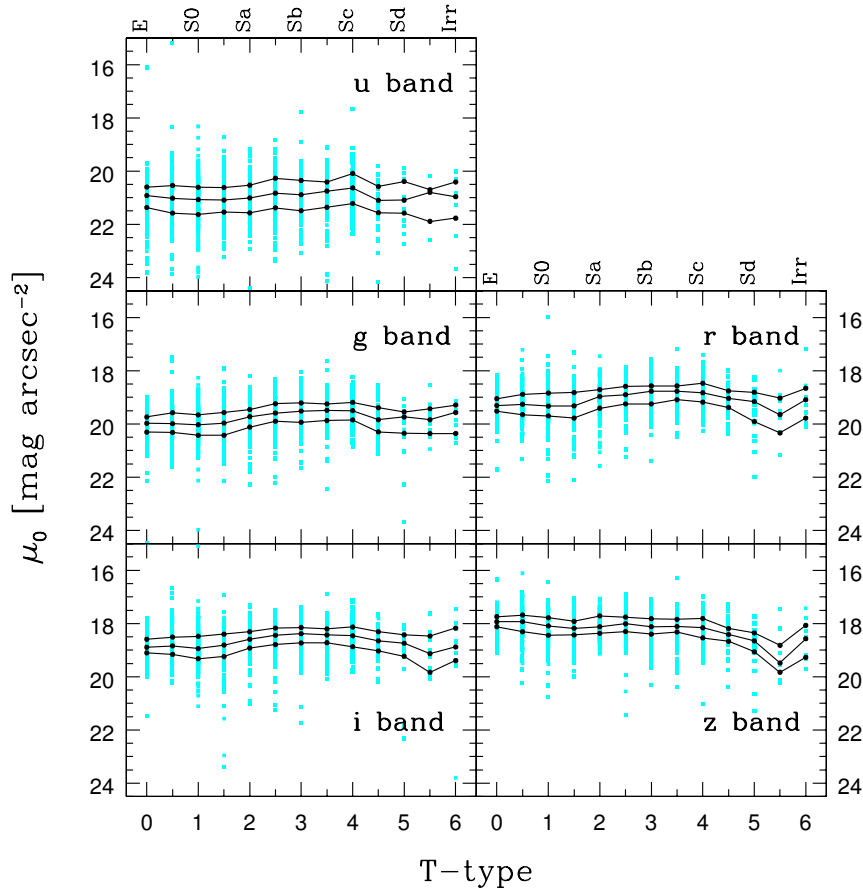
Figure 5.4: Intrinsic central surface brightness of the disk, corrected for galactic extinction, as a function of the Hubble morphological T–type. A Sérsic plus exponential profile is fitted to the galaxies surface brightness. Each point represents the value of μ_0 for each galaxy successfully modelled in the u, g, r, i and z photometric bands. The solid lines show the median, the upper and the lower quartiles of the distribution.
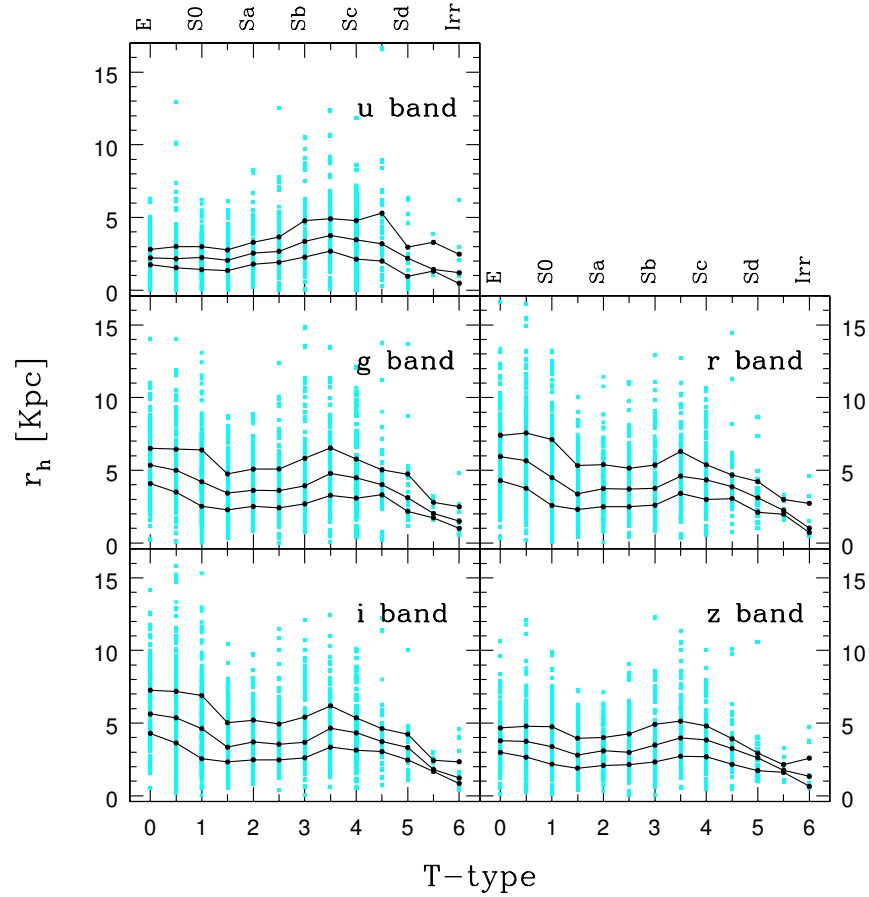
Figure 5.5: Disk scalelength as a function of the Hubble morphological T–type. A Sérsic plus exponential profile is fitted to the galaxies. Each point represents the value of r_h for each galaxy successfully modelled in the u, g, r, i and z photometric bands. The solid lines show the median, the upper and the lower quartiles of the distribution.
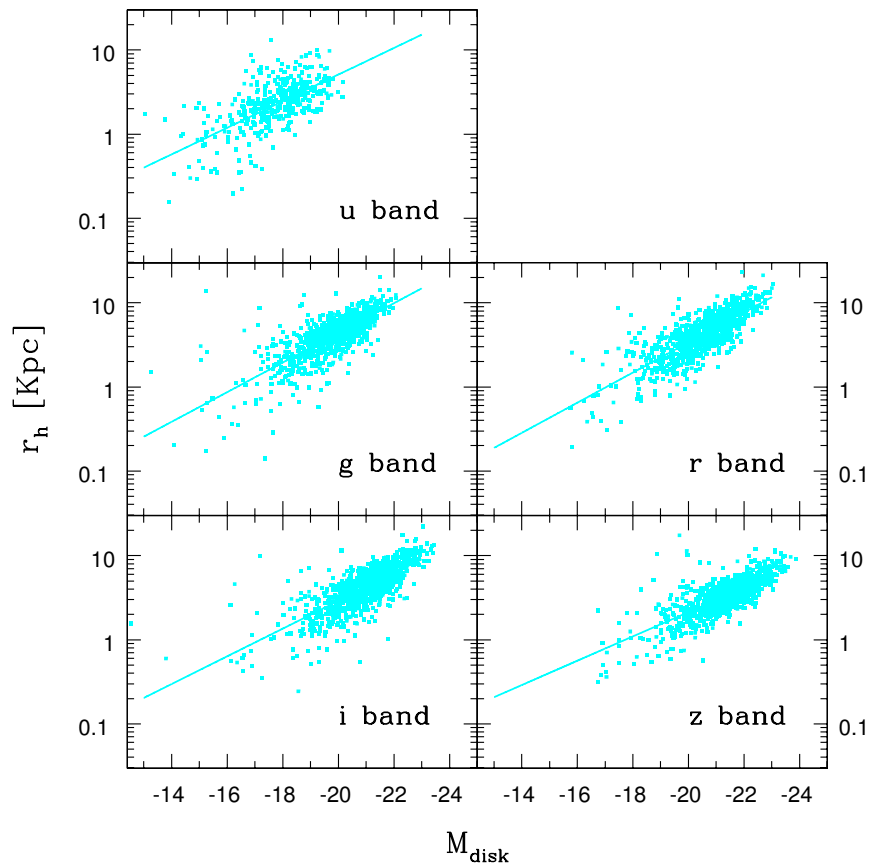
Figure 5.6: Relation between the disk scalelength and the absolute magnitude of the disk. Each point represents the value of r_h and M_{disk} for galaxies successfully modelled in the u, g, r, i and z photometric bands using a Sérsic plus exponential profile. The solid lines are linear regression fits to the data. See the text for more details.

Band	deV + exp		Sersic + exp	
	α	ζ	α	ζ
u	0.31 ± 0.03	0.48	0.39 ± 0.03	0.60
g	0.43 ± 0.02	0.68	0.44 ± 0.01	0.71
r	0.46 ± 0.01	0.76	0.45 ± 0.01	0.79
i	0.41 ± 0.01	0.74	0.41 ± 0.01	0.76
z	0.41 ± 0.01	0.77	0.36 ± 0.01	0.76

Table 5.2: The least–squares fitting results of the parameters in the r_h–M_{disk} relation. The data are shown for galaxies modelled with de Vaucouleurs plus exponential profile and Sérsic plus exponential fit in the 5 Sloan photometric bands. α is the exponent of the power law describing the dependence between the luminosity and the disk scalelength. The ζ columns are the correlation coefficients.

length r_h are the free parameters of the exponential light distribution. The total flux in the disk component is obtained by integrating equation 5.7 to infinity

$$F_{disk} = 2\pi \, r_h^2 \, \Sigma_0. \qquad (5.8)$$

The intrinsic surface brightness of the disk is obtained after applying a dimming correction to the central surface brightness. We finally express it in units of mag arcsec^{-2}

$$\mu_0 = m_{disk} + 2.5 \, \log(2 \, \pi \, r_h^2), \qquad (5.9)$$

as this is more familiar. The apparent magnitude of the disk, $m_{disk} = m - 2.5 \, \log(1 - B/T)$, is dereddened and k–corrected.

We investigate in Figure 5.4 the so called Freeman law (Freeman 1970). We show that in the 5 Sloan photometric bands the mean value of the intrinsic central surface brightness stays constant across all the morphological types, which is consistent with the Freeman disk. In more detail we observe that a decline is present for late–type objects. We have already mentioned that, since our sample is biased against late–type galaxies, the effect is not significant. We show in section 4.5 that late–type spirals have low mass. Therefore the decrease of the central surface brightness of late–type systems is in agreement with the results of other authors claiming that the Freeman law is not valid for low mass/luminosity galaxies. It is also worthy of note that a somehow lower value of μ_0 is also observed for elliptical and lenticular galaxies in the g and r band.

No particular trend is predicted for the distribution of the disk scalelength as a function of morphological type and we actually do not see any

Band	deV + exp			Sersic + exp		
	ζ_e	ζ_{eS}	ζ_{lS}	ζ_e	ζ_{eS}	ζ_{lS}
u	0.48	0.38	0.14	0.52	0.21	0.01
g	0.61	0.34	0.03	0.61	0.44	0.10
r	0.60	0.35	0.02	0.68	0.33	0.00
i	0.65	0.31	0.03	0.62	0.39	0.18
z	0.56	0.36	0.21	0.64	0.44	0.18

Table 5.3: Correlation coefficients for the r_e–r_h relation. The data are presented for galaxies modelled with de Vaucouleurs plus exponential profile and Sérsic plus exponential fit in the 5 Sloan photometric bands. Different columns refer to early–type systems (ζ_e, $0 \leqslant T \leqslant 1$), early–type spirals ($\zeta_{eS}$, $1 < T \leqslant 3$) and late–type spirals (ζ_{eS}, $3 < T \leqslant 5$).

in Figure 5.5. Since r_h is function of the mass/luminosity of the galaxy, only qualitative information can be retrieved. The galactic disks seem to be smaller in the z band and the ones of early–type and Sb galaxies are the largest compared to other morphological types.

Figure 5.6 shows the relation between the disk scalelength and the magnitude of the disk. In this plot we do not make any distinction between the disks of early, intermediate and late–type galaxies, as in the study of r_e–M_{bulge}, and we do not consider irregulars. The reason is that all disks, independently on the morphological type, are well fitted by the same power law. In Table 5.2 we show the least-squares fitting results of the parameters for the magnitude–size relation of the disk. The correlation coefficient, $\zeta \sim 0.7$, indicates that the fit is reliable even if a certain dispersion is present. We formulate the luminosity–size relation as

$$r_h \propto L_{disk}^{\alpha} \tag{5.10}$$

where $\alpha \sim 0.4$ and does not depend on the decomposition function used.

5.3.3 Bulge–disk correlations

In the previous sections we investigated the properties of galactic bulges and disks. Here we focus on possible existing correlations between the two photometric components in galaxies. We find that a correlation exists between the intrinsic surface brightness of the bulge and the central surface brightness of the disk (Figure 5.7) and between the effective radius of the bulge and the disk scalelength (Figure 5.8), although with a large scatter. The relationships are shown for morphologically selected subsamples, applying the same separation as in the other plots. The tightest correlations are the ones for early–type systems, $0 \leqslant T \leqslant 1$, and they depend slightly on
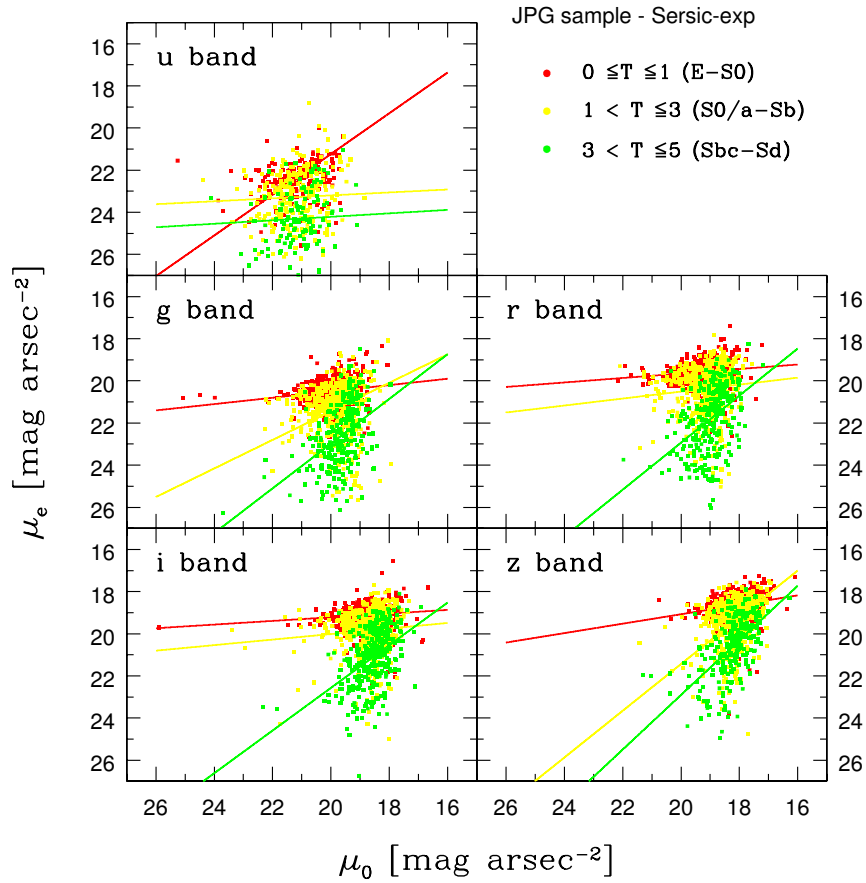
Figure 5.7: Relation between the intrinsic surface brightness of the bulge and the intrinsic central surface brightness of the disk. Each point represents the value of μ_e and μ_0 for galaxies successfully modelled in the u, g, r, i and z photometric bands using a Sérsic plus exponential profile. Red points are for early–type systems ($0 \leqslant T \leqslant 1$), yellow points for early–type spirals ($1 < T \leqslant 3$) and green points for late–type spirals ($3 < T \leqslant 5$). The same color scheme applies to the solid lines. They are linear regression fits to the data.

Figure 5.8: Relation between the effective radius of the bulge and the disk scalelength. Each point represents the value of r_e and r_h for galaxies successfully modelled in the u, g, r, i and z photometric bands using a Sérsic plus exponential profile. Red points are for early–type systems $(0 \leqslant T \leqslant 1)$, yellow points for early–type spirals $(1 < T \leqslant 3)$ and green points for late–type spirals $(3 < T \leqslant 5)$. The same color scheme applies to the solid lines. They are linear regression fits to the data.
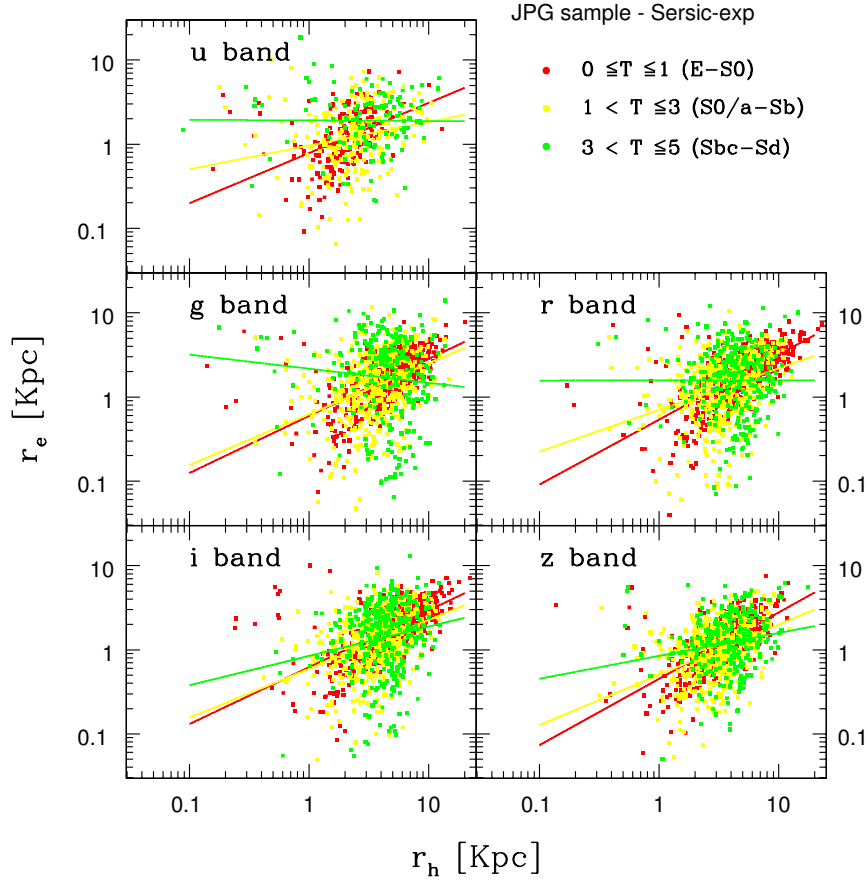
the considered photometric band. No real correlation exists between bulges and disks of late–type spirals, $3 < T \leqslant 5$. Early–type spirals, $1 < T \leqslant 3$, show very different trends in the μ_e–μ_0 plot depending on the photometric band while in the r_e–r_h plot they lie on a slope very similar to the one of early–type systems. Linear regression lines are fitted to the data and the correlation coefficients are shown in Table 5.3 for the correlation between the scalelengths of the bulge and disk components.

From the picture we described we infer that there is not a single mechanism that regulates the formation of the bulge and its interaction with the disk component.

5.4   Discussion & Conclusions

Using a homogeneous, complete sample of roughly 1800 morphologically classified galaxies with spectroscopic and photometric information in 5 filters, we provide a statistically significant view of the properties of galactic bulges and disks.

We find that our results do not depend strongly on the type of parametric functions adopted to perform the two–dimensional bulge–to–disk decomposition.

We can confirm with a higher confidence compared with de Jong (1996c) that the bulge and disk scalelengths do not show any correlation with the Hubble type, which is therefore a scale independent parameter. While galaxies belonging to the same morphological class span a pretty wide range in sizes and luminosities for the two photometric components, luminosity–size relations depending on morphology can be identified.

It is clear that larger systems are brighter. In addition we show that the properties of the bulges of early–type galaxies cannot be easily generalised to the bulges of spirals, and even between spirals not all the bulges look the same. The r_e–M_{bulge} relation is steeper for early–type systems than for late–type spirals. In contrast the r_h–M_{disk} relation does not change with galaxy morphology and can be parametrised by $r_h \propto L_{disk}^{0.4}$. The size–magnitude relation of disks turns out to be shallower than the one found by Shen et al. (2003) in the bright end for late–type galaxies. This is consistent with the fact that their late–type galaxies still contain a bulge component which steepens the relation.

We find a good correlation between r_e and r_h and between μ_e and μ_0. This is not in contrast with the weak correlation between μ_e and μ_0 claimed by de Jong (1996c). The reason of the apparent discrepancy resides in the fact that he does not distinguish between early and late–type spirals, which clearly follow a different trend.

It is worth noting that the correlations identified in the r_e–r_h plot have interesting implications on the formation and evolution of galaxies. Early–type
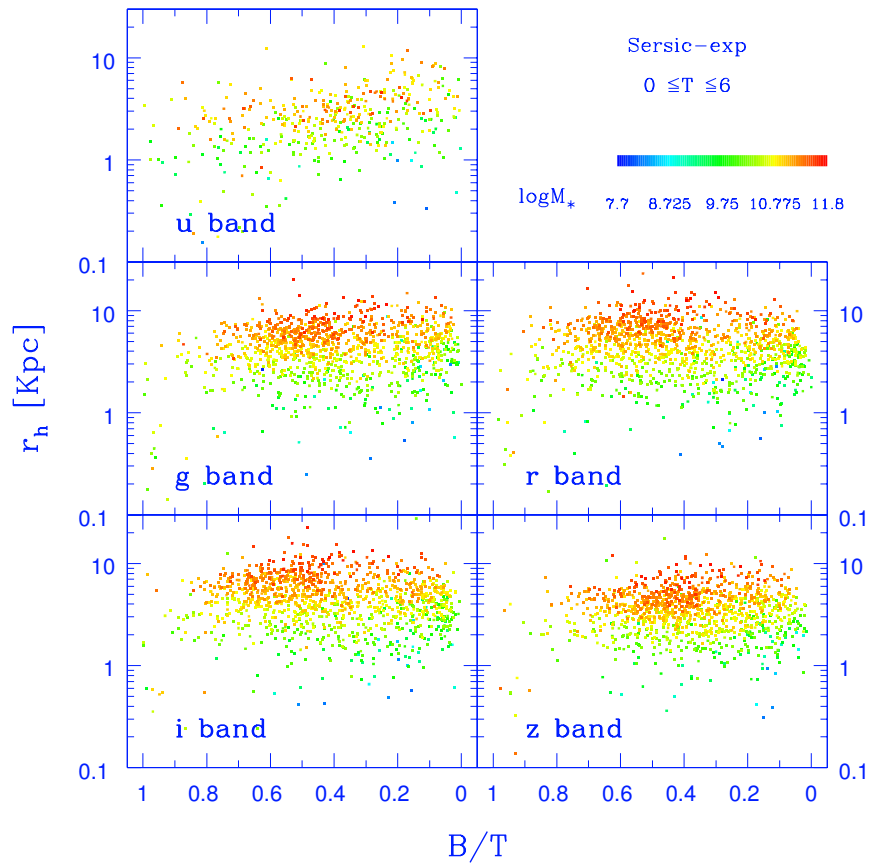
Figure 5.9: Relation between the disk scalelength and the bulge–to–disk ratio for galaxies of all morphological types ($0 \leqslant T \leqslant 6$) modelled with a Sérsic profile for the bulge and and exponential for the disk in the 5 Sloan photometric bands. The points are color-coded according to stellar masses.

systems and early–type spirals sit on the same slope, even if the correlation is more tight for the former. This behaviour can be explained in a scenario where disks form first and the bulges form afterwards via disk instability. In this case we expect bulges and disks to be closely coupled. From Figure 5.8 we can extrapolate that disks with larger scalelengths would form larger bulges. The presence of a bar also play an important role for the formation of the bulge, but we do not consider this aspect in our analysis.

Less obvious is the interpretation for the late–type spirals for which the bulge and disk scalelengths are not correlated. This suggests that a different mechanism is driving the bulge formation in these systems. The merging scenario can be invoked for the formation of bulges. Disks may form later through accretion of cold gas.

As a further check we investigate in Figure 5.9 the relation between the disk scalelength and the bulge–to–disk ratio as a function of stellar mass. We do not observe the correlation reported by Shen et al. (2003), that they interpret as a support of the disk–instability–driven scenario.

Conclusions

The challenge for modern astrophysics is to confront observational constraints with current theoretical and numerical models of galaxy formation and evolution. Thus, one hopes to reveal the main physical processes at work and the associated time–scales.

We use a complete magnitude limited sample of 1862 galaxies drawn from the Sloan Digital Sky Survey to investigate a large number of global and structural parameters. The sample includes bright objects, with an r–magnitude of $\leqslant$ 15.9, in the nearby universe, with redshift $z \leqslant 0.12$. It contains ellipticals, lenticulars, early and late–type spirals and irregulars. Photometric data are provided in u, g, r, i, and z bands and spectroscopic follow–ups are carried out for 1588 galaxies in the sample. The more general Sérsic $r^{1/n}$ profile and the de Vaucouleurs $r^{1/4}$ law are used to model the surface brightness in the bulge component while we assume that the light in the disk component has an exponential distribution.

As a result of the evolutionary process, the main components of galaxies are a spherical bulge and a flat, extended disk. Measuring the evolution of the fraction of light in these two components with time gives an indication of the efficiency of the hierarchical clustering process. In chapter 3 we show that the mean fraction of light in the disk component increases strongly with the total absolute magnitude of the galaxy, i.e. it is larger for fainter objects. Independent r and i band analyses give a very similar trend. For the first time we estimate the volume–averaged value for the fraction of light in disks and conclude that roughly $(55 \pm 2)\%$ of the total light in the local universe is in the disk component. We also determine the luminosity function for pure bulges, which are structures without a disk component and not simply spheroids.

In chapter 4 we study the relations between visual and quantitative morphological classifiers in order to define criteria to select clean galaxy samples, even at high redshift where the visual classification becomes somewhat arbitrary. We find that rest–frame galaxy colours, concentration index, bulge–to–disk ratio, effective surface brightness, mass–to–light ratio, residual and asymmetry parameters define a multi–parameter space in which galaxies of all morphological types are located according to well defined physical properties. We conclude that the quantitative morphological classifiers that we

have selected allow us to build galaxy samples according to their stellar masses, mean stellar ages and gas–phase metallicities.

In chapter 5 we observe that there is a clear trend for the disk scalelength to increase with the disk magnitude, with only a small dispersion, independent of the photometric band and of the morphology. The relation between the effective radius of the bulge and the bulge magnitude is also well defined but changes slope as a function of the morphological type. It becomes steeper for earlier types, which leads us to the conclusion that the disk scalelength is less dependent on the morphology than is the bulge scalelength. These results suggest that bulges form by different mechanisms in late and early–type galaxies. We also find that a correlation exists between disk and bulge structural parameters, in particular between the effective radius of the bulge and the disk scalelength for early–type systems. We interpret that as observational support for secular evolution models.

Interesting future extensions of this work are related to the study of the fundamental scaling relations of galaxies (e.g. Fundamental Plane of spiral galaxies and of spheroids), which should provide constraints on models of galaxy formation and evolution, and of colours and masses of bulges and disks. A natural continuation of this work would be to analyse the morphology of galaxies at high–redshift and their distribution in large scale structure in order to study the connection between morphology, environment and evolution.

Bibliography

Abraham, R. G., Valdes, F., Yee, H. K. C., & van den Bergh, S. 1994, ApJ, 432, 75

Abraham, R. G., Tanvir, N. R., Santiago, B. X., Ellis, R. S., Glazebrook, K., & van den Bergh, S. 1996, MNRAS, 279, L47

Andredakis, Y. C., Peletier, R. F., & Balcells, M. 1995, MNRAS, 275,874

Andredakis, Y. C. 1998, MNRAS, 295, 725

Baggett, W. E., Baggett, S. M., & Anderson, K. S. J. 1998, AJ, 116, 1626

Bender, R., Burstein, D., & Faber, S. M. 1992, ApJ, 399, 462

Bendinelli, O. 1991, ApJ, 366, 599

Bennett C.L., Banday A.J., Gorski K.M., Hinshaw G., Jackson P., Keegstra P., Kogut A., Smoot G. F., Wilkinson D.T., & Wright E.L. 1996, ApJ, 464, 1

Bennett C.L., Bay M., Halpern M., Hinshaw G., Jackson C., Jarosik N., Kogut A., Limon M., Meyer S.S., Page L., Spergel D.N., Tucker G.S., Wilkinson D.T., Wollack E., & Wright E.L. 2003a, ApJ, 583, 1

Bennett C.L., Halpern M., Hinshaw G., Jarosik N., Kogut A., Limon M., Meyer S.S., Page L., Spergel D.N., Tucker G.S., Wollack E., Wright E.L., Barnes C., Greason M.R., Hill R.S., Komatsu E., Nolta M.R., Odegard N., Peiris H.V., Verde L., & Weiland J.L. 2003b, ApJS, 148, 1

Bernardi, M. et al. 2003, AJ, 125, 1817

Bernardi, M. et al. 2003, AJ, 125, 1849

Bernardi, M. et al. 2003, AJ, 125, 1866

Bernardi, M. et al. 2003, AJ, 125, 1882

Bertin, E., & Arnouts, S. 1996, A&AS, 117, 393

Bershady, M. A., Jangren, A., & Conselice, C. J. 2000, AJ, 119, 2645

Binggeli, B., Sandage, A., & Tammann, G. A. 1985, AJ, 90, 1681

Binggeli, B., Sandage, A., & Tammann, G. A. 1988, ARA&A, 26, 509

Blanton, M. R., et al. 2001, AJ, 121, 2358

Blanton, M. R., et al. 2003, AJ, 125, 2348

Blanton, M. R., et al. 2003, ApJ, 592, 819

Boroson, T. 1981, ApJS, 46, 177

Brinchmann, J., Abraham, R., Schade, D. , Tresse, L., Ellis, R. S., Lilly, S.,
    Le Févre, O., Glazebrook, K., Hammer, F., Colless, M., Crampton, D.,
    Broadhurst, T. et al. 1998, ApJ, 499, 112

Broadhurst, T. J., Ellis, R. S., & Glazebrook, K. 1992, Nature, 355, 55

Bromley, B. C., Press, W. H., Lin, H., & Kirshner, R. P. 1998, ApJ, 505, 25

Bruzual A., G. & Charlot, S. 1993, ApJ, 405, 538

Bruzual, G. & Charlot, S. 2003, MNRAS, 344, 1000

Burstein, D. 1979, ApJ, 234, 829

Byun, Y. I. & Freeman, K. C. 1995, ApJ, 448, 563

Carlberg, R. G., et al. 2000, ApJ, 532, L1

Ciotti, L. 1991, A&A, 249, 99

Connolly, A. J., et al. 2002, ApJ, 579, 42

Conselice, C. J., Bershady, M. A., & Jangren, A. 2000, ApJ, 529, 886

Conselice, C. J. 2003, ApJS, 147, 1

Conselice, C. J., Bershady, M. A., Dickinson, M., & Papovich, C. 2003, AJ,
    126, 1183

Conselice, C. J., O'Neil, K., Gallagher, J. S., & Wyse, R. F. G. 2003, ApJ,
    591, 167

Conselice, C. J., et al. 2004, ApJ, 600, L139

Cole, S., Aragon-Salamanca, A., Frenk, C. S., Navarro, J. F., & Zepf, S. E.
    1994, MNRAS, 271, 781

Cole, S., Lacey, C. G., Baugh, C. M., & Frenk, C. S. 2000, MNRAS, 319, 168

Colless, M., et al. 2001, MNRAS, 328, 1039

Conklin, E. K., 1969, PhD Thesis

Courteau, S., de Jong, R. S., & Broeils, A. H., 1996, ApJ, 457, L73

Daddi, E., et al. 2003, ApJ, 588, 50

Davis, M., et al. 2003, Proc. SPIE, 4834, 161

Dickinson, M., Papovich, C., Ferguson, H. C., & Budavári, T. 2003, ApJ, 587, 25

Djorgovski, S. & Davis, M. 1987, ApJ, 313, 59

Dodelson, S., et al. 2002, ApJ, 572, 140

Doi, M., Fukugita, M., & Okamura, S. 1993, MNRAS, 264, 832

Dressler, A. 1980, ApJ, 236, 351

Dressler, A., Gunn, J. E. 1983, ApJ, 270, 7

Dressler, A., Lynden-Bell, D., Burstein, D., Davies, R. L., Faber, S. M., Terlevich, R., & Wegner, G. 1987, ApJ, 313, 42

de Bernardis P., Ade P.A.R., Bock J.J., Bond J.R., Borrill J., Boscaleri A., Coble K., Crill B.P., De Gasperis G., Farese P.C., Ferreira P.G., Ganga K., Giacometti M., Hivon E., Hristov V.V., Iacoangeli A., Jaffe A.H., Lange A.E., Martinis L., Masi S., Mason P.V., Mauskopf P.D., Melchiorri A., Miglio L., Montroy T., Netterfield C.B., Pascale E., Piacentini F., Pogosyan D., Prunet S., Rao S., Romeo G., Ruhl J.E., Scaramuzzi F., Sforna D., Vittorio N., 2000, Nature, 404, 955

de Jong, R. S. 1996, A&AS, 118, 557

de Jong, R. S. 1996, A&A, 313, 45

de Lapparent et al., in press, astro-ph/0404236 v2

de Vaucouleurs, G. 1948, *Annales d'Astrophysique*, 11, 247

de Vaucouleurs, G. 1959, *Handbuch der Physik*, 53, 275

de Vaucouleurs, G. 1977, *Evolution of Galaxies and Stellar Populations*, 43

de Vaucouleurs, G., de Vaucouleurs, A., Corwin, H. G., Buta, R. J., Paturel, G., & Fouque, P. 1991, *Third Reference Catalogue of Bright Galaxies*, 82, 621

Efstathiou, G. 1992, MNRAS, 256, 43P

Efstathiou, G. & Rees, M. J., 1988, MNRAS230, 5P

Eggen, O. J., Lynden-Bell, D., & Sandage, A. R. 1962, ApJ, 136, 748

Faber, S. M. & Jackson, R. E. 1976, ApJ, 204, 668

Faber, S. M., Dressler, A., Davies, R. L., Burstein, D., & Lynden-Bell, D. 1987, *Nearly Normal Galaxies. From the Planck Time to the Present*, 175

Faber, S. M., et al. 1997, AJ, 114, 1771

Fasano, G., Cristiani, S., Arnouts, S., & Filippi, M. 1998, AJ, 115, 1400

Ferrarese, L., van den Bosch, F. C., Ford, H. C., Jaffe, W., & O'Connell, R. W. 1994, AJ, 108, 1598

Fischer, P. 2000, AJ, 120, 1198

Folkes, S., et al. 1999, MNRAS, 308, 459

Freedman W.L., Madore B.F., Gibson B.K., Ferrarese L., Kelson D.D., Sakai S., Mould J.R., Kennicut R.C., Ford H.C., Graham J.A., Huchra J.P., Hughues S.M.G., Illingworth G.D., Macri L.M., Stetson P.B. 2001, ApJ, 553, 47

Freeman, K. C. 1970, ApJ, 160, 811

Franx, M., et al. 2003, ApJ, 587, L79

Fukugita, M., Ichikawa, T., Gunn, J. E., Doi, M., Shimasaku, K., & Schneider, D. P. 1996, AJ, 111, 1748

Fukugita, M., Nakamura, O., Turner, E. L., Helmboldt, J. & Nichol, R. C. 2004, ApJ, 601,L127

Gallazzi, A., et al. 2004, in preparation

Gamow, 1948a, phys. Rev., 74, 505

Gamow, 1948b, Nature, 162, 680

Gavazzi, G., Pierini, D., & Boselli, A. 1996, A&A, 312, 397

Giavalisco, M., Steidel, C. C., Adelberger, K. L., Dickinson, M. E., Pettini, M., & Kellogg, M. 1998, ApJ, 503, 543

Gunn, J. E., et al. 1998, AJ, 116, 3040

Guzzo, L., Strauss, M. A., Fisher, K. B., Giovanelli, R., & Haynes, M. P. 1997, ApJ, 489, 37

Hanany S., Ade P.A.R., Balbi A., Bock J.J., Borrill J., Boscaleri A., de Bernardis P., Ferreira P.G., Hristov V.V., Jaffe A.H., Lange A.E., Lee A.T., Mauskopf P.D., Netterfield C.B., Oh, S.; Pascale E., Rabii B., Richards P.L., Smooth G.F., Stompor R., Winant C.D., Wu J.H.P. 2000,ApJ, 545, 5

Hogg, D. W., Finkbeiner, D. P., Schlegel, D. J., & Gunn, J. E. 2001, AJ, 122, 2129

Hubble, E. P. 1936, *Realm of the Nebulae.* Yale University Press

Huchra, J., Davis, M., Latham, D., & Tonry, J. 1983, ApJS, 52, 89

Im, M., et al. 2002, ApJ, 571, 136

Katz, N. & White, S. D. M. 1993, ApJ, 412, 455

Kauffmann, G. & White, S. D. M. 1993, MNRAS, 261, 921

Kauffmann G., White S.D.M., & Guiderdoni B., 1993, MNRAS, 264, 201

Kauffmann, G., et al. 2003, MNRAS, 341, 33

Kayo, I. 2004, PASJ, 56, 415

Kelly, B. C. & McKay, T. A. 2004, AJ, 127, 625

Kent, S. M. 1985, ApJS, 59, 115

Khosroshahi, H. G., Wadadekar, Y., & Kembhavi, A. 2000, ApJ, 533, 162

Khosroshahi, H. G., Raychaudhury, S., Ponman, T. J., Miles, T. A., & Forbes, D. A. 2004, MNRAS, 349, 527

Kobayashi C., 2002, PhD Thesis

Komatsu E., Kogut A., Nolta M., Bennett C.L., Halpern M., Hinshaw G., Jarosik N., Limon M., Meyer S.S., Page L., Spergel D.N., Tucker G.S., Verde L., Wollack E., Wright E.L., 2003, ApJS, 148, 119

Kormendy, J. 1977, ApJ, 218, 333

Kormendy, J. 1979, ApJ, 227, 714

Kormendy, J. & Illingworth, G. 1983, ApJ, 256, 460

Kormendy, J. 1987, *Nearly Normal Galaxies. From the Planck Time to the Present*, 163

Kormendy, J. & Bender, R. 1996, ApJ, 464, L119

Kormendy, J. & Djorgovski, S. 1989, ARA&A, 27, 235

Lahav O., Lilje P.B., Primack J.R., Rees M.J., 1991, MNRAS, 251, 128

Larson, R. B. 1974, MNRAS, 166, 585

Lauer, T. R., et al. 1995, AJ, 110, 2622

Le Fèvre, O., Hudon, D., Lilly, S. J., Crampton, D., Hammer, F., & Tresse, L. 1996, ApJ, 461, 534

Le Fèvre, O., et al. 2000, MNRAS, 311, 565

Le Fèvre, O., et al. 2004, A&A, 417, 839

Lilly, S. J. 1993, ApJ, 411, 501

Lilly, S. J., Cowie, L. L., & Gardner, J. P. 1991, ApJ, 369, 79

Lilly, S. J., Le Fèvre, O., Crampton, D., Hammer, F., & Tresse, L. 1995, ApJ, 455, 50

Lilly, S. J., Le Fèvre, O., Hammer, F., & Crampton, D. 1996, ApJ, 460, L1

Lilly, S., et al. 1998, ApJ, 500, 75

Lin, H., Kirshner, R. P., Shectman, S. A., Landy, S. D., Oemler, A., Tucker, D. L., & Schechter, P. L. 1996, ApJ, 471, 617

Lupton, R. H., Gunn, J. E., Ivezić, Z., Knapp, G. R., Kent, S., & Yasuda, N. 2001, ASP Conf. Ser. 238: Astronomical Data Analysis Software and Systems X, 10, 269

Lupton, R. H., Ivezic, Z., Gunn, J. E., Knapp, G., Strauss, M. A.,& Yasuda, N. 2002, Proceedings of the SPIE, 4836, 350

Marleau, F. R. & Simard, L. 1998, ApJ, 507, 585

Madau, P., Pozzetti, L., & Dickinson, M. 1998, ApJ, 498, 106

Maddox S.J., Efstathiou G., Sutherland W.J., Loveday J., 1990, MNRAS, 243, 692

Madgwick, D. S., et al. 2003, ApJ, 599, 997

Mather, J. C., et al. 1994, ApJ, 420, 439

Metcalfe, N., Shanks, T., Fong, R., & Roche, N. 1995, MNRAS, 273, 257

Moore B., Governato F., Quinn T., Stadel J., Lake G., 1998, ApJ, 499, 5

Naim, A., et al. 1995, MNRAS, 274, 1107

Naim, A., Ratnatunga, K. U., & Griffiths, R. E. 1997, ApJS, 111, 357

Nakamura, O., Fukugita, M., Yasuda, N., Loveday, J., Brinkmann, J., Schneider, D. P., Shimasaku, K., & SubbaRao, M. 2003, AJ, 125, 1682

Navarro J.F., Steinmetz M., 1997, ApJ, 478, 13

Noguchi, M. 2000, MNRAS, 312, 194

Odewahn, S. C. 1995, PASP, 107, 770

Pascarelle, S. M., Windhorst, R. A., Keel, W. C., & Odewahn, S. C. 1996, Nature, 383, 45

Patton, D. R., Carlberg, R. G., Marzke, R. O., Pritchet, C. J., da Costa, L. N., & Pellegrini, P. S. 2000, ApJ, 536, 153

Pelló, R., Schaerer, D., Richard, J., Le Borgne, J.-F., & Kneib, J.-P. 2004, A&A, 416, L35

Peng, C. Y., Ho, L. C., Impey, C. D., & Rix, H. 2002, AJ, 124, 266

Petrosian, V. 1976, ApJ, 209, L1

Press W.H., Schechter P., 1974, ApJ, 187, 425

Ratnatunga, K. U., Griffiths, R. E., & Ostrander, E. J. 1999, AJ, 118, 86

Ravindranath, S., Ho, L. C., Peng, C. Y., Filippenko, A. V., & Sargent, W. L. W. 2001, AJ, 122, 653

Roberts, M. S. & Haynes, M. P. 1994, ARA&A, 32, 115

Sandage, A. 1961, Washington: *The Hubble atlas of galaxies* Carnegie Institution

Schade, D., Lilly, S. J., Crampton, D., Hammer, F., Le Fèvre, O., & Tresse, L. 1995, ApJ, 451, L1

Schade, D., Lilly, S. J., Le Fèvre, O., Hammer, F., & Crampton, D. 1996, ApJ, 464, 79

Schechter, P., 1976, ApJ, 203, 297

Schlegel, D. J., Finkbeiner, D. P., & Davis, M. 1998, ApJ, 500, 525

Schneider, D. P., et al. 2003, AJ, 126, 2579

Scodeggio, M., Gavazzi, G., Franzetti, P., Boselli, A., Zibetti, S., & Pierini, D. 2002, A&A, 384, 812

Sersic, J. L. 1968, *Atlas de galaxias australes.* Observatorio Astronomico, Cordoba

Shaw, M. A. & Gilmore, G. 1989, MNRAS, 237, 903

Shen, S., et al. 2003, MNRAS, 343, 978

Shimasaku, K., et al. 2001, AJ, 122, 1238

Simard, L., et al. 2002, ApJS, 142, 1

Smith, J. A., et al. 2002, AJ, 123, 2121

Smail, I., Dressler, A., Couch, W. J., Ellis, R. S., Oemler, A. J., Butcher, H., & Sharples, R. M. 1997, ApJS, 110, 213

Spergel D.N., Verde L., Peiris H.V., Komatsu E., Nolta M.R., Bennett, C.L., Halpern M., Hinshaw G., Jarosik N., Kogut A., Limon M., Meyer S.S., Page L., Tucker G.S., Weiland J.L., Wollack E., Wright E.L., 2003, ApJS, 148, 175

Springel, V., White, S. D. M., Tormen, G., & Kauffmann, G. 2001, MNRAS, 328, 726

Steidel, C. C., Giavalisco, M., Dickinson, M., & Adelberger, K. L. 1996, AJ, 112, 352

Steidel, C. C., Giavalisco, M., Pettini, M., Dickinson, M., & Adelberger, K. L. 1996, ApJ, 462, L17

Steidel, C. C., Adelberger, K. L., Giavalisco, M., Dickinson, M., & Pettini, M. 1999, ApJ, 519, 1

Steidel, C. C., Shapley, A. E., Pettini, M., Adelberger, K. L., Erb, D. K., Reddy, N. A., & Hunt, M. P. 2004, ApJ, 604, 534

Stoughton, C., et al. 2002, AJ, 123, 485

Strateva, I., et al. 2001, AJ, 122, 1861

Strauss, M. A., et al. 2002, AJ, 124, 1810

Tegmark, M. et al. 2004, ApJ, 606, 702

Tinsley, B. M. & Gunn, J. E. 1976, ApJ, 203, 52

Tremonti, C. A., et al. 2004, ApJ accepted

Tyson, J. A. 1988, AJ, 96, 1

Tully, R. B. & Fisher, J. R. 1977, A&A, 54, 661

Tully, R. B., Pierce, M. J., Huang, J., Saunders, W., Verheijen, M. A. W. & Witchalls, P. L. 1998, AJ, 115, 2264

van Dokkum, P. G. & Franx, M. 2001, ApJ, 553, 90

van den Bergh, S., Abraham, R. G., Ellis, R. S., Tanvir, N. R., Santiago, B. X., & Glazebrook, K. G. 1996, AJ, 112, 359

Wadadekar, Y., Robbason, B., & Kembhavi, A. 1999, AJ, 117, 1219

Watanabe, M., Kodaira, K., & Okamura, S. 1985, ApJ, 292, 72

Whitmore, B. C. 1984, ApJ, 278, 61

Wirth, A. & Gallagher, J. S. 1984, ApJ, 282, 85

Yasuda, N. et al. 2001, AJ, 122, 1104

York D.G. et al. (The SDSS Collaboration), 2000, AJ, 120, 1579

Young, C. K. & Currie, M. J. 1994, MNRAS, 268, L11

Zehavi, I. et al. 2002, ApJ, 571, 172

Zucca, E. 1997, A&A, 326, 477

Acknowledgment

...what is that? Fields to the right and to the left, cloudy and foggy. Where is the sun?! Gosh, in Italy was summer...

It was the 11th of April 2001, when I arrived in Munich for the first interview of my life. I didn't reach the institute and I was already sure that I wanted to go back!
Thank God, I didn't do that: the years I spent here were simply magic and now, that I look back, I try to remember the people and friends who transformed these years of my life into an unforgettable dream.

At first, a very special thanks to Simon D.M. White. I am greatly indebted to him for giving me the great opportunity to come to Munich and do research in his group. He guided this work through his competent advice and stimulating discussions.

My sincere gratitude is dedicated to Thomas Janka for his unremitting support and encouragement.

My very special gratitude is given to Shiyin Shen and Hans–Jakob Grimm for being not only special friends but also for acting as "second supervisors" who I missed.

For the numerous interesting discussions and for their help I am sincerely grateful to many friends: Gregory Rudnick, Annette Ferguson, Stephane Charlot, Jarle Brinchmann, Frank van den Bosch, Francesco Miniati, Martin Jubelgas, among many.

I am very thankful to Marcus Bruggen for his positive way of thinking, for "our jump" in the lake and for preventing me from sleeping under a bridge. For their friendship and their support I am very thankful to Bene, Barbarella, Chiaki, Claudia, Eli, Serena, Silvia, Tiri, Tiziana, Hugues, Olivier G., Luigi, Martin, Joachim and Bernhard. Thanks to Brice for all he represents to me.

It is impossible not to thank my perfect office–mate Jon for teaching me English and for listening to me in my sad and euphoric moods. He also

deserves my congratulations since he managed to survive in the office with me for more than 3 years defending himself with the only weapons he had: British self–control!

I would like to thank all colleagues who contribute to the productive and serene atmosphere in the institute, and apologise to all those that I have failed to mention by name. They are in my heart, anyhow!

I am thankful to the ever–friendly secretaries (Maria, Cornelia, Kate and Gabi) and the mostly–ever–friendly system–managers for all their help.

Finally, I am sincerely grateful to my whole family, in particular to my parents, Frattata, zio Titti and Girmy. I could have not finished this thesis without all their support and love. Not for the thesis but for his understanding, patience, help and love and for his ability to deal with my "particular" character, I am deeply indebted to my loved Olivier.